LOCALIZATION AND SUPERCONDUCTIVITY IN THIN FILMS AND NARROW WIRES OF ALUMINUM

A Dissertation

Presented to the Faculty of the Graduate School

of

Yale University

in Candidacy for the Degree of

Doctor of Philosophy

by

Padmanabhan Santhanam

May 1985

ABSTRACT

LOCALIZATION AND SUPERCONDUCTIVITY

IN THIN FILMS AND NARROW WIRES

OF ALUMINUM

Padmanabhan Santhanam

Yale University

1985

The theory of localization predicts that constructive interference between electron waves scattered by impurities results in a quantum correction to the electrical resistance. The study of changes in resistance as a function of temperature and magnetic field can help us verify the theory of localization.

A comprehensive set of experiments were performed on thin films of aluminum for testing the localization theory. Experiments on wide thin films in the quasi-two-dimensional regime confirm the theoretical predictions. These experiments have also yielded considerable quantitative insight about inelastic mechanisms and spin-orbit scattering rates in these films. The inelastic mechanisms that cause delocalization of electrons in our films are electron-phonon scattering and electron-electron scattering. The inferred inelastic rates we obtain are in good agreement with those obtained for films with comparable properties, from other types of experiments, done in the superconducting state. In our

films, the spin-orbit scattering rate is observed to scale with the elastic scattering rate.

The study of localization in quasi-one-dimensional systems requires metallic wires which are less than a micrometer in width. A new lithographic process involving a three-dimensional shadowing technique was developed, but had limited success. An alternate method using x-ray lithography has proved more successful in the fabrication of submicron-width samples.

We have extended the existing theory for quasi-one-dimensional systems to include spin-orbit scattering and Maki-Thompson superconducting fluctuations. Our experiments on narrow aluminum wires have verified this new theory successfully. The prediction of the localization theory of a crossover from two-dimensional behavior to one-dimensional behavior is also confirmed. Furthermore, we infer electron inelastic scattering rates in narrow wires that are identical to those in two-dimensional films. Our analysis of the previous experiments by other workers on narrow metallic wires indicates that the resistance changes observed in those experiments were probably not due to electron localization.

To the memory of

my parents

JANAKI and RANGANATHAN PADMANABHAN

ACKNOWLEDGEMENTS

The years I have spent in graduate school would have been miserable without the help, encouragement and friendship of many people. I will name a few who have played important roles in the work that culminated in this thesis and have helped me on various occasions with their guidance, suggestions and hard work.

It is with warm gratitude that I thank Professor Daniel Prober for his enthusiasm and support during the past five and a half years. In addition to his excellent professional guidance, his attention to detail and thoroughness have been inspiring. He has also been a good friend.

Shalom Wind has contributed enormously to the experiments reported in this thesis through his fabrication of the narrow wires and his help in the low temperature experiments. Bruce Dalrymple built the cryostat with which almost all the experiments reported in this thesis were performed. He also wrote the first few computer programs used in the data analysis. Dean Face characterized the Reactive Ion Etching System that was used in the fabrication of the narrow wires. He has also been a close friend and, I cannot count the occasions when we have discussed everything from the Meaning of Life to Superconductivity in d-band Metals. Michael Rooks has been a great help with his knowledge of computers that come in all sizes and shapes, and his initiative in the installation of the various computer equipment. Jim Gordon (of Harvard) started the first localization experiments on aluminum wires at Yale, when some of the ideas on the fabrication of narrow wires took shape.

Dr. Alan Pooley of the Peabody Museum at Yale helped me with the Scanning Electron Microscopy, used heavily during the initial stages of

this work. Clifford Snyder came to my rescue on many an occasion with his expertise in vacuum systems and the design of the various mechanical components. June Yarosh provided the secretarial assistance with the utmost efficiency. Jayne Miller and Linda Schwartz courteously saved me from the jaws of panic in many instances with their help.

The use of the semiconductor clean-room facilities at Yale was essential for the success of this work. The financial support of the National Science Foundation through grants DMR 7817957 and DMR 8207443 made this work possible. A partial support of the x-ray lithography system by the NSF grant ECS 7927165 is also acknowledged.

I would like to thank Professors V.E. Henrich, D.E. Prober, J.W. Serene and R.G. Wheeler for serving on my thesis committee. I am grateful to Dr. J.W. Serene for his general interest and help in the theory pertaining to this work and for finding some time in his busy schedule at the NSF to attend my thesis defense.

My thanks are also to V. Chandrasekhar for proof-reading the thesis. Sal Dattilo did many of the figures. Our group at Yale has somehow maintained its sense of humor over the years, even though its complexion has changed considerably during my stay. My thanks to all the members of our group over the years who made my stay at Yale thoroughly enjoyable.

'I can no other answer make but thanks,
And thanks, and ever oft good turns
Are shuffled off with such uncurrent pay'

Shakespeare in 'The Twelfth Night'

TABLE OF CONTENTS

FREQUENTLY USED SYMBOLS AND ABBREVIATIONS

m_o	Free electron mass
k_B	Boltzmann's constant
h	Planck's constant
$\hbar$	Planck's constant divided by 2π
$\vec{\sigma}$	Pauli operator for electron spin
μ_B	Bohr magneton
α	Fine structure constant
g	Lande' g factor
Φ_o	Flux quantum
c	Speed of light
e	Magnitude of the electronic charge
m^*	Effective electron mass in Al
E_F	Fermi energy
k_F	Fermi wave vector
v_F	Fermi velocity
T_c	Superconducting transition temperature
Γ	Residual resistance ratio
n	Number density of electrons per unit volume
$\eta(E_F)$	Density of states per unit volume per unit energy at the Fermi energy
τ	Elastic scattering time
τ_i	Inelastic scattering time
τ_{so}	Spin-orbit scattering time
τ_2	Effective scattering time for the relaxation of the triplet component of the Cooperon.

τ_s	Magnetic scattering time
τ_{q^*}	Charge imbalance relaxation time
τ_{ee}	Electron-electron scattering time corresponding to transfers of energy $\sim k_B T$
τ_ε	Electron-electron scattering time corresponding to small energy transfers.
τ_{ep}	Electron-phonon scattering time
D	Diffusion constant
ℓ	Elastic mean free path
ℓ_i	Inelastic scattering length
ℓ_{so}	Spin-orbit scattering length
ℓ_2	Effective scattering length corresponding to τ_2
ℓ_{int}	Characteristic length for electron-electron interaction
$\beta(T/T_c)$	Parameter characterizing the interaction between electrons in the Maki-Thompson term for conductivity
σ	Conductivity
ρ	Resistivity
W	Sample width
L	Sample length
d	Sample thickness
A	Cross-sectional area of a wire
H_i	Characteristic inelastic field
H_{so}	Characteristic spin-orbit field
H_o	Characteristic elastic scaling field
H_2	Characteristic field corresponding to ℓ_2
H_W	Characteristic field corresponding to sample width
H_{int}	Characteristic field for orbital effects due to electron-electron interaction

H_{sp}	Characteristic field for spin-effects due to electron-electron interaction
H_d	Characteristic field corresponding to the sample thickness
v_s	Velocity of transverse sound
q_{ph}	Phonon wave vector
λ_{ph}	Phonon wavelength
θ_D	Debye Temperature
ω_c	Cyclotron frequency
ψ	Digamma function
ΔR	Contribution to resistance at a fixed magnetic field and temperature
$\tilde{\delta}R$	Change of resistance as a function of temperature = $R(T,H) - R(T_{ref}, H)$
δR	Magnetoresistance = $R(T,H) - R(T,H=0)$
MR	Abbreviation for magnetoresistance
$R_\square$	Sheet resistance or resistance per square of the film.
ε_n	Eigenvalues of the Cooperon operator
MT	Abbreviation for Maki-Thompson
Δ	Superconducting energy gap
ξ	Superconducting coherence length
λ_{Q^*}	Charge imbalance relaxation length
H_{c2}	Superconducting upper critical field
$H_{c2\|\|}$	Upper critical field, H parallel to the film plane
$Hc2_\perp$	Upper critical field, H perpendicular to the film.

LIST OF FIGURES

LIST OF TABLES

I. INTRODUCTION

In a perfectly crystalline solid the electrons occupy the well known Bloch states. The periodic arrangement of atoms in a solid introduces energy bands, with energy gaps at the Brillouin zone boundaries. In the conventional theory of metals, one assumes that the conduction electrons partially fill the (conduction) band and that these electrons can be excited with arbitrarily small energy. This behavior is to be contrasted with the situation in semiconductors or insulators where there are filled bands of electrons (with energy gaps separating them from empty bands). The electrical resistivity in a perfectly crystalline metal will vanish at absolute zero temperature due to lack of electron scattering events. At higher temperatures, however, non-zero resistivity results due to scattering by phonons (lattice vibrations). If there are defects in the lattice, such as impurities or disorder, even at absolute zero there will be a residual resistance due to these defects. This behavior is schematically illustrated in Fig. I-1. Here, we have assumed the metal under discussion is a non-superconductor.

I-A LOCALIZATION

The concept of electron localization was first introduced by Anderson[1]. It has to do with the nature of the one-electron wave functions in a disordered medium. If the disorder is weak, the wave function is extended in space. However, if the disorder is strong, the wave function may change its nature completely and become spatially localized; that is, the wave function envelope decays exponentially with distance. Thus with sufficient disorder the 'metal' can show <u>infinite resistance</u>

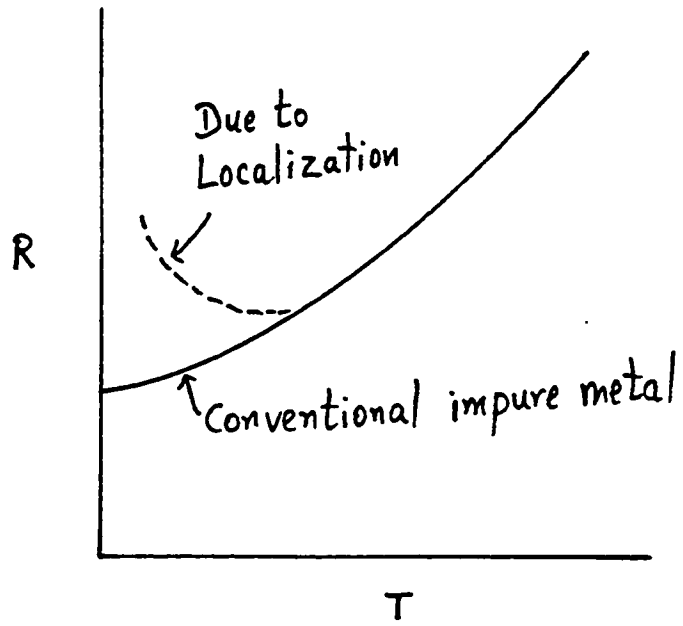

Fig.I-1 Resistance as a function of temperature: The behavior of a conventional impure metal compared to that including localization.

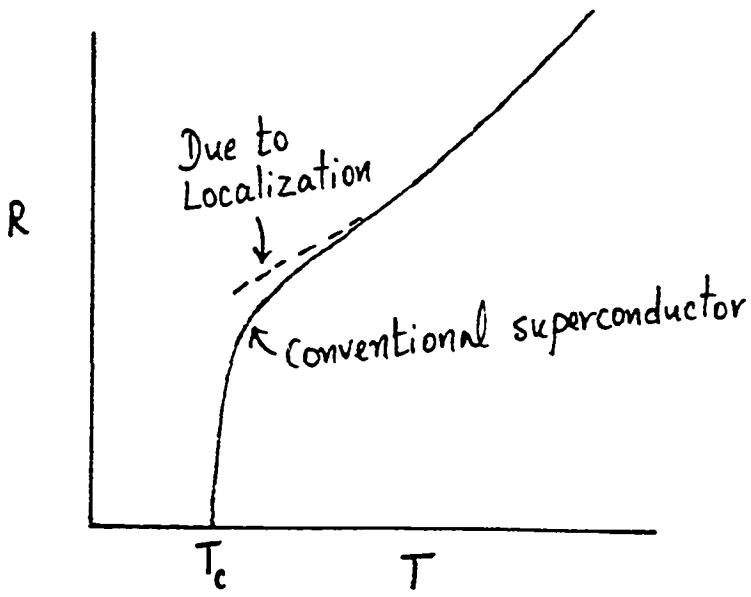

Fig.I-2 Resistance as a function of temperature for a conventional superconductor contrasted with that including localization.

at absolute zero. When the wave function at the Fermi energy becomes localized, we have an insulator. Mott[2] extended these concepts to address the question of the sharpness of the metal-insulator transition.

These ideas on localization were recently revived by Thouless[3] when he predicted that in experiments studying resistance of realistic metal wires at low enough temperatures one should observe an increase in resistance with decreasing temperatures. This behavior is schematically illustrated in Fig. I-1. The fundamental physical idea is that at T=0 K electrons in a disordered metal wire are stuck in localized states. At T=0, electron transport between spatially separated states does not occur, resulting in infinite electrical resistance. At non-zero temperatures the electrical conduction is caused by inelastic scattering events which kick the electrons out of one localized state into another at a different energy. (Note that the Hamiltonian which gives the localized states as eigenstates already includes the potential due to random disorder in it.) As the temperature increases the number of such inelastic collisions increases resulting in less and less resistance. Thouless used scaling arguments to quantitatively estimate the size of the expected effect. At T=0 K, the localization length (characteristic decay length of the envelope of the localized electron wave function) is the relevant scaling length. At non-zero temperatures the inelastic diffusion length ℓ_i is identified as the scaling length. ℓ_i is the rms distance travelled by an electron between two consecutive inelastic collisions. The scaling ideas of Thouless were extended by Abrahams et al.[4] to make quantitative predictions for conductivity in three-, two- and one- dimensional systems. Many experiments have been done in the past six years with a view to verifying these predictions.

The phenomenon of localization has received a much more complete interpretation in the past three years with the development of a detailed microscopic theory [5-7]. Using many body diagrammatic techniques, the original equations of scaling theory for the temperature dependence of conductivity were rederived. In addition, the theory is readily extended to include other perturbations such as magnetic field, spin-orbit interaction and magnetic impurities. These issues are explored further in Chapter II.

It is important to point out that the theory of localization deals only with the quantum correction to the conductivity due to small changes in the electron diffusivity as a result of coherent effects in the presence of disorder; the effects of interactions between electrons are not included.

I-B ELECTRON-ELECTRON INTERACTION

It has been pointed out by Altshuler et al.[8] that electron-electron interaction effects could give rise to changes in conductivity of the same magnitude as localization in disordered metals. The inclusion of the screened Coulomb interaction between electrons in the presence of random disorder introduces changes in the electronic density of states close to the Fermi energy. For example, in the case of Al, E_F = 11.7 eV and the thermal energy (k_BT) at T= 4K is 0.3 meV. Therefore, if changes in the density of states occur on an energy scale larger than 0.3 meV they will be manifested through various physical properties. This causes another quantum correction to the conductivity, in addition to that due to localization. At sufficiently large amounts of disorder there can

actually be a zero of density of states at the Fermi energy, corresponding to a correlation gap.

The theoretical expression for the resistance change as a function of temperature due to electron-electron interaction effects resembles the prediction of the localization theory so closely that other means of distinguishing the two theories had to be developed. The study of magnetoresistance is one such tool; for small magnetic fields, only the localization effects contribute significantly to the magnetoresistance. More discussion of these and related issues can be found in Chapter II. It is now generally agreed that both localization and electron-electron interaction effects exist in real experiments.

I-C SUPERCONDUCTIVITY

If we have a conventional superconductor, the resistance becomes zero at a temperature $T_c > 0$ (Fig. I-2). For perturbations (and defects) that do not violate time-reversal symmetry, superconductivity persists (Anderson's Theorem[9]) with some modifications[10]. If a superconductor is chosen for the study of localization phenomenon (at $T > T_c$), one must also account for the effect of superconducting fluctuations on the conductivity. Just above T_c, superconducting fluctuations are too strong to make a study of localization effects possible. Even well above T_c, the contribution to the resistance from the superconducting fluctuations is not negligible. These fluctuations have to be properly included for a quantitative analysis of the experimental data. The theory of superconducting fluctuations, as relevant to our experiments, is outlined in Chapter II.

I-D MOTIVATION FOR THIS THESIS

This thesis involves experimental work to further our understanding of electron transport in relatively clean ($k_F\ell > 100$) aluminum films. k_F is the Fermi wave vector and ℓ is the elastic mean free path of electrons due to scattering by static defects. In most previous localization experiments, high resistivity films ($k_F\ell \sim 10$) of alloys or quench-condensed metals were studied. When the localization theory was qualitatively found to be correct, the inferred values of the inelastic scattering rates (τ_i^{-1}) were unexpectedly large and could not be explained by 'conventional' inelastic electron scattering mechanisms such as electron-phonon scattering or electron-electron scattering. Hence the credibility of the localization theory was in some question. Also, the mechanism(s) causing these inelastic scattering rates were of interest, and unexplained. We selected relatively clean (i.e. with long electron mean free path) aluminum films for our studies so that the presumably simpler clean-limit localization behavior could first be explored. Also, in the case of aluminum films, other experiments were available for estimates of inelastic scattering rates so that an immediate comparison to the results of localization experiments should be possible.

The large inelastic diffusion length inferred for Al from other experiments and from theory implied that the effects due to localization would be large. In addition, for the study of one-dimensional localization behavior of Al wires, we needed to make wires of width smaller than the inelastic diffusion length. If the intrinsic inelastic diffusion lengths are large, only moderately small wires were needed to see one-dimensional localization effects.

Aluminum is also an attractive material from the material science perspective. It can be easily deposited by thermal evaporation, with reproducible properties. This has proved to be crucial for a clear comparison of various samples.

In this work, we have addressed the theory of localization in many of its aspects. Our first goal has been to study magnetoresistance in two-dimensional aluminum films (with thickness much smaller than ℓ_i) and to understand the delocalization mechanisms (inelastic scattering). We have also used the inferred inelastic scattering rates to explain some 'anomalous' results in prior superconducting experiments. Our own estimates of inelastic scattering rates from the study of non-equilibrium superconductivity in phase-slip experiments on narrow aluminum strips were useful in these comparisons.

The role played by spin-orbit scattering in localization experiments on thin metallic films can not be overemphasized. In our experiments we have looked for a systematic dependence of inferred spin-orbit scattering rate on film quality and found significant correlations.

Most of our localization studies used magnetoresistance, R vs. H data. The study of resistance as a function of temperature can supplement magnetoresistance data to confirm the predictions of the theory more completely. Further, the choice of aluminum gives us an opportunity to also test the predictions of the theory for superconducting fluctuations.

Yet another test for the theory lies in its prediction of magnetoresistance when the magnetic field is parallel to the plane of the film. A strong anisotropy is predicted for magnetoresistance. However, one would expect to infer the same set of scattering parameters, decided only

by the material properties, and independent of the magnetic field orientation used to measure it. This is indeed what we find.

The localization behavior is predicted to change from two dimensional to one dimensional when the sample width also (in addition to the thickness) becomes smaller than the inelastic scattering length. The quantitative understanding of the inelastic mechanisms helps one to look for such a dimensional crossover. An experimental observation of such a cross-over will also confirm the theoretical model. Our samples show such a crossover behavior and also indicate the existence of a second scale length related to spin-orbit scattering.

A final question that requires an answer is whether the scattering mechanisms are different in the narrow wires from those in the thin films. One does expect a change in the dimensionality of the scattering mechanism(s) in narrow enough wires. We addressed this question in our one-dimensional studies.

I-E LITHOGRAPHY

The study of two-dimensional films involved microlithography on the coarse scale. We have made samples of width ranging from $\sim$250 microns down to 2 microns (1 micron = 10^{-4} cm = 10^{4} Å). These samples could be patterned using conventional optical contact lithography in conjunction with optical projection lithography.

For samples that are clearly in the one dimensional regime, we needed submicron width wires. Line widths as small as 0.2 micron can be accomplished using high resolution optical projection lithography for wires with lengths less than 10 microns. Longer wires, L $\sim$ 200μm, are needed to obtain a reasonable signal voltage and to have large enough

sample resistance to make the resistance of the contact pads negligible. Due to unavoidable variations in the width due to exposure changes in the restricted field of view of the projection microscope, alternate procedures had to be developed. The first was a new lithographic process based on optical lithography and a three-dimensional shadowing technique for making $\sim$1000 Å wires. This process had only limited success. In the studies of narrow wires reported in this thesis, the experimental samples were fabricated using an x-ray lithography technique developed and perfected at Yale by S.Wind. Wires as narrow as $\sim$0.1 micron have been fabricated by this technique.

An important approach we have adopted is to prepare narrow wires and the wide films by deposition at the same time so that their material properties are (nearly) the same. Thus, their behavior in various experiments can be directly compared. This has led to some important conclusions on the physical phenomena themselves.

I-F OUTLINE OF THE THESIS

The structure of the thesis is as follows. In this first chapter we have introduced the basic ideas of localization along with its implications for our understanding of electron transport. In Chapter II, we discuss the relevant theoretical predictions for localization and superconducting fluctuations for two dimensional and one dimensional systems. The mechanisms for electron inelastic scattering (resulting in delocalization) and spin-orbit scattering are also briefly outlined. A short account of the non-equilibrium superconductivity theory used for inferring electron inelastic scattering rates from experiments in the superconducting state is also included for completeness. Chapter III

describes the experimental details for sample fabrication and measurement techniques. The details of data analysis and our work on thin films are given in Chapter IV. Comparison of the inferred inelastic scattering rate to the theory and other superconductivity experiments is also done here. Our studies on narrow wires are described in Chapter V. In Chapter VI we discuss the conclusions of localization experiments done by other groups in the light of our results. Chapter VII is the summary of our conclusions along with some suggestions for future work.

II. THEORY

II-A INTRODUCTION

The original predictions of the scaling theory of electron localization have been investigated by microscopic calculations. In addition to confirming the predictions of the scaling theory, the microscopic theory has made it possible to include the effects due to such perturbations as magnetic field or spin-orbit scattering in a formal manner. In this chapter, a brief discussion of these more recent developments in our understanding of the physical phenomenon leading to the localization behavior is given. The treatment follows references 6,7 and 11 .

The theoretical results for the Maki-Thompson superconducting fluctuations are also outlined for the cases of thin films and narrow wires. In addition, the basic theoretical considerations for the inelastic and spin-orbit scattering mechanisms are discussed. A brief summary of the non-equilibrium superconductivity theory needed for the interpretation of the phase-slip experiments in narrow filaments is also given.

The experiments measure the resistance change as a function of temperature or magnetic field. The total resistance at a <u>fixed</u> temperature and magnetic field is

$$R(T,H) = R_o + \Delta R^{Loc}(T,H) + \Delta R^{AL}(T,H) + \Delta R^{MT}(T,H) + \Delta R^{ph}(T) + \Delta R^{el}(H) + \Delta R^{Int}(T,H) \quad (2.1)$$

R_o is the classical (Drude) contribution due to temperature-independent elastic scattering due to static defects. This is the dominant contribution to the overall resistance at the low temperatures of interest to us. The expression for (dc) conductivity for this mechanism (pg.7 of

Ref.12) is given by

$$\sigma_0 = \frac{n e^2 \tau}{m} = \frac{1}{\rho_0} \qquad (2.2)$$

where τ is the impurity scattering time, n is the electron density per unit volume, m is the electron mass and ρ_0 is the resistivity.

The other contributions in Eq.(2.1) are:

(i) ΔR^{Loc} -Localization, (discussed in II-B)

(ii) ΔR^{AL} -Aslamasov- Larkin Fluctuations (II-C)

(iii) ΔR^{MT} -Maki-Thompson fluctuations (II-D)

(iv) ΔR^{ph} -Electron-Phonon scattering (II-E.2)

(v) ΔR^{Cl} -Classical magnetoresistance (II-E.3)

(vi) ΔR^{Int} -Electron-Electron Coulomb Interactions (II-E.4)

We have also assumed that the various contributions in Eq.(2.1) add linearly. In our experiments, any of the terms in Eq.(2.1) is at most 10^{-3} of R_0, so that in calculating fractional changes it will suffice to take

$$\frac{\Delta R}{R} = \frac{\Delta R}{R_0}$$

II-B LOCALIZATION

II-B.1 Introductory Ideas

We consider, as a model of an impure metal, an electron gas in a box with random impurities. The electrons interact only with the impurities and not with each other. The Drude formula for the dc conductivity Eq.(2.2) corresponds to random classical motion of the electron scattered by static defects such as impurities.

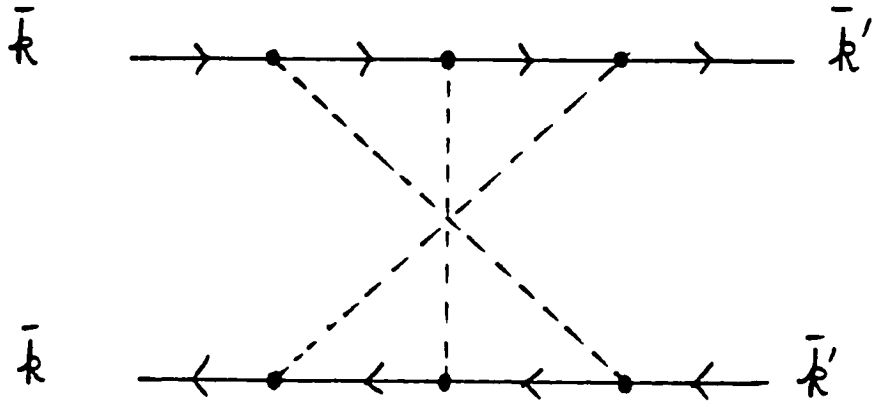

Fig.II-1 An example of a maximally crossed diagram with three intermediate impurity scattering events.

In their calculation of the zero temperature resistivity of a metal as a function of the concentration of impurities, Langer and Neal[13] pointed out the presence of a certain sequence of scattering processes that resulted in divergences in the resistivity. These set of processes correspond to Feynmann diagrams that are called 'maximally crossed diagrams'. They are shown in Fig. II-1. The upper solid line corresponds to an electron propagator with an initial momentum state $\bar{k}$ and a final state $\bar{k}'$ which interacts with impurities at various sites. The lower solid line corresponds to a hole propagator with an initial momentum state $\bar{k}$ and a final state $\bar{k}'$ which interacts with the same impurities.

At each impurity site the electron and the hole undergo equal and opposite changes of momentum in the two series of scattering events. These two scattering sequences are time reversally related. The evaluation of the diagrams (given in detail in Ref.11) gives an estimate of a function $C(\bar{r},\bar{r}')$ that describes the interference between these two scattering sequences. $C(\bar{r},\bar{r}')$ (called the Cooperon) can be interpreted as follows. If we consider an electron starting at a position $\bar{r}$, $C(\bar{r},\bar{r}')$ gives the correction to the probability of finding the electron at a position $\bar{r}'$ due to quantum interference. For the classical diffusion problem it will be zero.

When $\bar{k}+\bar{k}' = 0$ for the two scattering sequences, the interference is maximum. This represents the fact that one needs to couple the states with momenta $\bar{k}$ and $-\bar{k}$ to have a stationary localized state[7]. In addition to coupling to the state of exactly opposite momentum $-\bar{k}$, there are contributions from states with momenta $-\bar{k}+\bar{q}$, for small values of $\bar{q}$.

At T=0, electrons can be trapped in these localized states due to the absence of inelastic scattering mechanisms. This causes the conduc-

tance to reduce to zero. At finite temperatures, the coherence required to form the localized state will last only for a period corresponding to an inelastic scattering time τ_i.

In the following discussion we limit ourselves to the case of dc conductivity in the absence of magnetic impurities.

II-B-2 General Formalism

Case(i) No spin-orbit scattering

Let us first consider the situation when there is no spin-orbit scattering . From detailed theoretical calculations, in the presence of an external magnetic field, $C(\bar{r},\bar{r}')$ can be shown to be the solution of the equation[6,11],

$$\left[D\left(\hat{q} - \frac{2e}{\hbar c}\bar{A}\right)^2 + \tau_i^{-1} \right] C(\bar{r},\bar{r}') = \delta(\bar{r}-\bar{r}') \qquad (2.3)$$

with the boundary condition

$$\left[-i\bar{\nabla} - \left(\frac{2e}{\hbar c}\right)\bar{A} \right]_n C(\bar{r},\bar{r}') = 0 \qquad (2.3a)$$

for the component normal to the boundary of the sample. D is the diffusion constant determined by the elastic scattering and $\bar{A}$ is the magnetic vector potential. Notably Eq.(2.3) corresponds to a particle of charge 2e and a mass $\hbar/2D$ in a magnetic field.

The correction to the conductivity due to localization is given by

$$\Delta\sigma^{Loc}(T,H) = \int d^3r \; \Delta\sigma^{Loc}(\bar{r},\bar{r}) \qquad (2.4)$$

where,

$$\Delta\sigma^{Loc}(\bar{r},\bar{r}') = \frac{-2De^2}{\pi\hbar} C(\bar{r},\bar{r}') \qquad (2.4a)$$

The appearance of $C(\bar{r},\bar{r})$ in Eq.(2.4) can be physically attributed to the fact that we are calculating the change in the conductivity due to the change in the probability of finding the electron at any position r due to quantum interference. The function $C(\bar{r},\bar{r}')$ can be written in terms of the eigenfunctions $\varphi_n(r)$ of the operator in Eq.(2.3) as

$$C(\bar{r},\bar{r}') = \sum_n C_n \varphi_n(\bar{r}) \varphi_n^*(\bar{r}') \qquad (2.5)$$

with

$$C_n = \frac{1}{\varepsilon_n + \tau_i^{-1}} \qquad (2.5a)$$

where ε_n are the eigenvalues of the operator $D[\hat{q} - (\frac{2e}{\hbar c})\ \bar{A}]^2$. Substitution of (2.5) into (2.4) gives, for a set of orthonormal functions $\varphi_n(r)$

$$\Delta\sigma^{Loc}(T,H) = \frac{-2De^2}{\pi\hbar} \sum_n C_n \qquad (2.6)$$

The summation over the eigenvalues is carried out according to the physical situation, e.g., one dimensional or two dimensional sample, etc.

Case(ii) With spin-orbit scattering:

We consider the spin-orbit Hamiltonian[14],

$$\tilde{H}_{so} = \frac{\hbar^2}{4im^2c^2}\ \tilde{\sigma}\cdot(\bar{\nabla}V(\bar{r}) \times \bar{\nabla}) \qquad (2.7)$$

$\vec{\sigma}$ is the electronic spin and V(r) is the (non-magnetic) impurity potential. This Hamiltonian does not violate time-reversal symmetry (pg.90 of Ref.14); but the spin can no longer be considered a conserved quantity. The coherence required for localization is not destroyed by the spin-orbit scattering, but the amplitude of the interference is changed due to spin matrix elements[11,15]. We need some kind of three dimensionality in order for the spin-orbit interaction to be effective. This is because the momenta entering the spin-orbit Hamiltonian (2.7) have been allowed to have unrestricted orientations in a three-dimensional space. It appears that the adequate dimensional condition to use the prescription given below for incorporating the spin-orbit scattering in localization is that the sample size be larger the elastic mean free path ℓ (pg.139 of Ref.15) .

In the presence of spin-orbit scattering, the Cooperon splits up into two parts[6,15]

$$C_n = \frac{3}{2} \frac{1}{\varepsilon_n + \tau_2^{-1}} - \frac{1}{2} \frac{1}{\varepsilon_n + \tau_i^{-1}} \qquad (2.8)$$

with a characteristic time

$$\tau_2^{-1} = \tau_i^{-1} + (4/3)\tau_{so}^{-1}$$

The first term in Eq.(2.8) corresponds to triplet wave functions and the second term corresponds to singlet wave functions for the two particles constituting the Cooperon.

Eq.(2.8) is a result of complex field theoretical calculations; but some similarities to the conventional two electron problem (Helium atom)

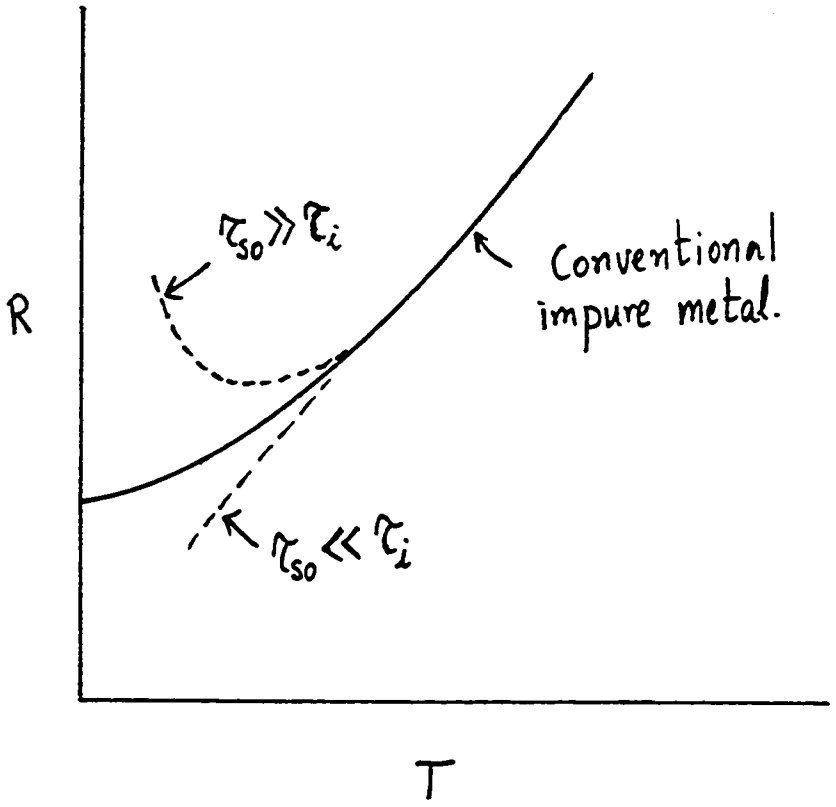

Fig.II-2 Effect of spin-orbit scattering on localization behavior.

in atomic physics[16] can be noted. In the case of ortho-helium, the eigenstate corresponding to the antisymmetric spatial wave function is triply degenerate and the introduction of spin-orbit coupling (even in the non-relativistic theory) removes this degeneracy. In contrast, para-helium has a non-degenerate eigenstate and spin-orbit coupling does not cause any change in the eigenvalue. This observation could be used to understand the appearance of the the spin-orbit rate in the denominator of the triplet term in Eq.(2.8) whereas the singlet term does not have the spin-orbit rate in it.

II-B.3 Qualitative Features of the Theory

The general qualitative results of the localization theory are schematically illustrated in Fig.II-2. We first discuss the temperature dependence of resistance, R(T). For R(T), the microscopic theory predicts the same behavior as described by Fig.I-1 only when the spin-orbit scattering rate is small. However, when the spin-orbit scattering rate is large compared to the inelastic rate the theory predicts that the resistance will decrease with decreasing temperature. The resistance will thus decrease below the classical residual resistance! Such a decreasing behavior of resistance is sometimes referred to as 'Anti-localization' in the literature.

The presence of a magnetic field decreases the amplitude of the Cooperon in general, due to the breaking of the time reversal invariance. In the limit of weak spin-orbit scattering ($\tau_{so}^{-1} \to 0$), such a decrease of $C(\bar{r},\bar{r})$ will bring down the R(T) curve to approach the classical curve. This results in a negative magnetoresistance. In the large spin-orbit scattering limit, the application of a magnetic field will bring the R(T)

curve up to the classical random behavior, resulting in a positive magnetoresistance.

II-B.4 Dimensionality Considerations

As was stated in the last section, the evaluation of the conductivity Eq.(2.6), has to be done for the specific experimental system being considered. For example, if there is an applied magnetic field, the eigenvalues and the eigenfunctions have to be appropriately modified.

The characteristic length scale for deciding the dimensionality of a sample is the inelastic scattering length, if there is negligible spin-orbit scattering in the system. With finite spin-orbit scattering, there is an additional effective scale length

$$l_2 = (D\tau_2)^{1/2}$$

that also decides system dimensionality. D is the diffusion constant given by

$$D = (v_F l/3)$$

with v_F the Fermi velocity. Let us consider a film of thickness d (with the film plane parallel to the x-z plane) such that

$$d < l_i \text{ and } l_2 .$$

Since $(\frac{2\pi}{d} \gg l_i, l_2)$, we can assume that only the $q_y = 0$ eigenstate contributes to the conductivity (see Appendix A). Then the integral prescribed in Eq.(2.6) has to be performed in a two-dimensional q-space. The film under consideration is said to be quasi-two-dimensional with respect to localization behavior.

If we have a wire of width W and thickness d such that

$$d, W < l_i \text{ and } l_2$$

then its behavior will be quasi-one-dimensional. Here, the q-space integration of Eq.(2.6) will be one dimensional because of the additional

assumption that only the state with $q_z = 0$ contributes to conductivity (see Appendix B).

A region of mixed-dimensional behavior for a flat wire is possible

$$d < l_i \text{ and } l_2 \text{ but } l_2 < w < l_i$$

and in this case the triplet term of Eq.(2.8) will behave two dimensionally whereas the singlet term will behave one-dimensionally. In the rest of this thesis, we will use the term two-dimensional to mean quasi-two-dimensional (2D) and similarly for the term one-dimensional (1D).

II-B-5 Definition of Resistance Changes

The magnetoresistance at a temperature T is defined as

$$\delta R(T,H) = R(T,H) - R(T,H=0) \qquad (2.9)$$

It will be helpful in the following sections to note that $\psi(x)$ is the digamma function and has the limiting behavior

$$\psi(1/2 + x) \to \ln x \text{ as } x \to \infty$$

We are also interested in studying resistance as a function of temperature, in a fixed field H. Here one has to choose a reference temperature T_{ref} in order that we can define

$$\tilde{\delta R}(T,H) = R(T,H) - R(T_{ref},H) \qquad (2.10)$$

and the zero field result can be obtained by taking $H \to 0$ limit of Eq.(2.10).

II-B.6 Inclusion of Magnetic Scattering

It is to be emphasized that we have limited our discussion so far to

the case $\tau \ll \tau_i$ and τ_{so}, and we have assumed that there is no magnetic scattering. In the case of Al, the assumption of negigible magnetic scattering is well justified. This is because in dilute concentrations, common magnetic impurities do not have localized magnetic moments in Al[12,28].

However, in general, if there is electron scattering due to magnetic impurities, it will suppress the localization effects. All the theoretical expressions presented here can be generalized[11] to include the magnetic scattering rate τ_s^{-1} by substituting $\tau_i^{-1} + 2\tau_s^{-1}$ for τ_i^{-1}, and $\tau_i^{-1} + (4/3)\tau_{so}^{-1} + (2/3)\tau_s^{-1}$ for τ_2^{-1}.

II-B-7 Results for Two-Dimensional Systems

We consider two experimental situations; namely, the applied magnetic field (i) perpendicular to the plane of the film, and (ii) parallel to the plane of the film. Most experiments are done in the perpendicular field configuration.

Case (i) Perpendicular Fields:

Hikami, Larkin and Nagaoka[5] calculated the contribution to the fractional resistance change due to localization at a given temperature T in the presence of a perpendicular magnetic field H and obtained

$$\frac{\Delta R}{R}^{Loc}(T,H) = \frac{R_\square}{2\pi^2 \hbar/e^2}\left[-\frac{3}{2}\psi\left(\frac{1}{2}+\frac{H_2}{H}\right)+\frac{1}{2}\psi\left(\frac{1}{2}+\frac{H_i}{H}\right)+\ln\left(\frac{H_0}{H}\right)\right] \tag{2.11}$$

where $R_\square$ is the sheet resistance and the characteristic fields are defined by

$$H_o = \frac{\hbar c}{4e l^2} \qquad H_i = \frac{\hbar c}{4eD\tau_i} \qquad (2.11a)$$

$$H_{so} = \frac{\hbar c}{4eD\tau_{so}} \qquad \text{and} \qquad H_2 = H_i + (4/3)\, H_{so}$$

H_o appears in the theory due because in the absence of an external magnetic field, the elastic scattering time is taken to be the shortest time for the Cooperon interference.

Case (ii) Parallel Fields:

When the magnetic field is parallel to the film plane only a perturbation calculation for conductivity is available[17](also see Appendix A). The theoretical result for the contribution to fractional resistance change due to localization is

$$\frac{\Delta R}{R}^{Loc}(T,H) = \frac{R_\square}{2\pi^2 \hbar/e^2}\left[-\frac{3}{2}\ln\left(\frac{H_2}{H}+\frac{H}{48\,H_d}\right)+\frac{1}{2}\ln\left(\frac{H_i}{H}+\frac{H}{48\,H_d}\right) + \ln\left(\frac{H_o}{H}\right)\right] \qquad (2.12)$$

This theory assumes that the thickness of the film is less than the Landau orbit size, $(\hbar c/2eH)^{1/2}$. More aspects of this limitation are discussed in Appendix A. In terms of fields, this would imply that Eq.(2.12) will be correct up to a maximum field of $\sim 12 H_d$ with

$$H_d = \hbar c/4ed^2 \ .$$

II-B.8 Results for One-Dimensional Systems

We assume that the wire is a flat strip of width W and film thickness d, and the magnetic field to be normal to the film. The relevant theory was derived by us[18], and is briefly described in Appendix B. The contribution to the fractional resistance change at fixed T and H is

$$\frac{\Delta R}{R}^{Loc}(T,H) = \frac{R_\square}{\pi \hbar/e^2}\left[\frac{3}{2}\left(\frac{H_W}{H_2}\right)^{1/2}\left(1+\frac{H^2}{48\,H_W H_2}\right)^{-1/2} - \frac{1}{2}\left(\frac{H_W}{H_i}\right)^{1/2}\left(1+\frac{H^2}{48\,H_W H_i}\right)^{-1/2}\right] \quad (2.13)$$

The term multiplied by 3/2 is the 'triplet' term, sensitive to spin-orbit scattering (see Sec.II-B.2). The second (singlet term) is unaffected by spin-orbit scattering. The result above involves the use of perturbation theory in the same sense as that for thin films in parallel field Eq.(2.12). Since the width of the wire is to be compared to the Landau orbit size in this case, the field restriction is $H < 12\ H_W$ where

$$H_W = \hbar c/4eW^2 .$$

We note that if we take $H \to 0$ limit of Eq.(2.13) with $\tau_{so}^{-1} = 0$, we obtain the original result of Thouless[3] for 1-D localization.

II-B.9 Results for Mixed-Dimensional Systems

In this case, the expression (See Appendix B) for the contribution to fractional change in resistance due to localization at fixed T and H (field taken normal to the film plane) is

$$\frac{\Delta R}{R}^{Loc}(T,H) = \frac{R_\square}{2\pi^2 \hbar/e^2}\left[-\frac{3}{2}\psi\left(\frac{1}{2}+\frac{H_2}{H}\right)+\frac{3}{2}\ln\left(\frac{H_0}{H}\right)\right] - \frac{R_\square}{\pi\hbar/e^2}\left[\frac{1}{2}\left(\frac{H_W}{H_i}\right)^{1/2}\left(1+\frac{H^2}{48\,H_i H_W}\right)^{-1/2}\right] \quad (2.14)$$

We note that the mixed-dimensional behavior corresponds to a regime where the triplet contribution [the first term of Eq.(2.14)] is 2D, and the singlet contribution [the second term of Eq.(2.14)] is 1D in nature. In all situations, the singlet term will be larger, and this results in a

positive magnetoresistance. When the spin-orbit rate is very large compared to the inelastic rate, the singlet term by itself is adequate for the interpretation of the data. We expect a sample which shows mixed dimensional behavior at low temperatures to be two dimensional at high temperatures, since at high temperatures $W < l_1$ and l_2.

II-C ASLAMASOV-LARKIN FLUCTUATIONS

The Aslamasov-Larkin (AL) contribution[19] to excess conductivity is due to the direct acceleration of superconducting pair fluctuations above T_c . Many experimental studies[20] in the past 1-1/2 decades have confirmed the existence of this contribution close to T_c. In the case of cleaner films, it was noted[20] that most of the experimentally observed excess conductivity at temperatures well above T_c was due to an indirect (Maki-Thompson) contribution and was not due to the AL term. Since our experiments involve relatively clean aluminum films and are done in the regime $(T/T_c) > 1.3$, we can ignore the AL term in our analysis.

II-D MAKI-THOMPSON SUPERCONDUCTING FLUCTUATIONS

II-D.1 Introduction

The existence of the indirect contribution to the excess conductivity above the transition temperature of a superconductor has been realized for more than a decade[21]. Quasiparticles of approximately zero total momentum are created from the decay of the pair fluctuations. These quasiparticles remain in a state of small total momentum even after scattering from (non-magnetic) impurities due to time reversal symmetry. Hence they continue to be accelerated just as if they were pairs. However, the quasiparticle life time is limited due to various mecha-

nisms. Some of these quasiparticles pair up again. It has been proved experimentally recently[22] that very close to the superconducting transition the recombination of the quasiparticles is the dominant mechanism. But, at temperatures not too close to T_c, inelasic scattering destroys the phase coherence between the quasiparticles. The consequence of the inelastic scattering events is, thus, to restrict the contribution to conductivity from the correlated quasiparticles of near zero total momentum from diverging. This attribute is similar to the role played by inelastic scattering in the localization behavior where the inelastic scattering prevents the conductivity from going to zero. We note that spin-orbit scattering does not violate time-reversal symmetry and it is not expected to play a role in the MT contribution.

It is clear that the quasiparticles will interact with each other through the Cooper interaction and hence the Maki-Thompson term explicitly requires an interaction between the quasiparticles to be included in the theory. This is to be contrasted with the localization contribution which assumes non-interacting electrons.

II-D.2 General Formalism

The evaluation of the particle-particle propagator corresponding to the MT contribution has been worked out in detail by Larkin[23] and more recently by Lopes dos Santos and Abrahams[24].

As a result of these relatively involved calculations, they arrive at the equation for conductivity in the limit[24] $k_B T \ln(T/T_c) \gg \hbar/\tau_i$

$$\Delta\sigma^{MT}(T,H) = \frac{-2De^2}{\pi\hbar}\beta(T/T_c)\sum_n \frac{1}{\varepsilon_n + \tau_i^{-1}} \qquad (2.15)$$

$\beta(T/Tc)$ is the parameter characterizing the strength of the interaction between electrons and has been tabulated by Larkin (see Appendix G). As $T \to T_c$, $\beta(T/Tc)$ diverges. It is also important to note that $\beta(T/Tc)$ is independent of localization dimensionality. We should note that this form resembles the contribution for localization in the absence of spin-orbit scattering [Eq.(2.6)] except for the difference in the sign and the appearance of the parameter $\beta(T/T_c)$. If there is an applied magnetic field, Eq.(2.15) is only valid in the limit[24] $4DeH/c \ll k_BT\,\ell\eta(T/T_c)$. The eigenvalues and the corresponding eigenfunctions, as in the case of localization, depend on the physical case under consideration- for example, the presence or absence of an external magnetic field. Also, as discussed in Appendix C, the cut-off energies deciding the upper limits of the integrations are different for the localization and MT contributions. In addition, $\beta(T/T_c)$ can itself be a function of τ_i in general[24] and we are restricted to yet another limit, namely, $\hbar/(k_BT\tau_i) \ll 1$ to ignore such a dependence.

II-D.3 Qualitative Features of the Theory for MT Fluctuations

The effect of the MT fluctuations is to decrease the resistance of the material even at temperatures much above T_c. Application of a magnetic field reduces the strength of the MT fluctuations, yielding positive magnetoresistance.

II-D.4 Dimensionality Considerations

The summation of Eq.(2.15) implies the inelastic diffusion length to be the characteristic length for deciding the dimensionality of MT fluctuations. Hence if

$$d < \ell_i$$

the sample will be quasi-two dimensional and if

$$W,\ d < \ell_i$$

it will be quasi-one dimensional.

II-D.5 Results for Two Dimensional Systems

Case(i) Resistance as a function of temperature (H=0)

For the quasi-two dimensional case, in the absence of an external magnetic field, the fractional contribution to the resistance at a given temperature T is given by[15]

$$\frac{\Delta R}{R}^{MT}(T, H=0) = \frac{R_\square}{2\pi^2\hbar/e^2}\left[-\beta(T/T_c)\ \ln\left\{\frac{k_B(T-T_c)}{\hbar}\tau_i\right\}\right] \tag{2.16a}$$

Case(ii) Perpendicular Fields

The fractional change in resistance at a given temperature T and magnetic field H is[23]

$$\frac{\Delta R}{R}^{MT}(T,H) = \frac{R_\square}{2\pi^2\hbar/e^2}\ \beta(T/T_c)\ \psi\left(\frac{1}{2}+\frac{H_i}{H}\right) \tag{2.16b}$$

The magnetoresistance can be defined as before through Eq.(2.9). If we want to study R(T) in the presence of a magnetic field, we can use Eq.(2.10).

Case(iii) Parallel Fields

The contribution to the fractional change in resistance in a parallel field is[26]

$$\frac{\Delta R}{R}^{MT}(T,H) = \frac{R_\square}{2\pi^2 \hbar/e^2}\,\beta(T/T_c)\,\ln\left(\frac{H_i}{H} + \frac{H}{48\,H_d}\right) \qquad (2.17)$$

Eq.(2.9) gives the magnetoresistance.

II-D.6 Results for One Dimensional Systems

In Appendix C, we have derived the result[18] for the contribution to the fractional change in resistance from MT fluctuations for quasi-one dimensional systems. We have assumed that the magnetic field is applied perpendicular to the plane of the film. The calculation is valid in the limits discussed in detail under Section II-D.2 . In addition, similar to the predictions of the localization theory for one-dimensional systems [Eq.(2.13) and (2.14)] the theory of MT fluctuations for 1D systems can also be used only for fields $H < 12\,H_W$.

The fractional change in resistance due to MT fluctuations at a given temperature and in a perpendicular field H is

$$\frac{\Delta R}{R}^{MT}(T,H) = -\frac{R_\square}{\pi \hbar/e^2}\,\beta(T/T_c)\left[\left(\frac{H_W}{H_i}\right)^{1/2}\left(1 + \frac{H^2}{48\,H_i H_W}\right)^{-1/2}\right] \qquad (2.18)$$

The magnetoresistance can be defined as before. R(T) can be obtained through Eq.(2.10). It is to be reiterated that this calculation assumes $\hbar/\tau_i \ll k_B T \ln(T/T_c)$.

II-E OTHER CONTRIBUTIONS TO RESISTANCE

II-E.1 Introductory Considerations

In addition to the three contributions (localization, AL fluctuations and MT fluctuations) discussed previously, there are three other contributions to resistance. These are: (1) the classical electron-phonon

contribution to resistance as function of temperature and (2) classical magnetoresistance and (3) electron-electron interactions (corresponding to Feynmann diagrams of both particle-particle and particle-hole types). The electron-phonon contribution to R(T) and the classical magnetoresistance are not discussed in most works in localization because of the fact that in the dirty systems other workers have studied, the other contributions are much larger than these two. Due to the relatively clean nature of our samples (with longer elastic mean free paths), we discuss these two terms also in some detail.

II-E.2 The Electron-Phonon Contribution to R(T)

The standard text book result (Bloch-Gruneisen Law, See for example in pg.214 of Ref.14)

$$\Delta R^{ph}(T) \propto T^5 \tag{2.19}$$

for $T \ll \theta_D$ (θ_D is the Debye temperature). This form is due to the restrictions on scattering angles at $T \ll \theta_D$. T^5 behavior is seldom observed in experiments[26,27]. However, for aluminum the previous experiments indicate[26]

$$\Delta R^{ph}(T) \propto T^3 \tag{2.19a}$$

This dependence of resistance on T^3 in Al [instead of Eq.(2.19)] is due to the dominance of electron-phonon umklapp scattering at large angles even at low temperatures. As we shall see in Chapter IV, our results confirm this behavior.

II-E.3 Classical Magnetoresistance

The effect of magnetic field on the electron orbits in solids is discussed in most text books(eg. pg.238 of Ref.12). In the case when τ is shorter than τ_i, one expects this magnetoresistance to be temperature independent. From a two band model (pg.250 of Ref.28) for $\omega_c\tau \ll 1$ (ω_c= eH/mc is the cyclotron frequency), one obtains for Al (see Appendix D)

$$\frac{\Delta R}{R}(H) = 0.23\,(Hl)^2 \qquad (2.20)$$

with H in gauss and l in cm.

II-E.4 Electron-Electron Interaction

The MT term, discussed in Section II-D, involves the study of the influence of temperature and magnetic field on the correlated motion of two electrons with a total momentum of approximately zero, even in the absence of changes in the density of states . Since superconductivity influences the interaction between the two electrons, the parameter $\beta(T/T_c)$ of Eq.(2.15) represents the strength of this increased interaction. $\beta(T/T_c)$ diverges as $T \rightarrow T_c$. As observed before, the MT term is sensitive to weak magnetic fields.

In contrast, there exists a quantum correction to conductivity due to electron-electron interactions which gives a change in the density of states. This is a result of orbital effects due to electron-electron interaction[8,15]. The theoretical expression for R(T) from this theory closely resembles that from the localization theory except that the interaction theory has a characteristic time of $(\hbar/k_BT)$ instead of the τ_i of the localization theory. Since in our samples $(\hbar/k_BT) \ll \tau_i$,

the interaction term is much smaller than the localization contribution and can be neglected.

The characteristic field for the electron-electron interaction is[6]

$$H_{int} = \frac{\pi c k_B T}{2eD} \approx 1.34 \times 10^4 \left(\frac{T}{D}\right) \qquad (2.21)$$

For our sample parameters this would imply fields that are at least 100 times larger than inelastic scaling field H_i. We estimate the magnetoresistance due to the orbital effects of electron-electron interaction (using the theory of Altshuler et al.[6]) to be at least one order of magnitude smaller at any temperature and therefore we neglect it in the analysis.

We should note that there could also be a contribution to magnetoresistance due to spin effects[29] for applied fields comparable to

$$H_{sp} = \frac{k_B T}{g\mu_B} \approx 7.5 \times 10^3 \, T \text{ Gauss.} \qquad (2.21a)$$

As is obvious from Eq.(2.21a), $H_{sp} > 10$ kG in our experimental situations. An estimate of this contribution shows that it is more than two orders of magnitude smaller than the localization and MT contributions in our samples. Hence, we need not include the interaction term due to spin effects in our analysis either.

II-F MECHANISMS OF INELASTIC SCATTERING

The mechanism(s) causing delocalization of electrons has been an issue for which the theoretical understanding is continuing to evolve. In general, one is looking for a process(es) that destroys the phase

coherence required for the Cooperon. We discuss, in some detail, three mechanisms relevant to our experiments. In our discussion we use 'inelastic' to imply 'a process causing delocalization'. We will indicate any subtle differences between processes that destroy phase coherence of the Cooperon and processes that change the energy of a single quasiparticle.

II-F.1 Electron-Phonon Scattering

There have been many estimates of the electron-phonon scattering rates in metals (see for example, Schmid[30]). Most of these calculations assume simple models for electron-phonon interaction and do not account for the detailed differences in the electron-phonon interaction in various metals, such as band structure. However, in the case of Al, Lawrence and Meador[31] calculated the electron-phonon scattering rate using realistic electron wave functions and band-structure details of Al. We use their theoretical result in our discussions for comparison. Lawrence and Meador obtained for clean, bulk Al a value for the electron-phonon inelastic rate at the Fermi energy

$$\tau_{ep}^{-1} = 0.91 \times 10^{7}\, T^{3} \equiv A_3^{Th}\, T^{3}. \qquad (2.22)$$

The above result is obtained after dividing the Lawrence & Meador value of $1.3 \times 107\ T^3$ by the mass enhancement factor 1.4 as suggested by Eq.(25) of Ref.31. We note that the inelastic scattering processes that are relevant for localization experiments occur within an energy shell of width $(\hbar/\tau_i)$ at the Fermi surface. Since $\hbar/\tau_i \ll k_B T$, it is appropriate to use τ_i at the Fermi energy for comparison to our experiments.

The theory of Lawrence and Meador for Al has been tested by other workers for its quantitative validity. Using surface Landau levels (surface skipping orbits), Wegehaupt and Doezema[32] measured the electron-phonon scattering rates at various points in the Brillouin zone in single crystal Al. Gasparov and Harutunian[33] measured radio-frequency size effects in Al. These experiments probe properties averaged over specific orbits on the Fermi surface. The experiments found quantitative agreement with the theory of Lawrence and Meador.

The calculation of Lawrence and Meador is for the clean limit of electron-phonon scattering corresponding to

$$q_{ph}\ell \gg 1$$

where q_{ph} is the typical phonon wavevector. As will be discussed in Chapter IV our samples, by and large, are in this limit.

We point out that while there is consensus among theorists that the clean limit bulk electron-phonon scattering rate should go as T^3 , the expected behavior for dirty limit($q_{ph}\ell<1$) electron-phonon scattering is still controversial. A rate proportional to T^4 has been proposed by Schmid[30,34] and by Thouless[3]. According to Schmid's model there is an increase in the coupling of electrons to transverse phonons with decreasing value of ℓ; the coupling to transverse phonons vanishes in the pure metal. But, Lawrence and Meador estimate that about 80% of the contribution to electron-phonon scattering comes from transverse phonons even in the case of pure aluminum. Thus the results of Schmid's model do not seem to be strictly applicable for the case of Al. Two other theoretical calculations due to Takayama[35] and Kagan et al.[36] predict an electron-phonon rate in dirty systems proportional to T^2. Our present

experiments do not probe this limit and so we shall not discuss the differences among these theoretical predictions.

The dimensionality of electron-phonon scattering is generally decided by comparing the physical dimensions of the sample to the typical phonon wavelength. Transverse phonons are the dominant scatterers of electrons in Al. The most probable phonon wavelength at any temperature is given by[37]

$$\lambda_{ph} = \frac{\pi \hbar v_s}{2 k_B T}$$

Using $v_s = 3.04 \times 10^5$ cm/sec for the transverse sound velocity, we obtain $\lambda_{ph} = (726/T)$ Å, with T in K.

A second possible choice for the dimensionality criterion is based on the Pippard-Ziman condition[38] which states that phonons of wavelength larger than the electron mean free path are inefficient scatterers. Thus the electron mean free path can be expected to decide the dimensionality of electron-phonon scattering. In the case of thin films on solid substrates good adhesion of the films to the substrate enhances the three dimensionality. Aluminum films on glass (SiO_2) have been calculated to have satisfactory matching for phonon transmission[39] .

II-F.2 Electron-Electron Scattering of Quasiparticles

The standard text book result for the electron-electron scattering rate[12] (proportional to T^2) is for clean ($\hbar/\tau < k_B T$) metals in the bulk. Lawrence and Wilkins[40] have calculated the quasi-particle electron-electron life times in clean bulk Al. There have been calculations by Schmid[41] and Altshuler et al.[42] for bulk, dirty ($\hbar/\tau > k_B T$) systems. Our films are in the dirty-limit for the electron-electron

interaction (viz. $\hbar/\tau > k_BT$), but have film thicknesses that are much smaller than the electron-electron interaction length

$$l_{int} = (\hbar D/k_BT)^{1/2}.$$

This makes our films two-dimensional with respect to electron-electron interaction. Thus the calculations done for the bulk systems are not of relevance to us.

Abrahams et al.[43] calculated the life time for a quasi-particle in a dirty two dimensional system. They predicted

$$\tau_{ee}^{-1} = \frac{1}{2\pi} \frac{R_\square}{\hbar/e^2} \frac{k_BT}{\hbar} \ln(T_1/T). \qquad (2.23a)$$

$T_1 = 9 \times 10^5 (k_F l)^3$ for Al. This result has been extensively used in the literature, including our publications[44-46]. Subsequently, Lopes dos Santos[47] reevaluated τ_{ee}^{-1} self-consistently and obtained

$$\tau_{ee}^{-1} = \frac{1}{4\pi} \frac{R_\square}{\hbar/e^2} \frac{k_BT}{\hbar} \ln(4T_1/T) \qquad (2.23b)$$

instead of (2.23a). Altshuler et al.[42] have predicted a result

$$\tau_{ee}^{-1} = \frac{1}{4\pi} \frac{R_\square}{\hbar/e^2} \frac{k_BT}{\hbar} \qquad (2.23c)$$

for dirty 2D systems [without the logarithmic factor of Eq.(2.23b)].

In the above theoretical results the typical energy for electron-electron interaction is $\sim k_BT$ and hence, l_{int} is the relevant length

scale for deciding the dimensionality of the electron-electron scattering due to this mechanism.

II-F.3 Electron-Electron Scattering Rate for the Cooperon Interference Effect

Fukuyama and Abrahams[48] calculated the life-time of the Cooperon interference (discussed in Sec.II-B.1) τ_ε explicitly including dynamically screened electron-electron interaction and obtained the same result as Eq.(2.23a). i.e.

$$\tau_\varepsilon^{-1} = \frac{1}{2\pi} \frac{R_\square}{\hbar/e^2} \frac{k_B T}{\hbar} \ln(T_1/T) \qquad (2.24)$$

Altshuler et al.[49] (and recently Eiler[50]) have calculated the effect of electron-electron scattering events with energy transfers small compared to k_BT (also called the interaction of electrons with electromagnetic fluctuations) on the phase relaxation of the Cooperon. Their results indicate that in reduced dimensionality (2D and 1D) the rate, τ_ε^{-1}, due to this mechanism can be large. In the case of 2D systems (such as our thin films), the theoretical prediction is

$$\tau_\varepsilon^{-1} = \frac{1}{2\pi} \frac{R_\square}{\hbar/e^2} \frac{k_B T}{\hbar} \ln\left(\frac{\pi\hbar/e^2}{R_\square}\right) \equiv A_1^{Th} T \qquad (2.25)$$

The criterion for two dimensionality for the use of Eq.(2.25) is

$$d < \left[\frac{2\pi(\hbar/e^2)}{\rho_0} \left(\frac{\hbar D}{k_B T}\right) \frac{1}{\ln\left(\frac{\pi\hbar/e^2}{R_\square}\right)} \right] \qquad (2.25a)$$

in addition to[49] $d < \ell_{int}$. For our films, Eq.(2.25a) requires $d < 0.1$ cm. The value of τ_ε^{-1} of (2.25) is smaller than τ_ε^{-1} of Eq.(2.24) by

approximately a factor of two in our samples. Very recently, Fukuyama[51] has attempted to clarify the differences in the evaluations of Eq.(2.24) and (2.25). According to his conclusions, it is Eq.(2.25) that correctly describes the decay rate of the Cooperon due to electron-electron interaction for two dimensional systems.

In case of 1-D systems, τ_ε^{-1} is estimated to be[49]

$$\tau_\varepsilon^{-1} = \left[\frac{R_\square}{\hbar/e^2} \left(\frac{k_B}{\hbar} \right) \frac{1}{W} \sqrt{\frac{D}{2}} \right]^{2/3} T^{2/3} \tag{2.26}$$

with the requirement to be one-dimensional that

$$W < \left[\frac{\hbar/e^2}{R_\square} \left(\frac{\hbar D}{k_B T} \right) \frac{1}{\pi\sqrt{2}} \right]^{1/2} \tag{2.26a}$$

In our comparison to experiments we will use Eq.(2.25) and Eq.(2.26) as the relevant expressions for the phase relaxation rate due to electron-electron interaction, 2-D and 1-D systems respectively.

II-F.5 Other Mechanisms

In the case of amorphous systems Black et al.[52] calculated an inelastic time due to the existence of two energy levels. Some experiments in highly disordered systems of metal films[53] compared their results to that prediction. It is not clear as to how relevant this mechanism is in our polycrystalline metal films. There is presently no clear experimental evidence for this mechanism in reported localization studies.

II-G Spin-Orbit Scattering

The origin of spin-orbit scattering in thin metal films has been an interesting puzzle for more than a decade[54,55]. The utility of the localization experiments is that, from the analysis of the experimental data, one can relatively easily infer the spin-orbit scattering time in metal films.

Abrikosov and Gorkov[54] estimated based on a simple scattering theory that

$$\left(\frac{\tau}{\tau_{so}}\right) \approx (\alpha Z)^4 \qquad (2.27)$$

where α (~1/137) is the fine structure constant and Z is the atomic number of the metal. An ideal,infinite crystal does not have scattering of any kind. Deviations from ideality, impurities, boundaries and defects, are responsible for elastic scattering and also for spin-orbit scattering. Hence it is plausible that in the metallic limit that the spin-orbit scattering rate should scale with elastic scattering rate. If the elastic scattering is caused by vacancies in the lattice or by boundary scattering Z could be expected to be that of the metal. For Al, Z=13 so that

$$\left(\frac{\tau}{\tau_{sc}}\right) = 0.8 \times 10^{-4}$$

If the elastic scattering is due to bulk impurities, as is likely to be in many experiments, one would expect the atomic number of the impurity to enter the picture. We will compare the various experimental results for the spin-orbit scattering in Al in Chapter IV.

II-H NON EQUILIBRIUM SUPERCONDUCTIVITY

II-H.1 Introduction

The study of non-equilibrium processes in the superconducting state can yield useful information about the inelastic scattering mechanisms in superconductors. A comparison between the inelastic scattering rates inferred from localization experiments and those from non-equilibrium superconductivity experiments can confirm if the same inelastic processes participate in these experiments.

We shall briefly state the results of the Bardeen-Cooper-Schrieffer (BCS) theory[56] on the nature of the elementary excitations in the superconducting state. Due to the phonon-mediated electron-electron attraction there is an energy gap Δ created at the Fermi energy. In other words, to break a Cooper pair and create two quasiparticles at the Fermi surface, an energy 2Δ is needed. In the BCS model of a superconductor, the quasiparticle excitation energy in the superconducting state is given by[56]

$$E_k = \left(\Delta^2 + \xi_k^2\right)^{1/2} \tag{2.28}$$

ξ_k is the energy of the quasiparticle state k in the normal metal measured relative to the Fermi energy. BCS theory calculates[56] as a function of temperature close to T_c to be

$$\Delta(T) = 1.74\ \Delta(0)\left(1 - T/T_c\right)^{1/2} \tag{2.28a}$$

where $\Delta(0) = 1.764\ k_B\ T_c$.

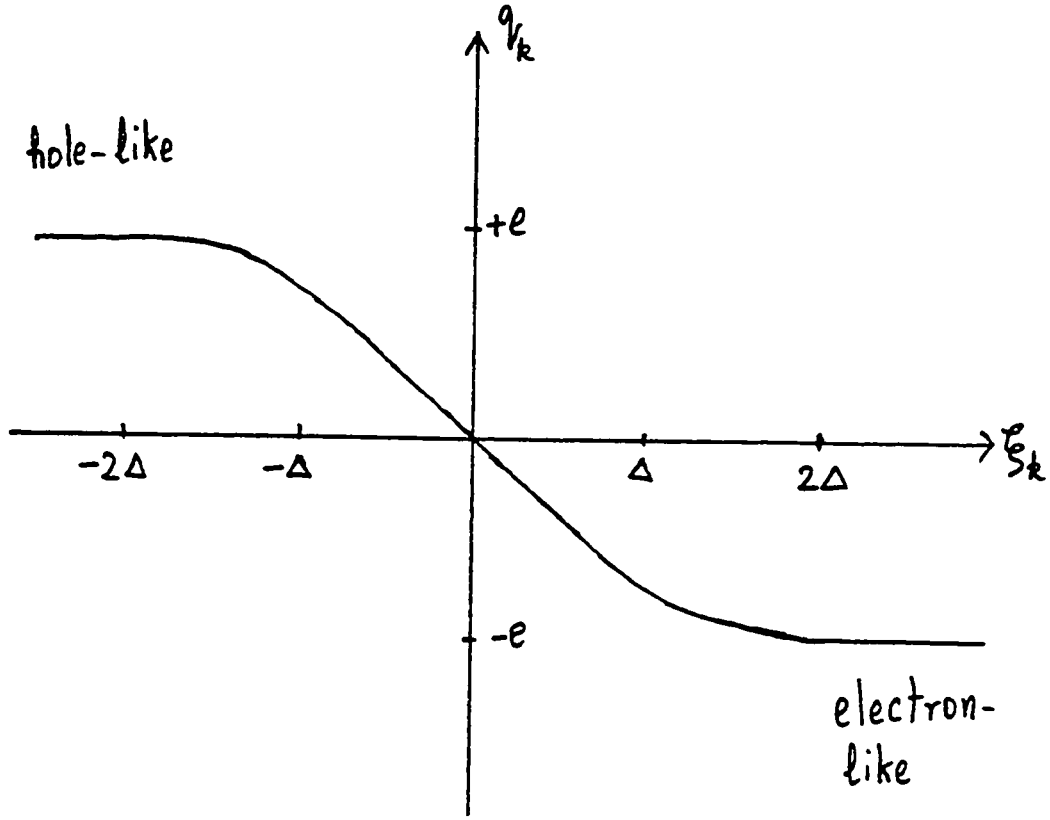

Fig.II-3 Effective quasiparticle charge q_k in the superconductor as function of the normal state quasiparticle energy ξ_k with respect E_F. Only asymmetric quasiparticle excitations create charge imbalance.

In the description of the various properties of superconductors, a two fluid model has been extensively used. The idea is to consider the real system as consisting of two coexisting fluids (i) a normal fluid comprising the quasiparticles and (ii) a superfluid comprising the Cooper pairs. The chemical potentials of the two fluids are equal in the equilibrium situation. When the chemical potentials are not equal, the superconductor is said to be in a non-equilibrium state.

Pethick and Smith[57] have considered the total charge of the system in terms of the two fluid model. From a detailed consideration, they obtain an energy dependent effective charge for the quasiparticles. We show this dependence in Fig.II-3. Quasiparticles far above the Fermi energy have the full electron-like charge of -e whereas quasiparticles far below the Fermi energy have the full hole-like charge of +e . Only symmetric excitations of quasiparticles above and below E_F can maintain the charge of the normal fluid unchanged. For asymmetric excitations, there is a net contribution from the normal fluid to 'charge imbalance'. To maintain overall electrical neutrality, there must be a compensating change in the number of electrons in the condensed state. This implies that the chemical potentials of the superfluid and the normal fluid must shift in opposite directions from their common equilibrium value resulting in a non-equilibrium situation. Such a situation of non-equilibrium is generated only by charged perturbations (e.g. particle injection, or a conversion of supercurrent to normal current as at a normal-superconductor boundary).

II-H.2 Inferring τ_i from charge imbalance relaxation

Schmid and Schön[58] have derived an expression relating the charge imbalance relaxation rate $\tau_{Q^*}^{-1}$ in such a situation and the inelastic

scattering rate at E_F by solving the Boltzmann equation to first order in Δ/k_BT_c (which is valid for $T \sim T_c$). They obtain,

$$\tau_{Q^*}^{-1} = \frac{\pi}{4} \frac{\Delta}{k_B T_c} \tau_i^{-1}(E_F) \qquad (2.29)$$

This result can be understood physically as follows. As seen in Fig.II-3, the maximum change of the effective charge in the normal fluid will occur when a quasiparticle gets scattered from far above E_F to far below E_F or vice versa. However, the probability for occupancy of the initial state or the vacancy at the final state is always so small that such large-energy scattering events are not the most important ones in causing charge relaxation. Instead, of all the inelastic scattering occuring near E_F, only a fraction Δ/k_BT of those scattering events cause significant relaxation of quasiparticle charge imbalance.

II-H.3 Tunneling-Injection Experiments

Clarke and colloborators[59,60] have used a tunnel injection method to determine the charge imbalance relaxation rate in superconducting films. In this method a Normal-Insulator-Superconductor (NIS) tunnel junction injects quasiparticles into the superconductor. The difference in the electrochemical potentials of the non-equilibrium region (where the injection was done) and the equilibrium region of the superconductor was detected by a second NIS junction that did not draw any current. Chi and Clarke[60] have done these experiments on aluminum films, and we will refer to their results in Chapter IV.

II-H.4 Phase-Slip Centers in Narrow Filaments

Now, we consider a thin superconducting wire[61] of transverse dimensions smaller than the superconducting coherence length $\xi(T)$ and the

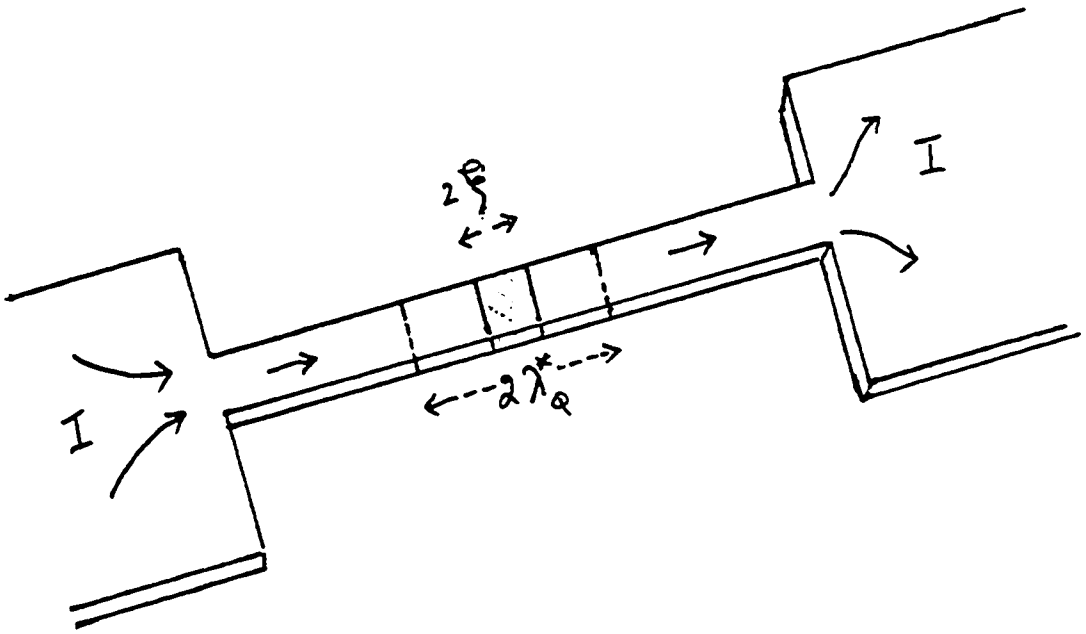

Fig.II-4 The schematic of a phase-slip center. The core of the center extends over a length $2\xi(T)$ and the charge imbalance extends over $2\lambda_{Q^*}$.

penetration depth $\lambda(T)$ of the material. For such a wire the superconducting order parameter and current density are uniform across the cross-section. The experiment on phase-slip centers involves a gradual increase in the bias current from zero. Due to local inhomogeneities in the sample, we can imagine that there is one point where the critical current is the lowest. As the bias current is increased above this minimum critical current, it is no longer possible to find a zero voltage (fully superconducting solution) and a finite electric field appears. This accelerates the supercurrent above the critical velocity (corresponding to the critical current) resulting in the collapse of the order parameter. The entire current must then be carried as a normal current; this in turn allows the superconductivity to reappear, and the cycle repeats. Since there is a voltage drop across this center, the phase of the superconducting order parameter must be increasing at different rates on the two sides of it. Thus, the center is called a Phase-Slip Center (PSC). A schematic of a single phase-slip center is shown in Fig.II-4.

Far from the PSC, the equilibrium situation has to pertain. The distance over which equilibrium is reestablished is the length over which the chemical potential difference between pairs and quasiparticles (discussed in Section II-H.1) becomes zero. So we deduce that the length of the non-equilibrium region near a PSC is equal to twice the charge imbalance relaxation length

$$\lambda_{Q^*} = (D\tau_{Q^*})^{1/2}$$

The factor two comes from the two sides of the PSC. The differential resistance associated with a single PSC is, therefore,

$$R_d = \frac{dV}{dI} = 2\lambda_{Q^*}\left(\frac{\rho_0}{A}\right) \tag{2.30}$$

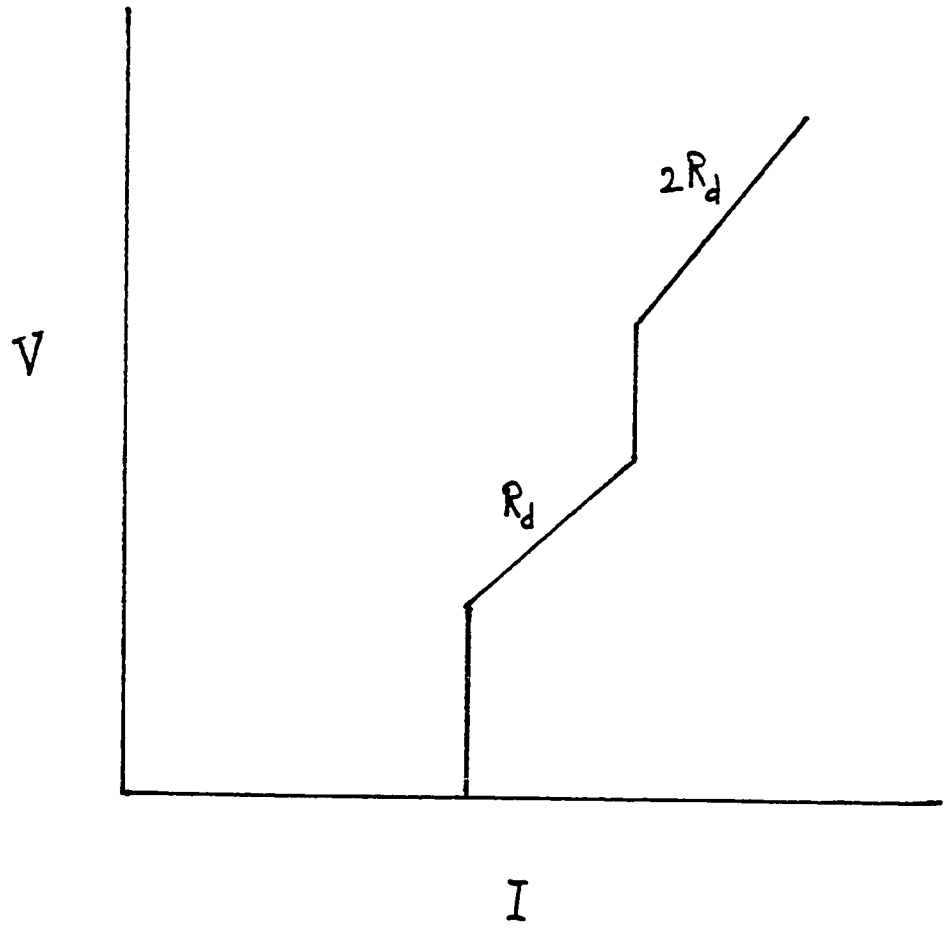

Fig.II-5 The schematic of the step-like structure expected due to the formation of two non-interacting phase-slip centers in a long filament.

where A is the area of cross section of the filament.

In a long filament there are various locations where such a Phase-Slip Center can occur. The voltage measured across the sample increases abruptly at the value of current when each new phase-slip center is created. In the simplest case, one assumes that the distances between the PSCs are large enough to avoid interactions between them[62]. Then, the step structure, schematically shown in Fig.II-5, is expected to have its differential resistance increased in units of a minimum value R_d, which itself corresponds to the single PSC mentioned above.

In Chapter IV, we will refer to our experiments which measured the charge imbalance relaxation rate in aluminum by studying the phase slip centers. A more direct way of measuring the chemical potential difference between the Cooper pairs and quasiparticles as a function of position is to place tunneling probes along the length of the wire[63,64].

III. EXPERIMENTAL TECHNIQUES

The important experimental components required for our study of localization in clean aluminum films were the following:

(1) A technique for depositing aluminum with reproducible properties

(2) The use of optical lithography for patterning samples of moderately small sizes with the required geometry

(3) An advanced method of fabrication for wire samples narrower than 1 micron, for the study of 1D localization

(4) Measurement of changes in resistance with a resolution of a part per million

(5) A low temperature set-up capable of reaching temperatures of $T \sim 1.2K$ with a provision for static magnetic fields of moderate strengths ($H < 10kG$)

In items 1,3 and 4, we made significant advances over the state-of-the-art that existed at Yale at the beginning of this work. We discuss all these techniques in this chapter.

III-A SCANNING ELECTRON MICROSCOPY

We have extensively used Scanning Electron Microscopy (SEM) to observe photoresist structures, metal films and narrow wires. The microscope used most frequently in this work was an ETEC Autoscan operated by Dr. Alan Pooley in the Peabody Museum at Yale. Typically, we coated samples with a thin $\sim 100\text{Å}$ Gold-Palladium layer to enhance secondary electron emission from the sample. In the case of insulating samples, such as photoresist profiles, the coating also reduced charging of the

sample. Magnifications as high as 100,000 were used. More recently, we have used the SEM Model ISI-SS 60 for observing the samples. This microscope is in the Applied Physics Section.

III-B FILM DEPOSITION

The use of resist lift-off (discussed in III-D) in the fabrication of samples requires a directional deposition technique, such as thermal evaporation. Film depositions in the early stages of this work were done in a Kinney vacuum system which had a base pressure of $\sim 10^{-6}$ Torr after several hours of pump down. More recently, a Varian vacuum station with an ability to reach $\sim 10^{-6}$ Torr pressure range in about half an hour has been available. The film thickness was measured by a calibrated quartz-crystal monitor from R.D. Mathis[65].

For aluminum deposition, we found heating a tungsten filament wound tightly with a 99.999% pure Al wire[66] to be the most efficient method. Occasionally tantalum boats were also used for the Al deposition. The evaporation rates ranged from 2 Å/sec to 20 Å/sec depending on the quality of films desired; cleaner films resulted from larger rates. In the study of narrow wires, we deposited wide films at the same time (codeposition) for comparison of film properties.

In addition to aluminum, the other metals of interest (for lithographic purposes) were chrome and gold. The source for the deposition of chrome was a chrome plated tungsten rod. Gold films were used in the fabrication of the mask for x-ray lithography by S. Wind. A gold wire wound around a tungsten filament was heated as the source. A thin $\sim$100Å chrome film was deposited prior to the Au film, in the same pump down, to improve the adhesion of gold to substrate.

III-C REACTIVE ION ETCHING

A useful tool for transferring submicron-size patterns is Reactive Ion Etching (RIE). The initial set-up for the RIE system was designed by Professor S. Grodzinsky (then visiting Yale from University of New Haven). Subsequently it was assembled and characterized by D. Face. Further details on RIE will be available in D.Face's thesis.

In the RIE system, a standard diffusion pumped Cooke vacuum system (with a base pressure of $\sim 1 \times 10^{-6}$ Torr) was used. A MKS^{66a} Model 254 (three channel) gas flow controller with feedback control and an option to operate at a fixed chamber pressure (or at a given gas flow rates) was connected to the vacuum chamber. The RF power from a standard generator ($\sim$ 14MHz) was capacitively coupled to water cooled electrodes in a parallel plate configuration. The substrate sat on a silicon plate that covered the bottom electrode. The bottom electrode was powered by the RF. The upper electrode was unpowered but not grounded. Oxygen was chosen for etching organic polymers (such as photoresist). The RF source enhanced the ionization of the etching gas. The principle behind the etching process was an anisotropic gas-phase chemical reaction between the etching gas molecules and the organic polymer, which resulted in volatile products that were pumped away from the chamber. Under typical operating conditions, with oxygen partial pressure $\sim 3 \times 10^{-3}$ Torr in the chamber, the difference in the mobilities of the electrons and ions resulted in a self bias of $\sim$ -400V on the bottom electrode. Due to large mean free paths of the molecules, the direction of the etching process was decided by the electric field due to this self bias. Vertical etch profiles result.

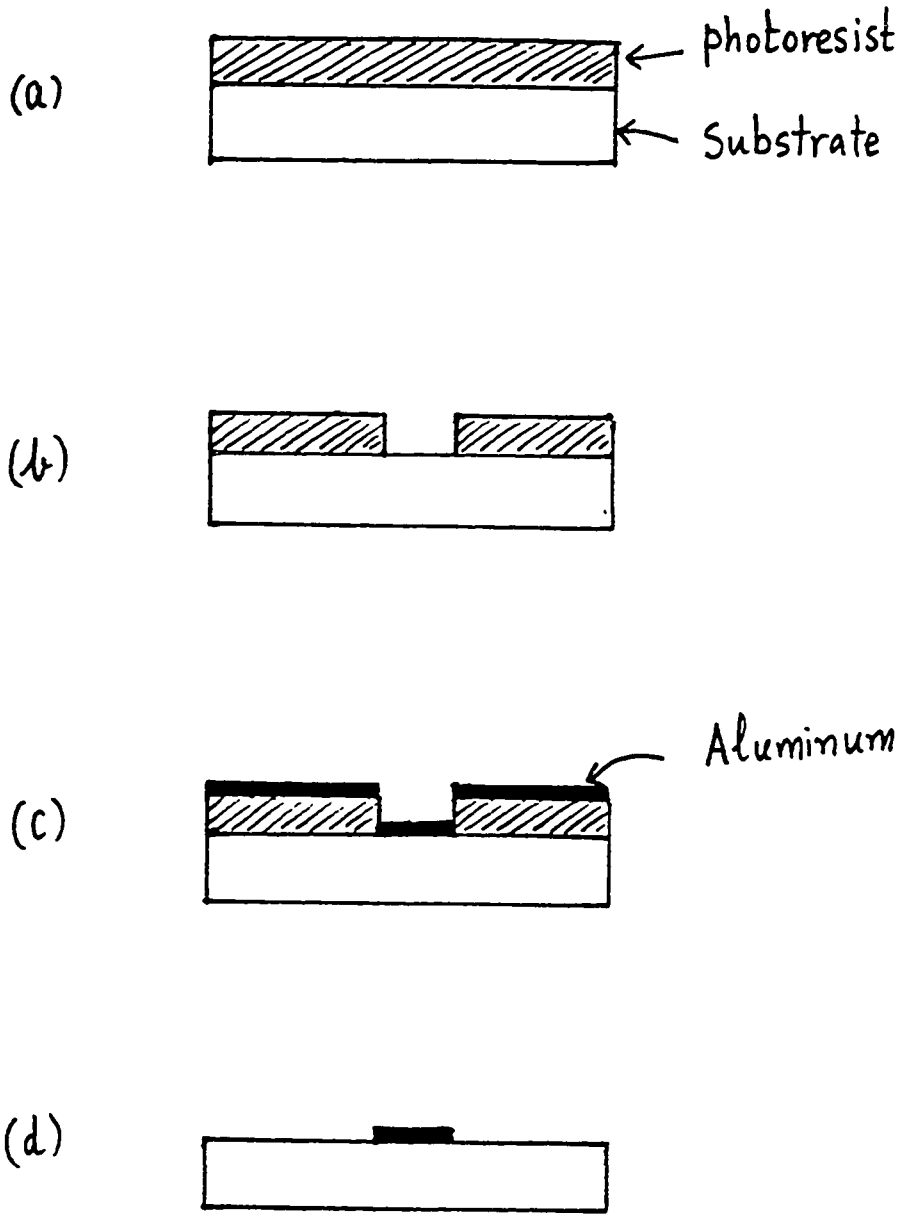

Fig.III-1 Basic fabrication sequence for optical lithography shown in side view. (a) photoresist spin-coated on the substrate (b) Exposure and development of the photoresist (c) Metal deposition (d) Metal pattern after lift-off.

For the conditions described above, an etch rate of $\sim$1000Å/minute was observed by D.Face[67] for the common organic polymers(AZ photoresist, Poly-Methyl MethAcrylate, Polyimide). We used this rate as a standard in our lithographic processes.

III-D LARGE SCALE LITHOGRAPHY

In this work, samples of width from 250 microns down to 2 microns were fabricated using the conventional contact optical lithography. A typical process sequence is shown in Fig.III-1 . This involved the following.

(i) Preparation and cleaning of cover glass substrates (not shown in the figure)

(ii) Photolithography- the substrate was coated with photoresist (PR); the areas to be metallized were exposed to light through a mask and PR in those areas was removed by developing.

(iii) Film Deposition- A thin film of aluminum was deposited onto the substrate by thermal evaporation in a vacuum chamber.

(iv) Lift-off- The PR was dissolved away in an organic solvent removing the metal which overlaid it, while the metal in direct contact with the substrate remained.

More details of the processing steps and parameters can be found in Appendix E.

The exposure of the PR was done in two ways. (1) If no reduction in size was required in the exposure stage, a mask of the same size as the final sample was needed. For doing such contact lithography, we used an exposure unit which holds the mask and the substrate in close conformal contact. The exposure unit has been described in detail in Ref.68. (2)

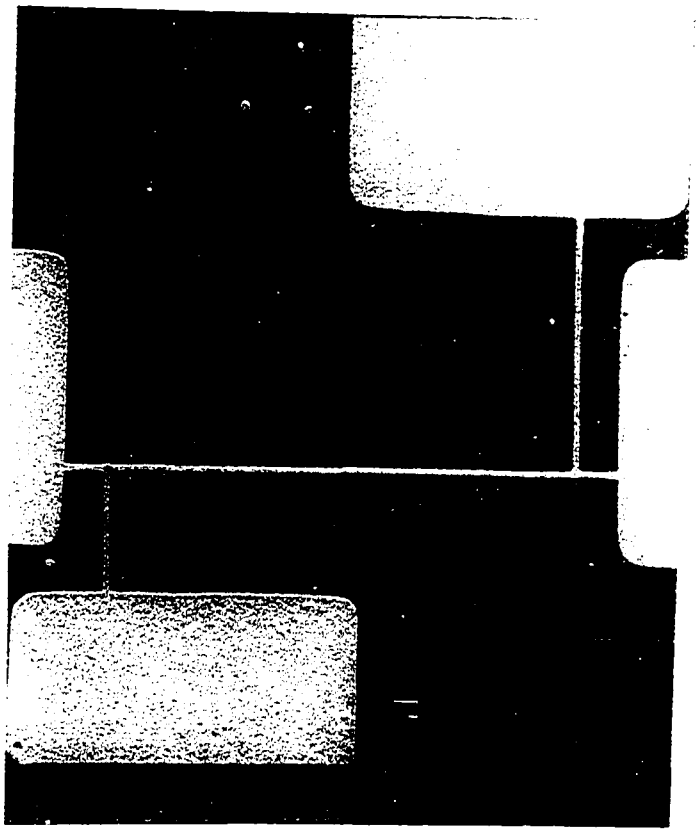

Fig.III-2 SEM photograph of a 2 micron wide aluminum line fabricated by optical lithography. The size bar is 10 microns long.

When a reduction in size was required in the exposure stage, a Zeiss Photomicroscope was used to project the demagnified image of a mask onto the substrate. The use of a microscope as a projection system for doing microlithography has been described by Feuer and Prober[69]. The demagnification factor can be changed by the choice of the objective lens in the microscope.

The design of the mask for photolithography was done to facilitate three- and four-terminal electrical measurements on the completed sample. We started from a large pattern cut in rubylith (or black masking tape on mylar) of size depending on the reduction planned. After an initial reduction of 10 to 1 with a simple Kodak camera onto a high-resolution emulsion plate, the pattern was transferred onto a cover glass slide using contact photolithography and photoresist processing. One can obtain a chrome-on-glass mask by depositing $\sim$1000Å of chrome onto the transferred photoresist stencil and doing lift-off processing. This transfer from emulsion mask to chrome-on-glass mask was desirable even in cases where no further reduction of the size was needed because of the fact that the emulsion mask got scratched easily with use. The emulsion mask also did not have sharp boundaries between dark and clear regions. When a larger reduction in size was required, further projection lithography was done in order to fabricate a mask, which could then be used for contact lithography. The highest resolution we could achieve was with a 100x oil immersion objective with a numerical aperture of 1.25. This lens demagnified the mask by a factor of 43.5, which was also the largest reduction ratio we could achieve in a single step. Once a mask was made, we successfully replicated line widths as narrow as 2 microns using a single layer contact lithography. Fig.III-2 shows a 2 micron

wide line of a 200Å thick aluminum film made by such a combination of steps.

III-E FINE LINE LITHOGRAPHY

III-E.1 Optical Projection Lithography

Fabrication of narrow wires can be accomplished by a variety of techniques. These are summarized in Ref.70. One can do optical projection lithography using high resolution objectives to make structures less than a micron, as demonstrated by Feuer and Prober[69]. Their technique of exposing through the substrate (to obtain favorable PR profiles for lift-off) yielded wires as narrow as 0.2 micron. The process requires a high quality microscope, good control of the processing parameters (exposure and development of the photoresist) and the use of the non-linear photochemical properties of the photoresist polymer.

Fig.III-3 shows the SEM pictures of chrome lines made by direct optical projection lithography made using a single layer of AZ-1350B photoresist. The width of the line on the mask before projection through the 100x lens was 12 microns. The final line width should be close to 0.25 micron, based on a demagnification factor of 43.5. By controlling the time of exposure, one could change the width of the line from 0.5 micron (corresponding to an exposure of 45 sec) down to 0.25 micron (corresponding to an exposure of 40 sec). III-3a is a 0.5 micron wide 500Å thick chrome line. III-3b is a 0.25 micron wide chrome wire of the same thickness. At lower exposures the lines developed bad lift-off profiles which resulted in the tearing of chrome film during lift-off as is obvious from Fig.III-3c.

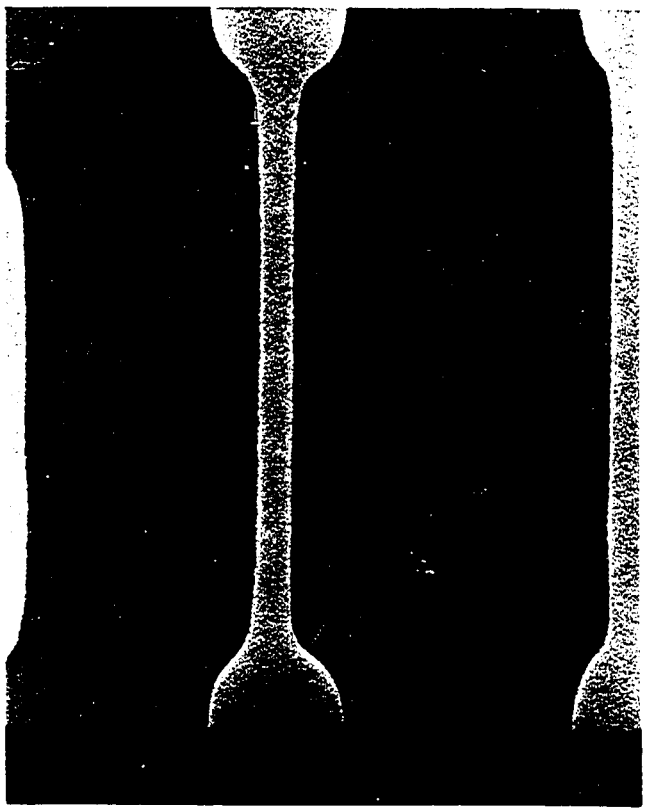

Fig.III-3(a)

Fig.III-3(b)

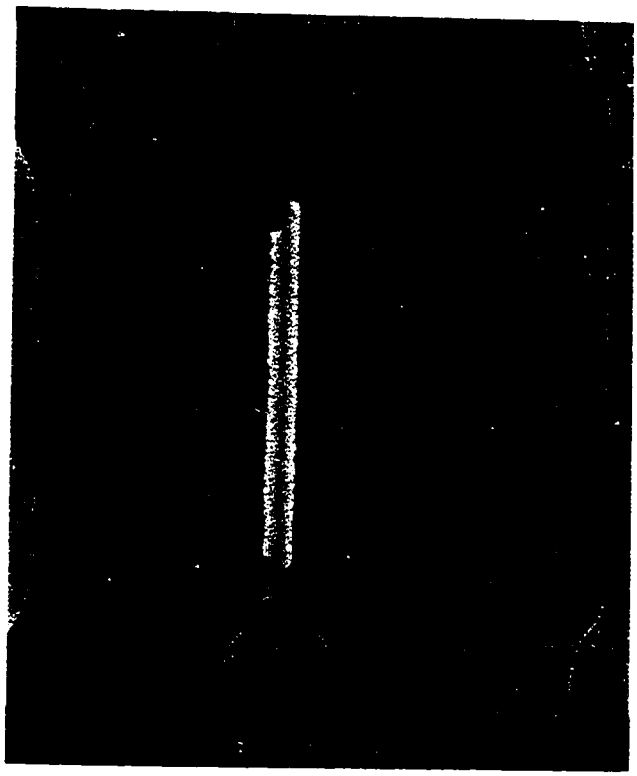

Fig.III-3(c)

Fig.III-3 SEM photographs of 500Å thick, submicron width chrome wires fabricated by optical lithography. (a) A uniform 0.5 micron wide line.(b) A 0.25 micron wide line made with the same mask by controlling the process parameters (c) An example of a badly lifted-off wire; see the tearing of the edges.

Due to intensity variations across the field of projection and the limited field of view we could not make uniform wires of widths < 0.5 micron longer than ~10 microns. These samples were fabricated using an objective that was not a flat-field objective. It appears that longer wires of ~0.5 micron width can be made with a flat-field objective[71]. For 1D localization studies in clean aluminum wires we needed to make samples of sufficient length to have high enough total resistance for observing small changes in normalized resistance. Hence other techniques were used.

III-E.2 Step-edge Lift-off

A novel method of fabricating long narrow wires was devised by Prober et al.[72] This process is shown in Fig.III-4. A vertical step was formed on the substrate and it was sputter coated with the metal of interest. By ion beam etching the metal surface at an angle, a triangular wire was formed along the step edge. This process utilized the fact that the substrate was etched by the ion beam more slowly than the metal was etched. An alternate method, to make wires of rectangular cross section, would be to evaporate the metal parallel to the surface of the substrate after the step had been formed.

We wanted to develop a fabrication process which avoided a separate lithographic step for making electrical contacts to an already fabricated wire. The problem of contact resistances (particularly in the case of quasi-four terminal electrical measurements) can be acute as a result of the the protective oxide on Al. Also, our desire to prepare a wide film in the same deposition as the narrow wire (to compare properties of 2D and 1D samples) necessitated a lift-off process in the fabrication of

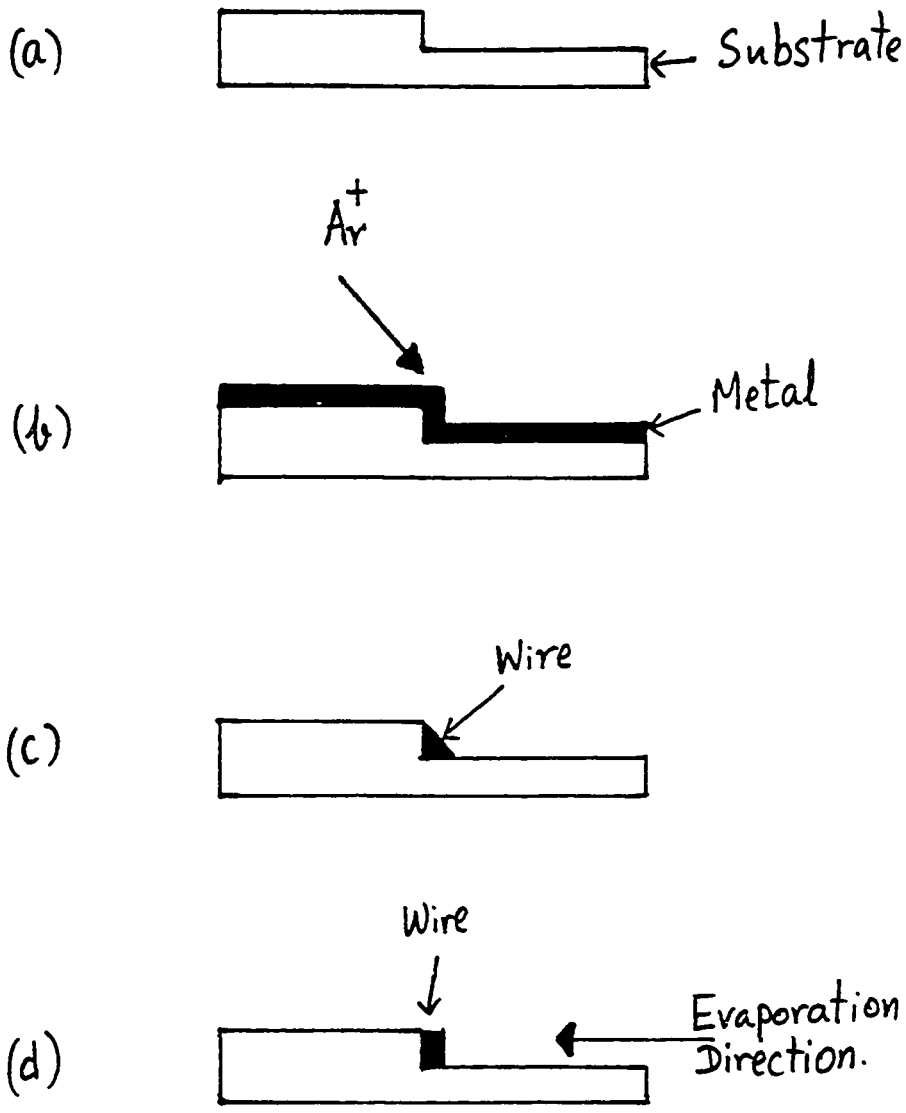

Fig.III-4 The fabrication sequence of step-edge method of Prober et al. shown in side view.(a) Formation of a step on the substrate (b) The metal is deposited and Ar^+ Ion-beam etched at an angle (c) A nearly trianglular is formed along the step edge. (d) An alternative way of obtaining a wire of rectangular cross section by evaporating the metal parallel to the substrate after the process step (a).

both the wide film and the narrow wire. The particular step-edge lithographic method discussed above did not meet these demands.

In the early stages of this work, none of the more sophisticated lithographic capabilities such as electron-beam lithography or x-ray lithography was available at Yale. We had to develop a fabrication process based on optical lithography, step-edge shadowing and Reactive Ion Etching (RIE). This was a lithographic challenge too tempting to ignore.

The process we developed is shown schematically in Fig.III-5. We started with a clean cover glass substrate.

(i) A 4% solution of Poly-Methyl MethAcrylate (PMMA) of molecular weight 950,000 in chlorobenzene[73] was spin coated at speed of 1500 RPM. The substrate was baked at 175°C for 30 minutes. We used PMMA for its chemical stability even when baked at high temperatures. The resulting PMMA layer was $\sim$3000Å thick.

(ii) After waiting for 15 minutes for the substrate to cool down, Polyimide precursor[74] (PI-2550 diluted 1:1 with T-8035 thinner and thoroughly mixed) was spun on at a speed of 8000 RPM for 2 minutes. Since the polyimide tended to bubble when it was put on the substrate, we waited for 1 minute before spinning. The substrate was baked again, but now at 250°C for 1 hour. This step yielded a $\sim$6500Å thick PI layer.

(iii) A layer of AZ-1350B photoresist was spin-coated at 6000RPM for 40 sec. The substrate was baked at 80°C for 20 minutes. The PR layer was $\sim$3000 Å thick

(iv) The photoresist was then exposed in the Zeiss microscope using half the exposure field and through-the-substrate exposure. The mask was a razor blade. This was followed by deposition of a 300Å thick chrome

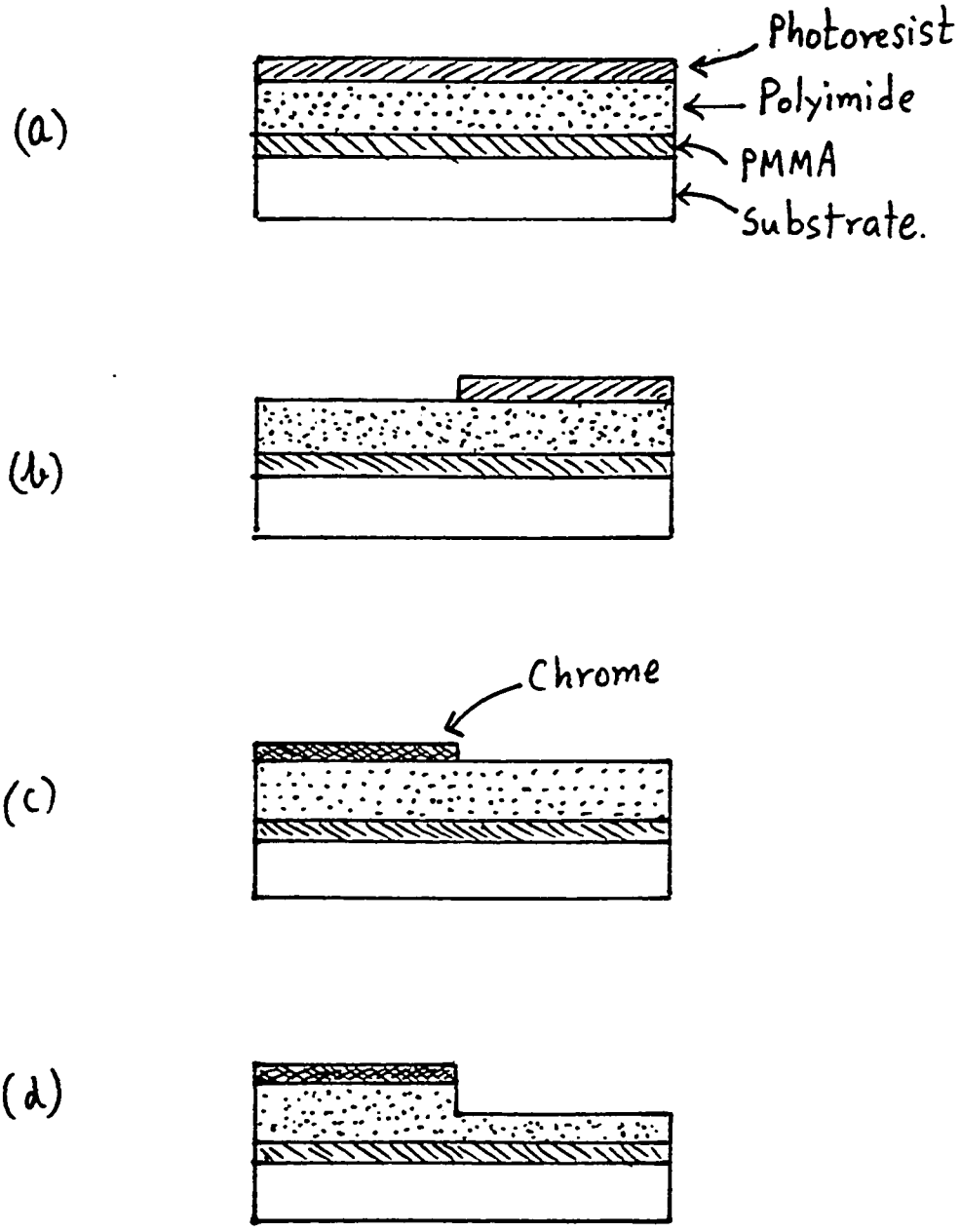

Fig.III-5 The fabrication sequence for the step-edge lift-off process developed in this work. (a) A multilayered substrate is prepared for optical lithography. (b) An edge is formed in the top layer by photoresist exposure and development. (c) A 300Å chrome film is deposited and lifted-off. (d) RIE in O_2 plasma to form a step in the polyimide of desired height

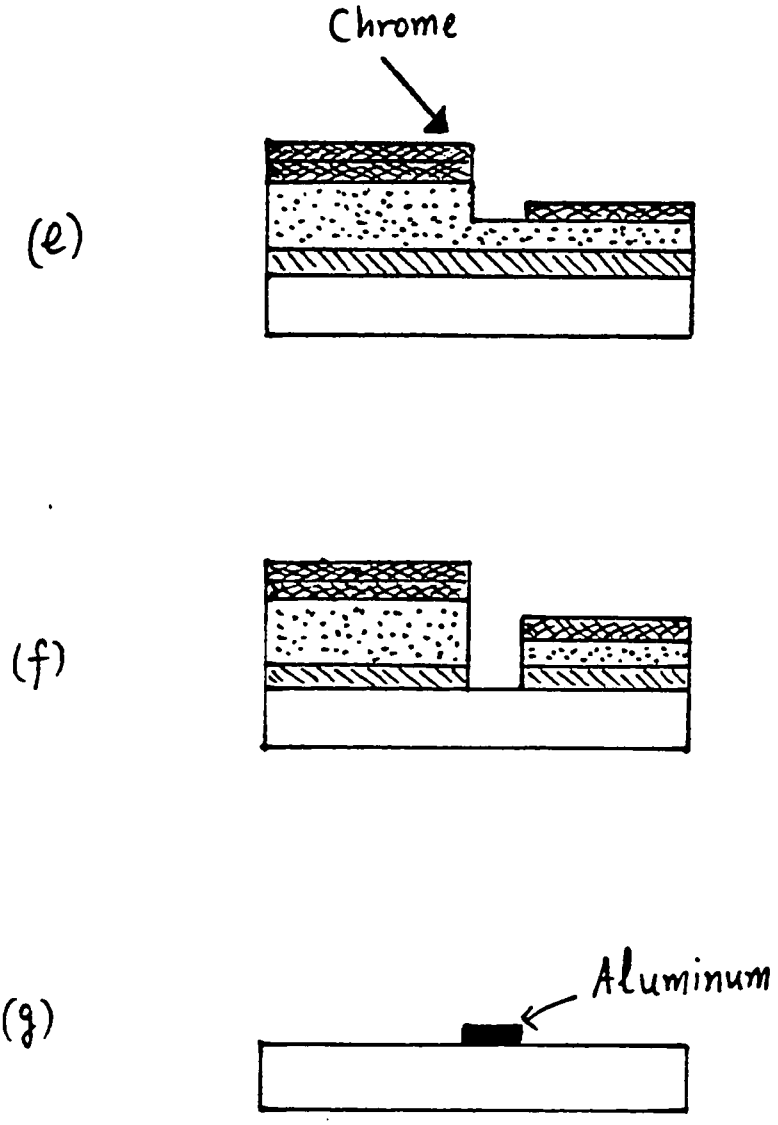

(e) A second 300Å thick chrome film is deposited at an angle defining the gap next to the step. A metal slot mask defines the contact pads during the deposition. (f) A second RIE to expose the substrate where it is not covered by chrome.(g) Deposition of Al and lift-off.

film and liftoff. The result was a semicircular chrome film with a straight, smooth edge on the PI.

(v) The substrate was then etched in an Oxygen plasma by RIE (described in III-C) to form a~1500Å step in the polyimide layer.

(vi) A second chrome film (also 300Å thick) was evaporated across the step at an angle to leave a gap at the step. The width of the gap was determined by the angle of deposition and the step height. A metal slot mask was held close to the substrate to cover the regions on either side of the step. The slot mask was oriented perpendicular to the edge. This provided clear areas for contact pads.

(vii) The substrate was again etched vertically with O_2 RIE until the glass surface was exposed. The result is a stencil with a gap corresponding to the wire and a large contact pad on either side.

(viii) The desired thickness of aluminum was then evaporated.

(ix) The sample was then soaked in acetone for two hours, sprayed gently with acetone and isopropanol and blown dry with high purity nitrogen gas.

Fig.III-6 shows the results of the process described above. For the most part the process worked close to expectations. The crucial step, which resulted in low yields, was stage (vi) above. In this angle deposition, a small piece of dirt was often trapped in the gap and this would result in a wire with a small break in it. We had numerous instances when dirt, organic or inorganic, resulted in broken wires.

Another issue which caused a serious concern at the same stage of processing was the creeping of the metal atoms under the slot mask in small islands resulting in the final metal line disconnected from the contact pads. Some remainder of this problem is seen in Fig.III-6b. This

Fig.III-6(a)

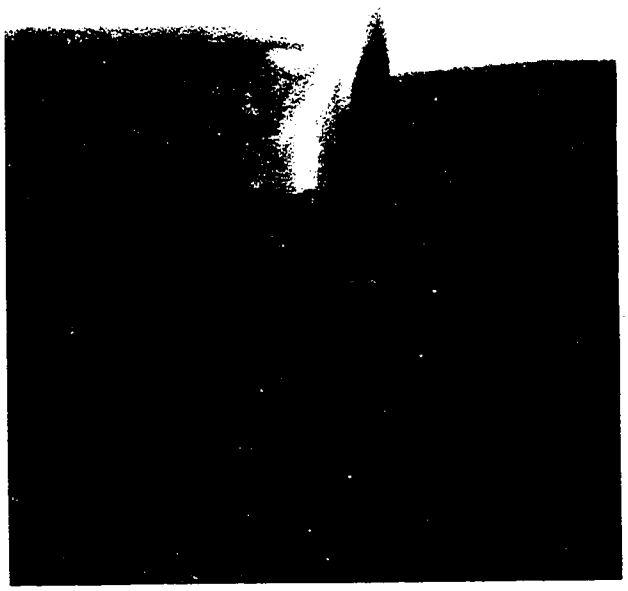

Fig.III-6 SEM pictures of the wires made by step-edge lift-off. (a) The mulilayered stencil ready for metal deposition corresponding to the process step Fig.III-5-f. The size bar is 1 micron. (b) A 800Å thick chrome wire of width -1500A. (c) the same wire under a higher magnification . The size bar is 1 micron. (d) A look at the wire edge-on along the length. The size bar is 1000Å. (e) An example of a broken wire that resulted due to trapping of dirt in the process stage corresponding to III-5-e.

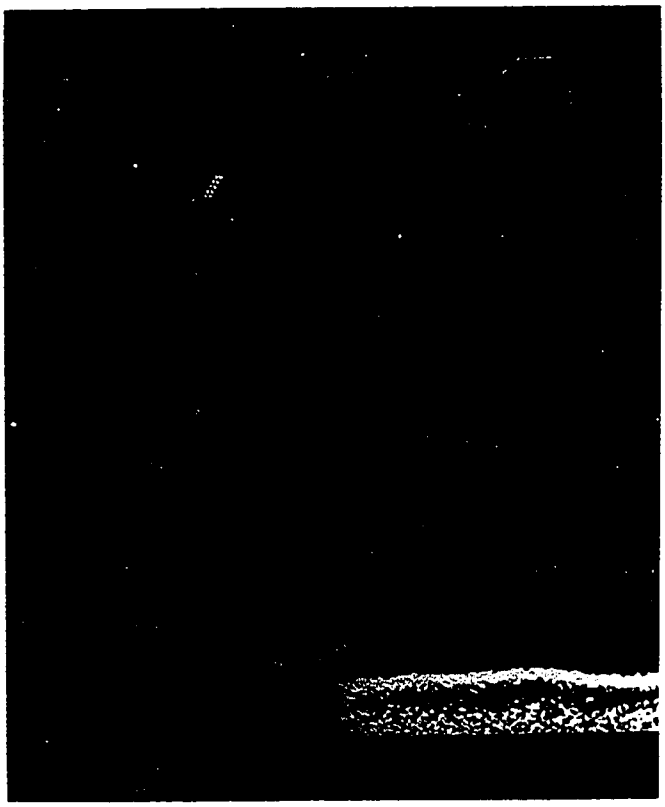

Fig.III-6(b)

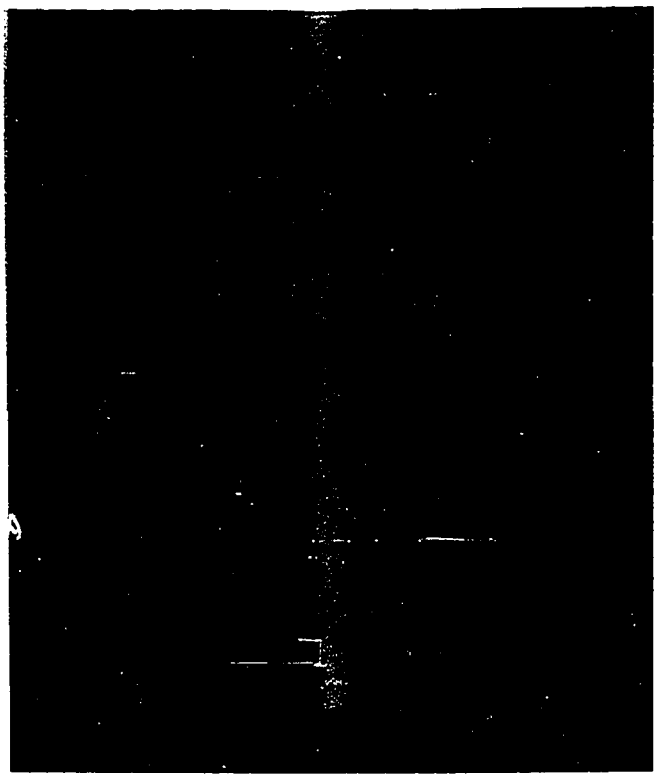

Fig.III-6(c)

Fig.III-6(d)

Fig.III-6(e)

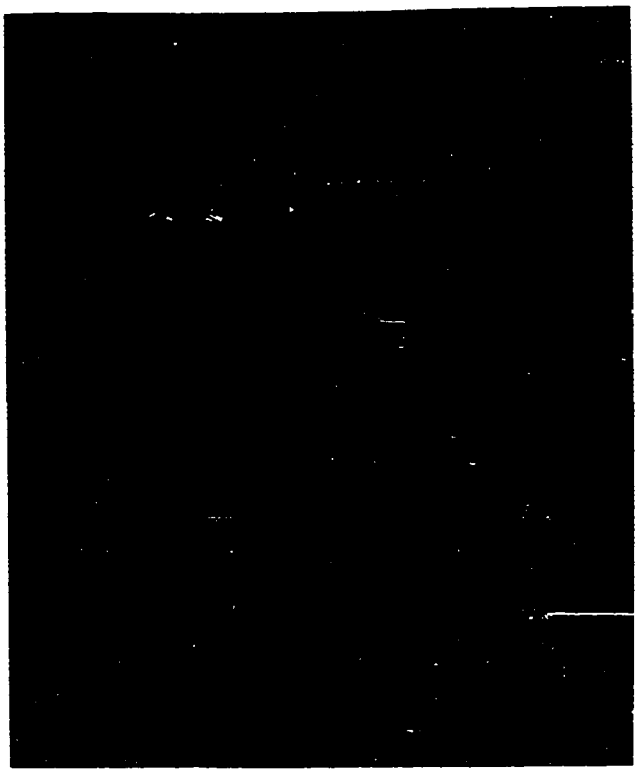

problem was subsequently overcome by a better design of the slot mask so that it was in close contact with the substrate during the chrome deposition.

At this stage of the project, an x-ray lithography station became operational in our group due to the efforts of S. Wind. Considering the almost zero yield of the step-edge lift off process, due to its high contrast nature, an alternate process using x-ray lithography was devised. However, some features of the step-edge process developed were used to make the masks required for the x-ray lithography.

III-E.3 X-RAY LITHOGRAPHY

X-ray lithography has some attractive features: (i) One can produce patterns over a large area with a resolution of $\sim$200Å. (ii) Due to favorable lift-off profiles, a single layer resist lithography can produce high yields. However, because of the limitation of 1:1 pattern transfer in contact x-ray lithography, we need to produce a mask of $\sim$0.2 micron size by some other means. The steps in the fabrication of aluminum wires using x-ray lithography are shown in Fig.III-7. The details of this process can be found in Ref.75.

The mask-making involved etching a vertical step in a micron thick polyimide film spun on a cover-glass slide, using Reactive Ion Etching. Polyimide is x-ray transparent. A $\sim$1000 Å thick gold film, the x-ray absorber, is then deposited across the step at an angle, leaving a gap at the base of the step. The initial height of the step and the angle of deposition of gold film determined the width of the gap formed and hence the width of the final line. A broad clear region for a contact pad was formed on either side of the line in the gold deposition stage by a metal mask. The polyimide membrane was then alternatively supported by a

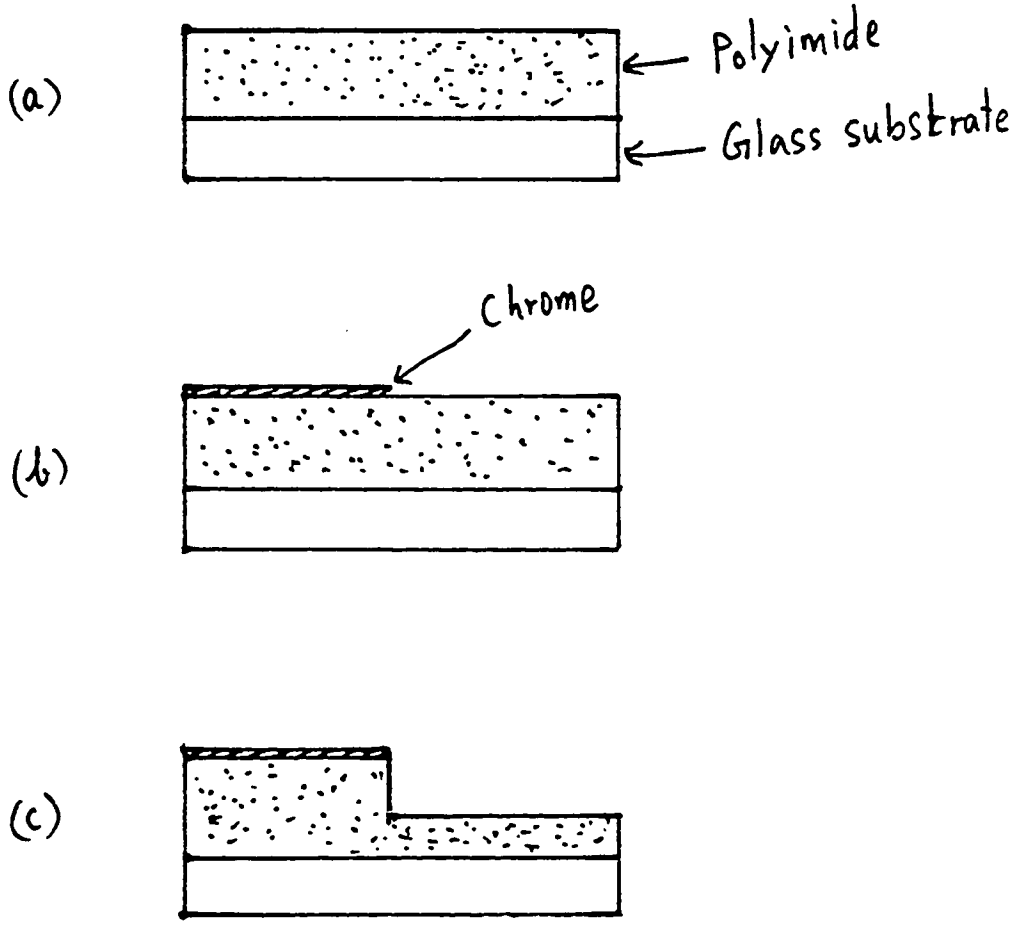

Fig.III-7 An outline of the x-ray lithography process in side view. The steps (a)-(d) are for the fabrication of the x-ray mask. (a) Preparation of polyimide coated glass substrate (b) Formation of a chrome film with smooth straight edge by optical lithography and lift-off. (c) RIE in O_2 plasma to form a step of desired height.

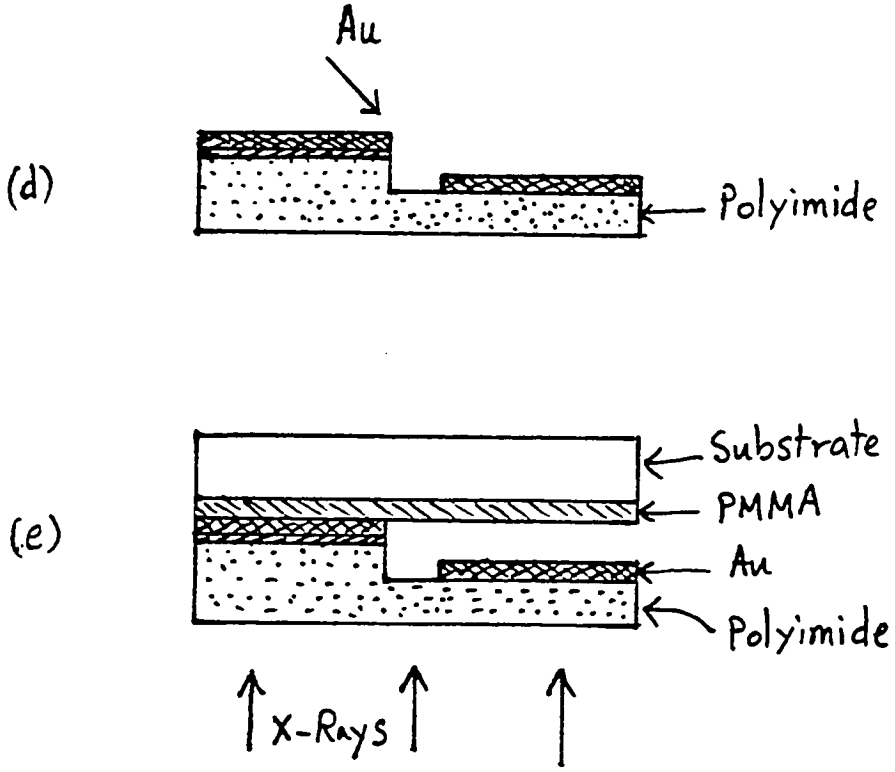

(d) Deposition of a 1000Å thick gold film at an angle to form a gap close to the edge. The contact pads are also defined in this stage by a metal slot mask. The glass substrate is removed by etching and the polyimide membrane is mounted on a vespel ring (not shown in the figure).(e) Exposure of the PMMA resist coated substrate to x-rays (f) After development, aluminum deposition and lift-off, the finished sample.

vespel ring to enable the removal of glass substrate (which otherwise would attenuate x-rays) in hydrofluoric acid.[76]

The x-ray source was a water cooled copper target. The electrons of approximately 6kV energy were focussed onto the target in a diffusion pumped chamber at $\sim 10^{-7}$ torr. The x-ray resist (PMMA) coated silicon wafers were exposed using the x-ray mask. The close contact between the mask and the substrate was ensured by an electrostatic technique[76].

III-F MEASUREMENT TECHNIQUES

III-F.1 Sample Mounting

The handling of samples after fabrication was a delicate task. While the wider films for the two dimensional studies were more forgiving, the wires of width <1 micron had to be properly handled. In all cases, we found it useful to short the leads on the substrate with silver paint before soldering external copper leads onto them. We used pure indium solder for the contacts. Indium solder stuck better to Al films when the contacts were made soon after the film deposition. After mounting the sample in the cryostat, an external shorting plug was used to keep the leads of the sample shorted, at which time the silver paint connections on the substrate were scratched out. In addition, extra precautions were taken to avoid electrostatic build up problems[68]. A few samples were 'blown out' when such a procedure was not followed.

III-F.2 Resistance Measurement

In our experiments we had the provision for making

(1) four terminal measurement using a dc current source and a Keithley nanovoltmeter[77a]

(2) four-terminal ac measurement using a PAR-126 lock-in

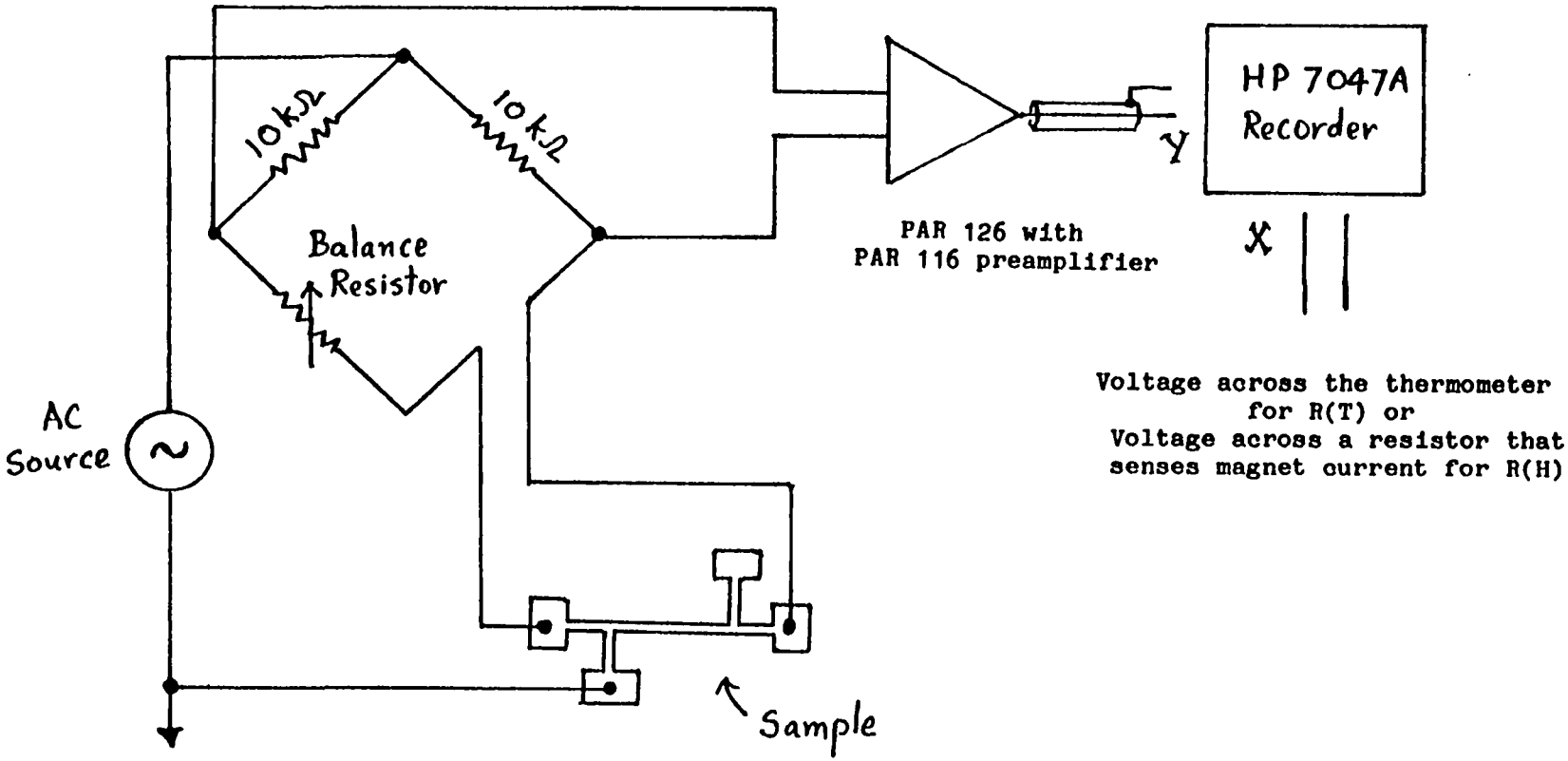

Fig.III-8 A schematic of the three-terminal measurement apparatus.

amplifier[77b] and

(3) three-terminal measurement using a LR-110 ac bridge[78]

While the four terminal measurements were distinctly better in avoiding complications due to contact and lead resistances, they did not have the needed accuracy because of drift problems of the ac current source and off-set and dynamic range limitations of the dc amplifier. Thus three-terminal ac measurements were used for the high resolution MR studies.

For the low resistance 2D samples (R < 200 ohms), we found the combination of the three-terminal bridge and a lock-in amplifier detector (with a transformer input) to be the most effective configuration. The schematic of the measurement set up using the three-terminal bridge is shown in Fig.III-8. A typical situation in the measurement of 2D films was a signal voltage of 10 mV (peak-to-peak) and noise of 10 nV (peak-to-peak) (with the transformer) so that a resolution of $\sim 1 \times 10^{-6}$ results from this simple consideration. We could obtain a resolution and short-term stability of better than one part in 10^6 , as required for making magnetoresistance studies on low resistance samples up to relatively high temperatures. The noise observed was essentially determined by the Johnson noise of the room-temperature balance resistor of the bridge. The symmetric design of the leads in the mask for the two dimensional samples (see Fig.III-8) made it possible to obtain a value for sample resistance measured with the three-terminal bridge which agreed with the resistance measured in the four terminal measurements to better than 5%. However, for the high resistance narrow wires the LR-110 bridge with its own internal detector was adequate. The contact resistances (~1ohm) were negligible compared to the wire restance(~ 1kohm). In all cases,

for both 1-D and 2-D samples, care was taken to avoid complications due to superconductivity of indium contacts below $T_c \sim 3.5$ K. If the three-terminal bridge was used below the $T \sim 3.5$K there were obvious abrupt changes in the magnetoresistance that were reproducible. The maximum field below which the magnetoresistance was not affected by the indium contacts increased with decreasing temperature. We could verify the magnetoresistance behavior below this maximum field by using the four-terminal measurement below $T \sim 3.5$K. Since the signal was larger at low temperatures we did not need the highest resolution to make this check. A frequency of 500 Hz was used for all ac measurements.

III-F.3 Self-heating

In addition to the issues discussed in the last paragraph, an important limit to the ultimate resolution possible in our experiments was an upper limit to the measuring current as a result of self-heating. For the narrow wires which had a typical low temperature resistance of ~ 1 kohm, measuring currents larger than ~ 20 microamperes produced heating effects. This can easily be checked experimentally at any given temperature as follows. First the magnetoresistance was plotted on the chart paper at a given measuring current. Then the measuring current was changed to a convenient multiple of the previous current and the voltage scale of the chart recorder was changed by the same multiple. The magnetoresistance was plotted again. If there was no self-heating, the second curve would trace right on top of the first trace. But if there was heating, the magnetoresistance would behave as if the sample was at a higher temperature. The cleanest sample we measured was a 250 micron wide film (sample Q8). This had a low temperature resistance of ~ 20 ohms and we could pass hundreds of microamperes through it without any

appreciable self-heating. In all cases we had to use smaller currents at lower temperatures to avoid heating problems.

III-G LOW TEMPERATURE APPARATUS

This section describes briefly some salient features of the cryogenic arrangement. The set-up was the one used by B.J.Dalrymple. The reader is referred to his thesis[79] for an excellent account of the details. The lowest temperatures ($\sim$ 1.25 K) were reached by pumping on the liquid He^4 bath.

The cold end of the cryostat consisted of a variable-temperature copper bar located inside a vacuum can made of copper. The bar housed a thermometer, a resistance heater (a 1 kohm metal film resistor) and a stub for holding samples. Different mounting stubs were used for parallel and perpendicular field measurements. The copper bar was connected through a weak thermal link (a brass screw-nylon spacer arrangemant) to the top copper plug which sat at the Helium bath temperature. Numerous #40 copper wires passed from the top of the cryostat at room temperature down to the variable temperature copper bar at the bottom to meet the various needs.

Temperature measurement was done using a calibrated, germanium resistance thermometer Cryocal[80] Model CR-1000. For temperatures above 4.5K the sample was in a vacuum can; for temperatures below 4.5K a small amount of He transfer gas was introduced. Temperature stability was good to a millikelvin at low temperatures without any feed-back circuits. Sweeping the temperature was accomplished by the heater imbedded in the same copper block of the cryostat which holds the sample and the thermometer.

Magnetic fields required in the experiment were produced by a NbTi superconducting magnet. The field calibration was 2.53 kG/Amp. For fields H < 2 kG, a HP 6214A power supply (I_{max} =1.2 Amp, V_{max}= 12V) was used. When larger fields were needed, a larger Hewlett Packard 6259B (I_{max} =50 Amps., V_{max}=10V) supply was used. The current through the magnet was monitored by measuring the voltage across a standard resistor in series with the magnet. We swept magnetic field continuously to record the MR on a HP 7047A x-y chart recorder. Due to the clean nature of our samples, we did not need fields larger than $\sim$2kG to observe the localization effects. Both positive and negative field values were recorded to locate the zero of the field. Field offsets due to trapped flux of $\sim$1G were typical.

IV. EXPERIMENTAL RESULTS: THIN FILMS

IV-A FILMS AND MATERIAL PARAMETERS

In this chapter, we discuss the detailed analysis of the experimental data on thin films obtained using the techniques described in Chapter III. In a typical experiment, we needed to determine some fundamental parameters for a proper characterization of each sample. These parameters are:

(i) Film Thickness (d): The thickness of the film is known (to ~5% accuracy) from the readings of the thickness monitor during the deposition.

(ii) Sheet resistance or Resistance per square ($R_\square$) of the film: From an electrical measurement of the resistance of the film and knowledge of its geometry, we determine the $R_\square$ of the film, using

$$R_\square = R\ (W/L)$$

where R is the total resistance of a sample of width W, and length L. $R_\square$ measured at T= 4.5K was used extensively in the theoretical equations of Chapter II.

(iii) Resistivity (ρ) : The resistivity at any temperature can be determined from $R_\square$ using the relation

$$\rho = R_\square \times d$$

The resistivity ρ_o at T= 4.5K gives an estimate of the concentration of impurities and other static defects in the sample.

(iv) Mean free path (ℓ) of the electrons: This is the average distance travelled by an electron between two consecutive collisions with the static (temperature independent) defects. As one could expect,

TABLE IV-1 - Parameters for 2D-films. $R_{\square}$ is at 4.5K

Sample	$R_{\square}$ (ohms)	d (Å)	T_c (K)	ℓ (Å)	D (cm^2/s)	Γ
Q8	0.17	780	1.27	258	112.0	3.05
P12	0.85	250	1.34	107	46.1	2.17
Q28	1.39	250	1.37	105	45.4	2.03
P14	1.83	250	1.42	67	29.0	1.58
P15	1.86	250	1.44	62	26.8	1.59
T46	1.87	150	1.40	80	34.6	2.00
L45	2.38	150	1.41	92	40.1	1.83
T42	3.95	150	1.46	59	25.6	1.48
Q20	5.65	150	1.51	60	26.0	1.46
BR-A[a]	8.15	95	1.82	52[c]	22.0	1.47
BR-B[b]	33.0	90	1.83	23[c]	10.0	1.18

a Sample A of Ref.89 analysed by us.

b Also of the authors of Ref.89, magnetoresistance data obtained through private communication and analysed by us.

c Estimated using Fig.IV-2.

ℓ increases as ρ_o decreases. We determine ℓ from the measurement of the critical field slope (see Sec.IV-A.1).

(v) Residual Resistivity Ratio (Γ): It is the ratio of resistivity at room temperature to ρ_o . Larger values of Γ indicate cleaner films.

(vi) Superconducting transition temperature (T_c): We have chosen the T_c of the sample as the temperature corresponding to half the resistance of the normal state in the resistive transition. The width of the transition ΔT_c increased with ρ_o; typically ΔT_c was $\sim$10 mK for $\rho_o \sim$ 3 microohm-cm. The sample parameters for the films are shown in Table IV-1.

IV-A.1 Determining the Diffusion Constant (D)

The diffusion constants for our samples are obtained by studying the superconducting perpendicular critical field slope, dH_{c2}/dT, close to T_c. We use

$$D = -\frac{4 k_B c}{\pi e (dH_{c2\perp}/dT)} = -\frac{1.098 \times 10^4}{(dH_{c2\perp}/dT)} \quad (4.1)$$

A discussion of the relevant theory can be found in Appendix F. The key advantage to obtaining the diffusion constant in this way is that we get the product $v_F \ell$ directly without having to assume either v_F or ℓ independently. In Eq.(4.1), $D = v_F \ell/3$ for three dimensional diffusion. If we use $v_F = 1.3 \times 10^8$cm/sec for aluminum[81], we verify that $d > \ell$ so that we are self-consistently in the three dimensional limit of electron diffusion.

IV-A.2 Dependence of T_c and the $\rho_o \ell$ product on ρ_o

In our samples of Al, T_c increases with an increase in the low

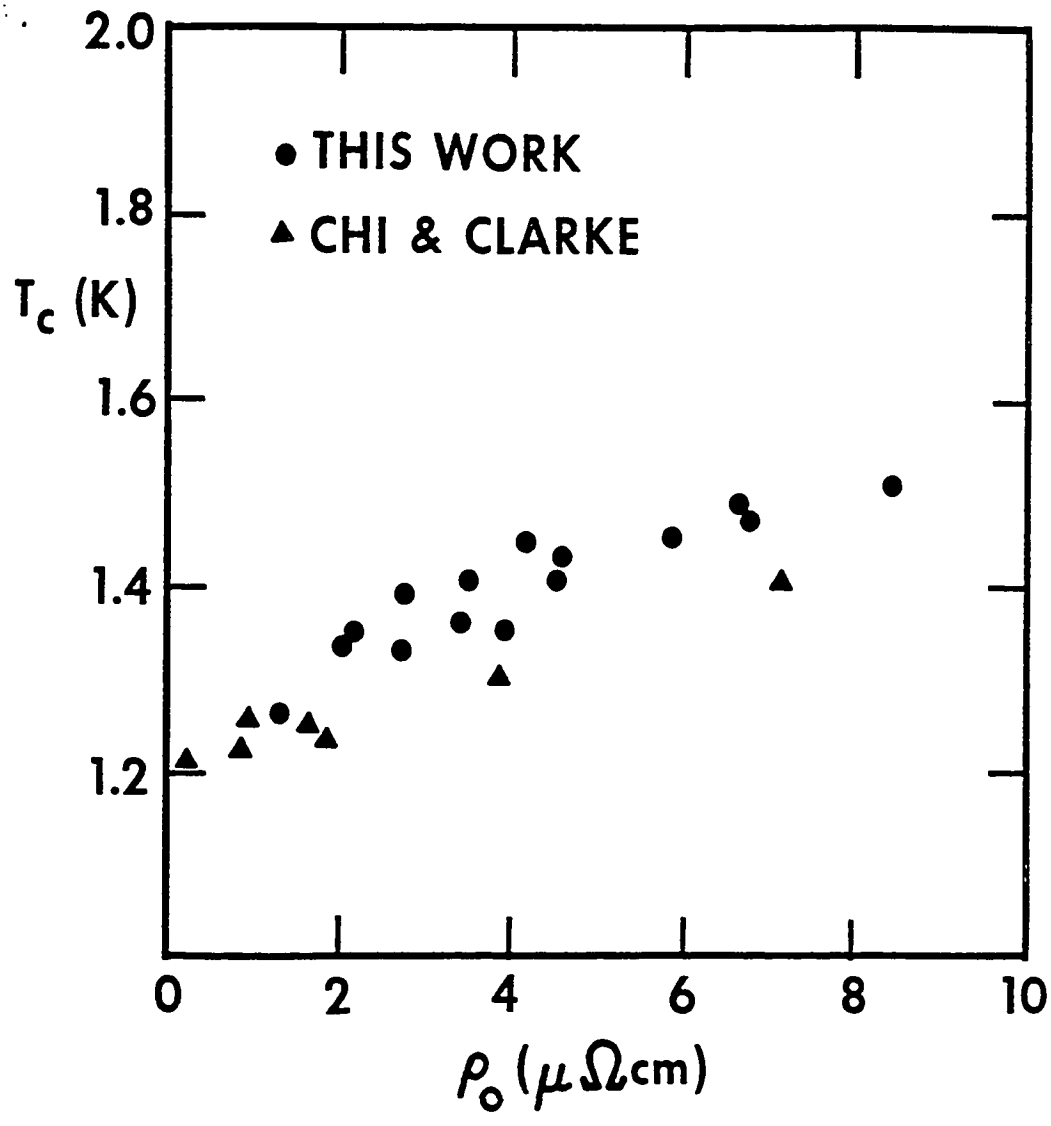

Fig.IV-1 T_c as a function of the resistivity ρ_o for our samples. The properties of the samples from Ref.60 are shown for comparison.

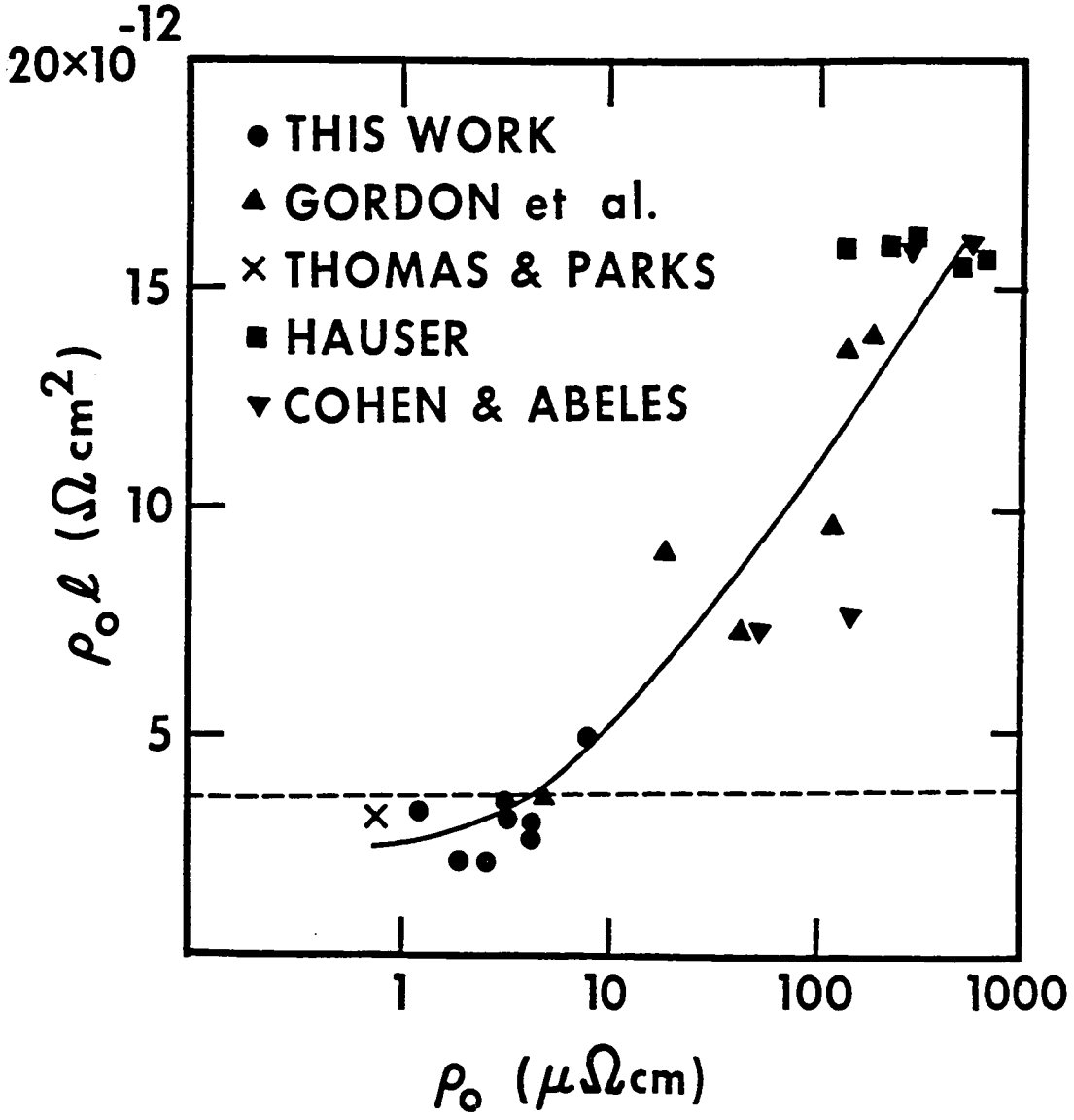

Fig.IV-2 The variation of the product $\rho_0 \ell$ for our samples along with those of Refs. 82-86. All these samples films were deposited on room temperature substrates. The dashed line shows the result from the free electron model corresponding to 3.6×10^{-12} ohm-cm^2. Solid line is a guide to the eye.

temperature resistivity ρ_c . Fig. IV-1 shows the dependence of the T_c on ρ_o for various samples. We have included the data from Ref.60 for comparison. This dependence, though widely observed in experiments, is not explained to date.

Using the Drude formula for conductivity in the free electron model, one can obtain the equation for the product $\rho_o l$ as

$$\rho_o l = \frac{m^* v_F}{n e^2} \qquad (4.2)$$

If we take $m^* = 1.4\ m_o$[31], $n = 1.8 \times 10^{23}$ /cm^3 (see Ref.12) we obtain a value of $\rho_o l = 3.6 \times 10^{-12}$ ohm-cm^2. The value of this product does not depend on ρ_o within the free electron model. The inferred values of $\rho_o l$ derived from our critical field measurements (with $v_F = 1.3 \times 10^8$cm/sec) indicate a tendency of $\rho_o l$ to increase with increasing ρ_o . We show this behavior in Fig.IV-2 along with the results from Ref. 82-86. Use of the free electron value for $\rho_o l$ is adequate only for the cleaner films to within a factor of two. The dirtier films have considerably higher values[86] for $\rho_o l$. An explanation of this behavior is not available at present.

IV-A.3 Limits on The Validity of Matthiessen's Rule

According to Matthiessen's rule[12], the total resistivity of the sample is the sum of the contributions due to (temperature-independent) static defects and (temperature-dependent) mechanisms such as phonons so that,

$$\rho = \rho_o + \rho_{ph}(T) \qquad (4.3)$$

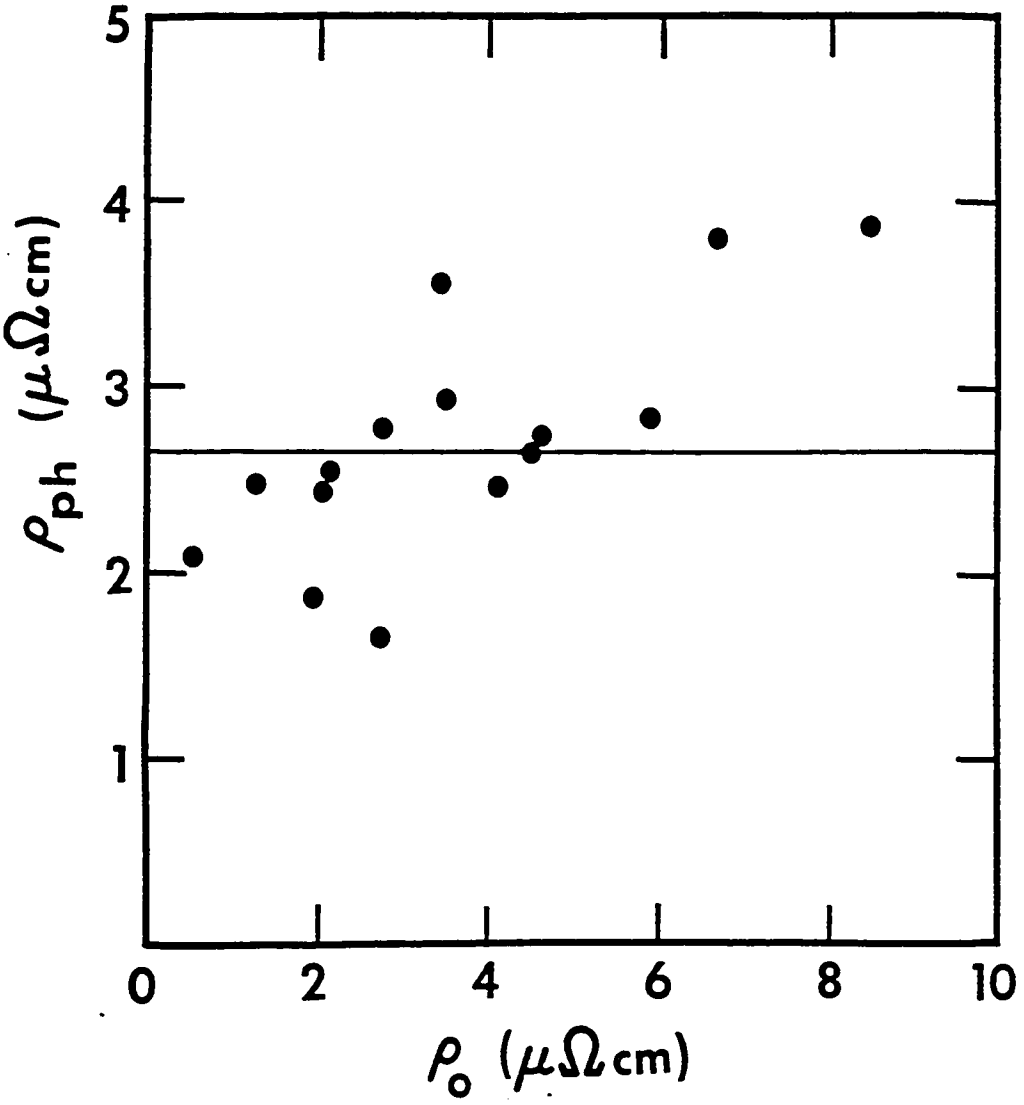

Fig.IV-3 The phonon contribution to room temperature resistivity plotted as a function of the resistivity ρ_o at low temperatures for our samples. The solid line corresponds to the phonon resistivity expected from measurements in single crystals.

where we have attributed the part of the resistivity that is temperature dependent between 4.5K and 300K to phonon scattering. In this equation $\rho_{ph}(T)$ is expected to be independent of ρ_o. Deviations from Matthiessen's rule are expected from theory[12] and have been observed in many instances[26,87].

In Fig. IV-3, we show the measured change of resistivity from Room Temperature (RT) down to 4.5K as a function of ρ_o. We note

$$\rho_{ph} = [\rho_{RT} - \rho_o] = \rho_o [\Gamma - 1] \qquad (4.4)$$

The bulk resistivity at Room Temperature of clean single crystal aluminum[88] can be assumed to be due to phonons. This resistivity is 2.65 microohm-cm. As seen in Fig.IV-3, the agreement with Matthiessen's rule is satisfactory in our experiments.

IV-B PERPENDICULAR MAGNETORESISTANCE (HIGH FIELDS)

First, we briefly mention the observed behavior in high magnetic fields ($H > 2$ kG). The experimental magnetoresistance in this regime is dominated by a behavior that depended on the square of the field and is essentially independent of temperature.

The electron-electron interaction theory (discussed in Sec.II-E.4) predicts a magnetoresistance proportional to the square of the magnetic field, but this magnetoresistance contribution is expected to be strongly temperature dependent. In addition, the estimates of this term gave values for magnetoresistance much smaller than the experimentally observed values. Thus we conclude that the behavior in these high fields is mostly due to classical magnetoresistance (see Sec.II-E.3). The

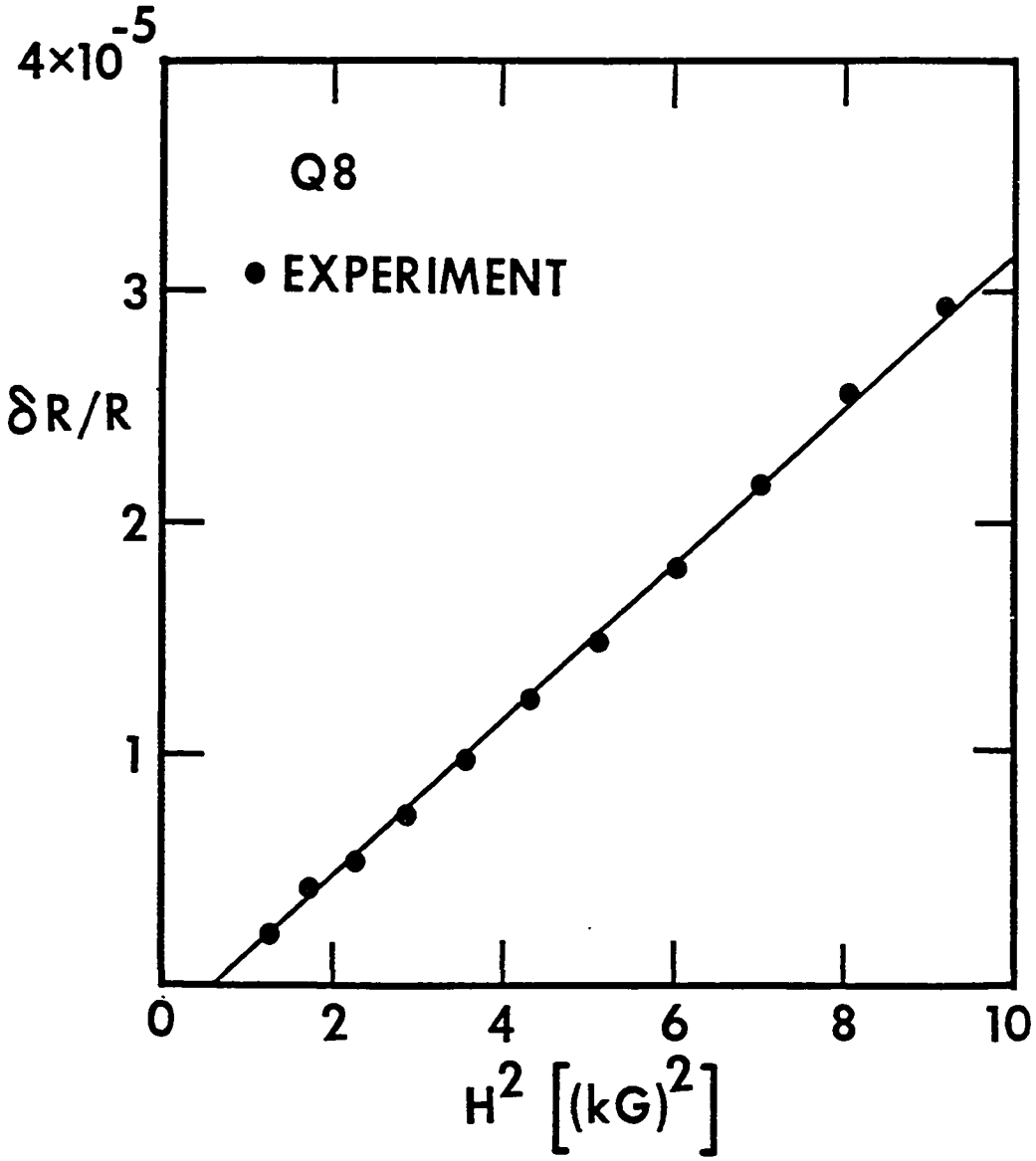

Fig.IV-4 The normalized magnetoresistance for sample Q8 at high fields plotted vs. H^2. The solid line is the fit to a straight line. The plot does not pass through the origin because of the quantum corrections to magnetoresistance at low fields.

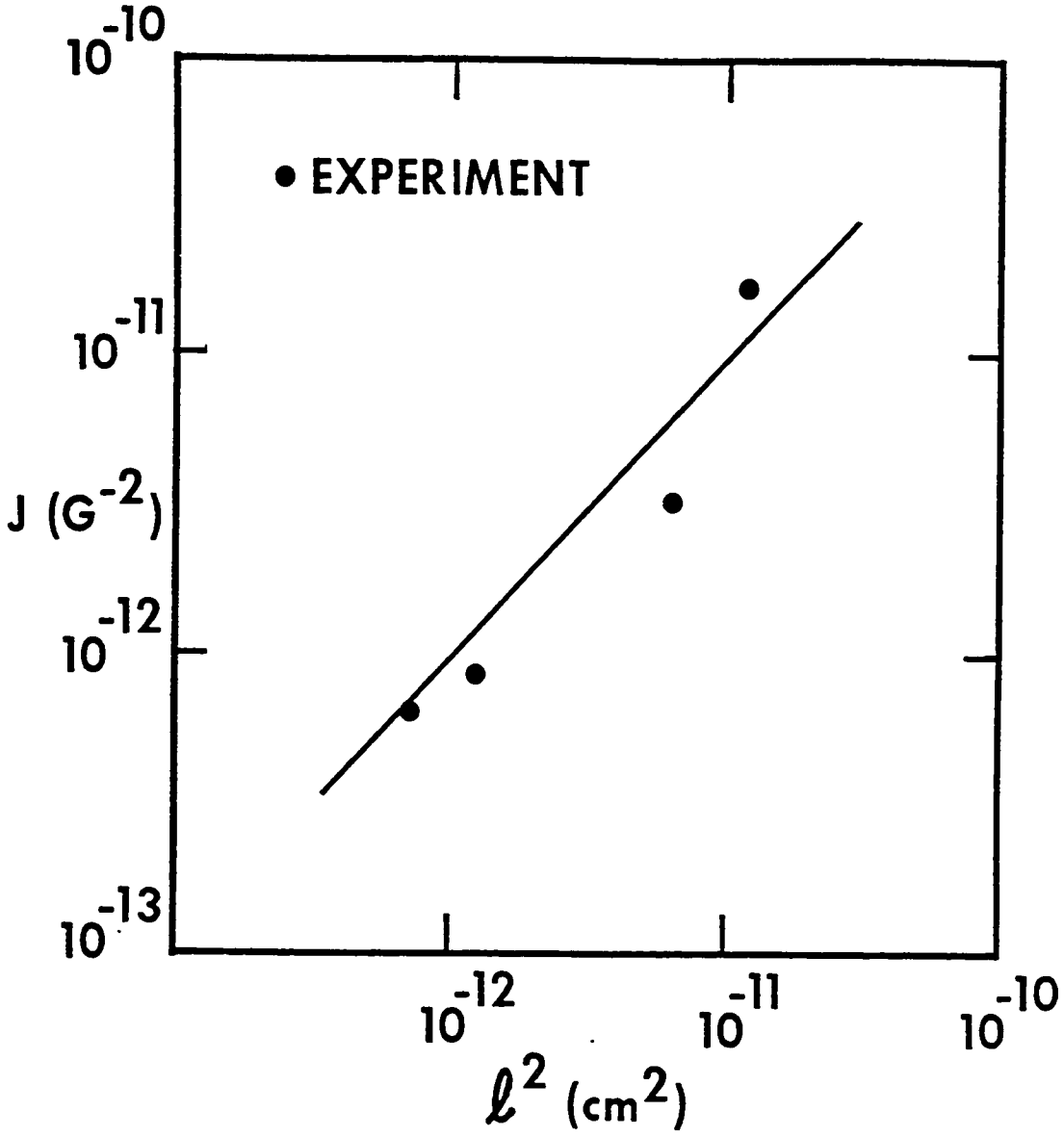

Fig.IV-5 The slopes of straight lines (similar to Fig.IV-4) for four samples plotted as a function of the square of the elastic mean free paths of the samples. The straight line corresponds to a value for K = 0.9 for H in G and ℓ in cm.

classical magnetoresistance is of significant magnitude because of the relatively long elastic mean free path of the electrons in our samples.

To support this conclusion, in Fig.IV-4 we show a plot of the normalized magnetoresistance as a function of H^2 for sample Q8. As indicated in Eq.(2.20), the slope J of such a plot should depend on the square of the elastic mean free path, so that

$$\frac{\delta R}{R}^{cl} = J H^2 \; ; \; J = K \ell^2 \qquad (4.5)$$

The elastic mean free paths were determined from critical field measurements as described in Sec.IV-A.1. Fig.IV-5 shows a plot of J as a function of the square of the mean free path for four samples. The average experimentally measured value of the constant K in Eq.(4.5) was 0.9 (ℓ given in cm and H in Gauss). Such a term for the classical magnetoresistance also quantitatively explains the presence of positive magnetoresistance in the case of sample A of Bruynseraede et al.[89] at fields larger than 1 Tesla.

We note that $K \sim 0.23$ is predicted by the two band model (see Appendix D), about a factor of 4 smaller than the experimental result. Most of the previous experimental results pertain to single crystal Al in the $H\ell \gg 1$ limit and hence are not of direct relevance to us. In addition, single crystals show anisotropy in magnetoresistance[88]. However, from Kohler plots for samples of Al with $\Gamma < 1000$, Corruccini[88] obtains a mathematical expression for the classical magnetoresistance in Al. For our samples, his expression predicts $K \sim 3$, of the same order of magnitude as our experimental result.

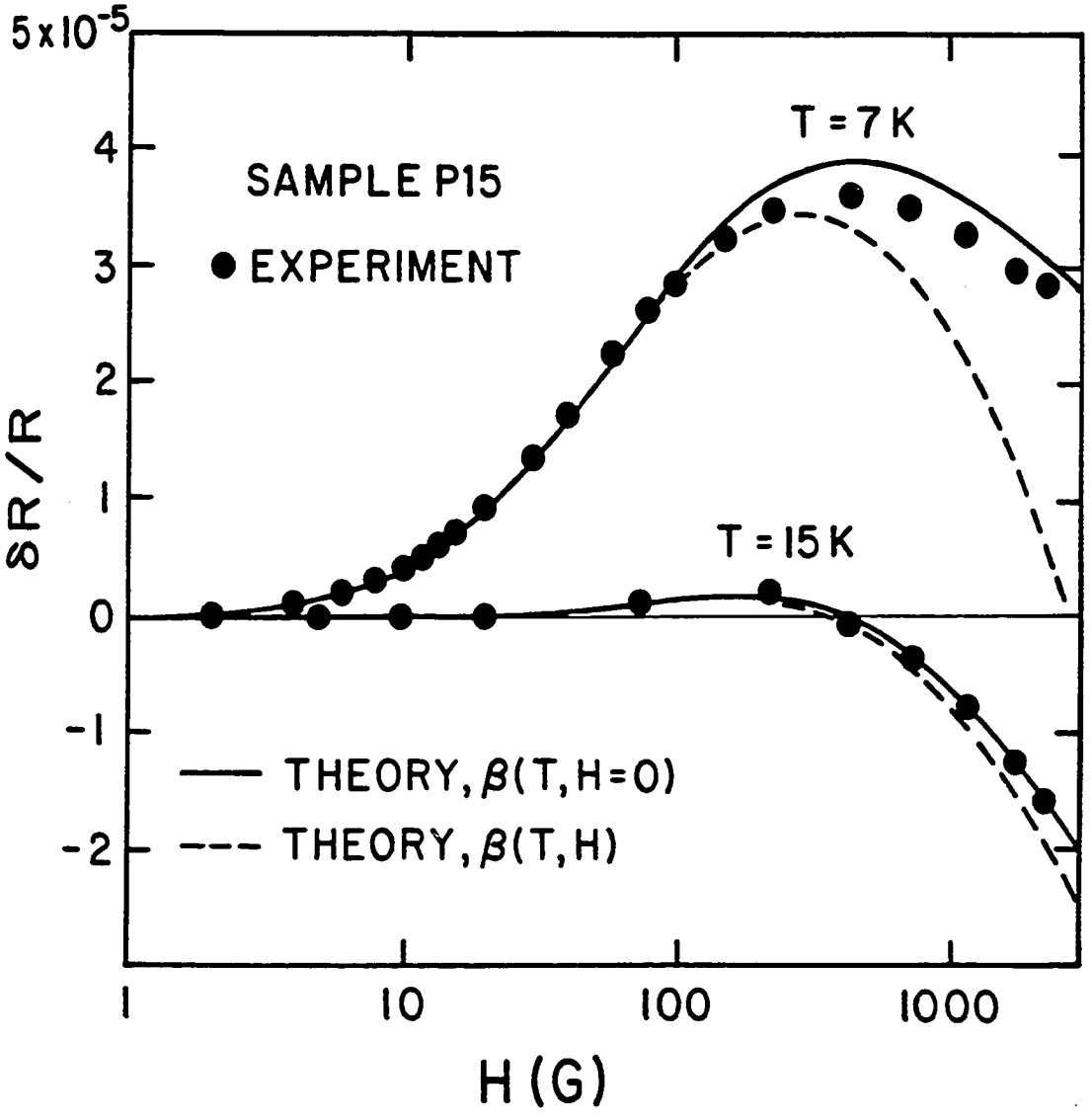

Fig.IV-6 Normalized magnetoresistance for sample P15. Fitting parameters are H_{so} = 30G and H_i=3.8 G at 7K and 33G at 15K.

IV-C PERPENDICULAR MAGNETORESISTANCE (LOW FIELDS)

IV-C.1 Fitting Procedure

We illustrate the behavior of a thin film in perpendicular fields in terms of sample P15 . Fig.IV-6 shows the normalized magnetoresistance for P15. For T $\leq$12K, the magnetoresistance was positive at low fields (H<100G), reached a maximum value and changed to negative magnetoresistance at higher fields. For T > 15K the magnetoresistance was negative in the entire field range studied (H< 2 kG).

For fields H < 500G, we could ignore the contribution from classical magnetoresistance and use only the theory of localization and superconducting fluctuations in the fitting procedure. The sum of the theoretical predictions[Eq.(2.9), (2.11),and (2.16)], is shown by the solid line. Fitting to the data was done by selecting H_{so} and H_i. $\beta(T/T_c)$ was taken from the table by Larkin[23](see Appendix G). Other workers (see for example, Ref.82) used $\beta(T/T_c)$ as a fitting parameter and found excellent quantitative agreement with the prediction of Larkin. At larger fields, Larkin's low-field prediction for $\beta(T/T_c)$ is not appropriate (see Sec.II-D.2). Fig.IV-6 also shows the result of inclusion of the depression of $\beta(T,H)$ at larger fields, as proposed in the theory of McLean and Tsuzuki[90]. This theory apparently overestimates the depression of $\beta(T,H)$ by a large amount and hence is not satisfactory. Lopes dos Santos and Abrahams[24] have recently pointed out (see Sec.II-D.2) that the theory of Larkin is valid for applied magnetic fields

$$H < \frac{c\, k_B T}{4eD} \ln(T/T_c)$$

The fits to our experimental data are done at low enough fields to satis-

fy this condition. Thus the fitting parameters could be reliably extracted from these fits.

An attempt was made to use a least square fit program with two parameters (H_i and H_{so}) and the convergence was not satisfactory. Instead, the parameters for the fitting iteration are chosen manually based on the computer plotting of the experimental data and the calculated theory curves. At temperatures $T < 12$ K the shape of the curve at very low fields ($H < 100G$) is determined almost fully by the choice of H_i and we can infer H_i values from the low field fit with an accuracy of $\pm 10\%$. The choice of H_{so} affected the maximum value of the positive magnetoresistance seen (for $T < 12K$) without much influencing the low field fit. Thus, after two or three iterations we could find reasonable fitting parameters. For $T \gtrsim 15K$ the fitting had to be done by changing both H_i and H_{so}. This took more than a couple of iterations. While this was a less than efficient way to use the computer, it took at most two days to manually fit the magnetoresistance data for a given sample for ten different temperatures. The personal reward, of course, was that one got a good understanding of how different parameters affected these fits. When treated as a free parameter, H_{so} was found to be essentially temperature independent above $T \sim 6K$. We can thus infer a value of H_{so} for a given sample, with an accuracy of $\pm 15\%$. We determine the values of τ_i and τ_{so} using Eq.(2.11a) and the value of the diffusion constant obtained as described in Sec.IV-A.1.

IV-C.2 Inelastic Scattering Rate

We show the experimentally determined inelastic rates in Fig IV-7. The solid lines are fits to the form

$$\tau_i^{-1} = A_1 T + A_3 T^3. \qquad (4.6)$$

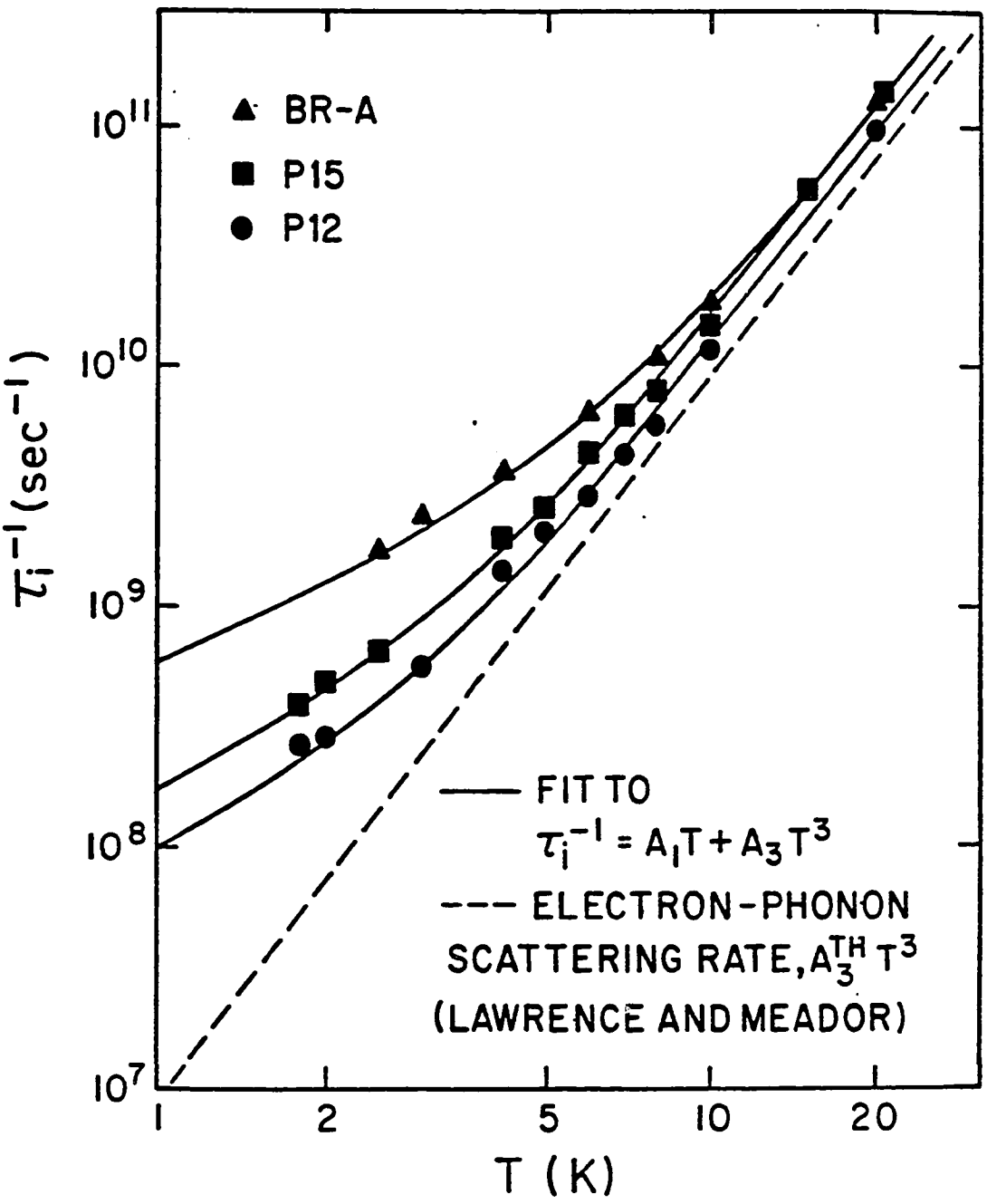

Fig.IV-7 Inelastic scattering rate vs. temperature. Rate for curve BR-A is from our analysis of magnetoresistance data of sample A of Ref.89. Values of A_1 and A_3 are listed in Table IV-2. Electron-phonon scattering rate, Ref.31 is $\tau_{ep}^{-1} = 0.91 \times 10^7 T^3$

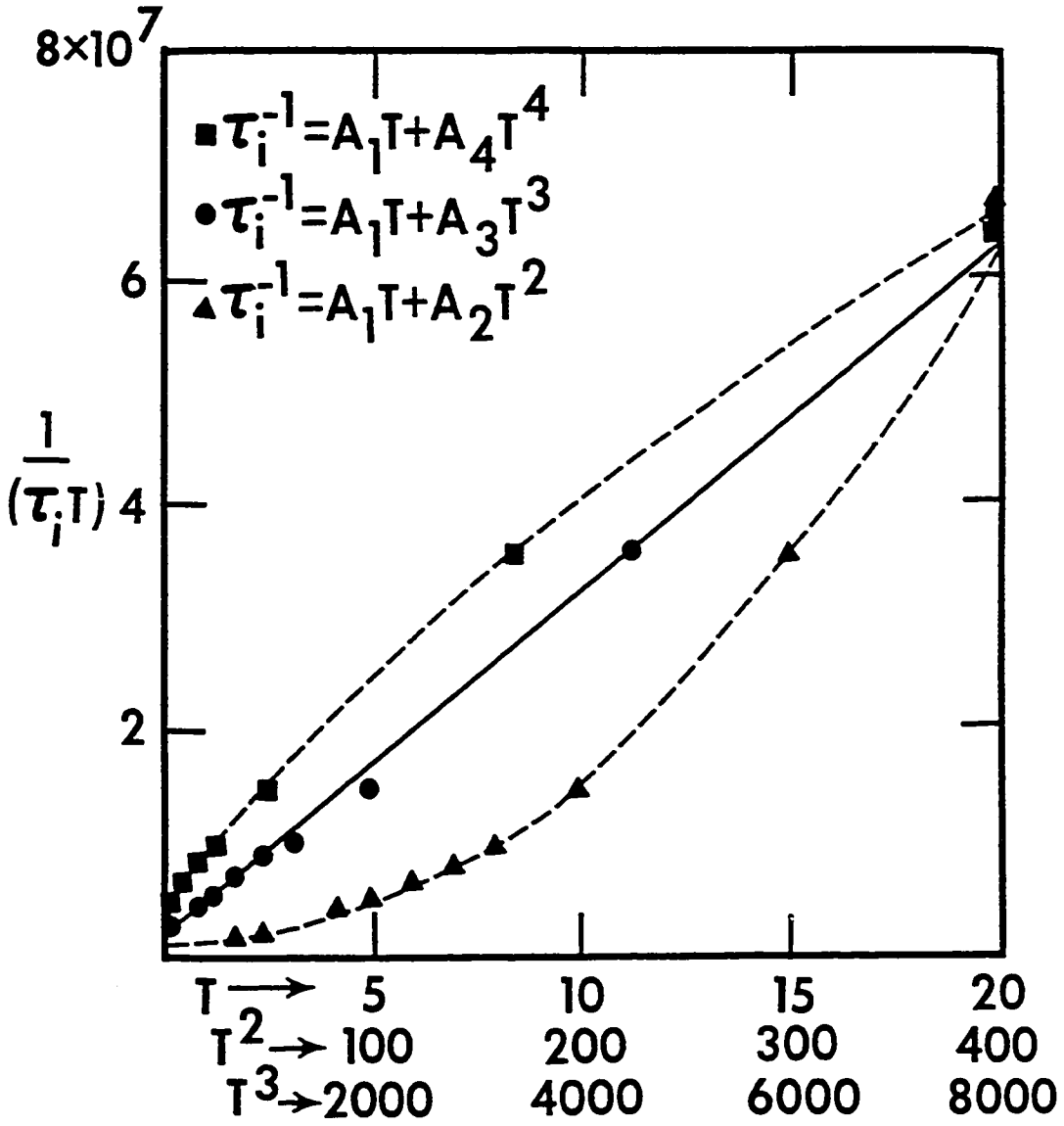

Fig.IV-8 Demonstration of the inadequacy of the other polynomial forms for τ_i^{-1}. Inferred values of $(\tau_i T)^{-1}$ for sample P15 plotted vs. T (▲); vs. T^2(●) ; and vs. T^3 (■). The plots are artificially made to pass through the T=20K point. The function that fits a straight line is the best fit. The straight line corresponds to $\tau_i^{-1} = A_1 T + A_3 T^3$. The dashed lines are guides to the eye.

with different values of A_1 and A_3 for each sample. The fit to Eq.(4.6) is excellent for all samples.

We show in Fig.IV-8, our attempts to fit the τ_i^{-1} data for sample P15 to other functions of the form

$$\tau_i^{-1} = A_1 T + A_n T^n \qquad (4.7)$$

where n=2 and 4. These fits are not satisfactory. Also, functions

$$\tau_i^{-1} = A_2 T^2 + A_n T^n$$

with n=3 or 4 ,do not describe the data satisfactorily.

We now compare the coefficients in Eq.(4.6) from the experiments to the theory for inelastic scattering outlined in Sec II-F. The values of A_3 for various samples are then compared to the electron-phonon scattering prediction of Lawrence and Meador[31], Eq.(2.22) in Table IV-2. As seen in the table, the agreement is very good. The typical phonon wavelength λ_{ph} is smaller the the sample thickness for $T > 3K$ so that the sample is three-dimensional for phonons above 3K. Good thermal matching between Al and glass substrates further enhances the three dimensionality. If the Pippard-Ziman condition (see II-F.1) plays a role in deciding the dimensionality of the electron-phonon scattering, the wavelengths of phonons that cause the most scattering will be smaller than the film thickness (since $\ell < d$). Hence electron-phonon scattering will be three dimensional from this consideration as well. We note that $(q_{ph}\ell) > 3$; this satisfies the criterion for the clean limit [see Sec.(II-F.1)] for electron-phonon scattering. We see in Table IV-2 that for all samples the experimentally inferred values for A_3 agree with the theory of Lawrence and Meador within a factor of two. We consider this to be a good agreement.

TABLE IV-2 Comparison of the coefficients A_1 and A_3 to theoretical predictions[a,b]

Sample	A_1 ($10^7 s^{-1} K^{-1}$)	A_3 ($10^7 s^{-1} K^{-3}$)	$\frac{A_1}{A_1^{Th}}$	$\frac{A_3}{A_3^{Th}}$
Q8	....[c]	1.5	...[c]	1.7
P12	9.0	1.2	2.2	1.3
Q28	13.2	1.8	2.1	2.0
P14	17.8	1.7	2.2	1.9
P15	16.1	1.5	1.9	1.7
T46	....[d]	1.4	...[d]	2.0
L45	....[d]	1.7	...[d]	1.9
T42	34.3	1.4	2.1	1.6
Q20	43.1	2.1	1.9	2.3
BR-A[a]	58.1	1.4	1.9	1.5
BR-B[b]	137.0	2.8	1.4	3.0

a A_1^{Th} is defined in Eq.(2.25)

b $A_3^{Th} = 0.91 \times 10^7$ from Eq.(2.22)

c This sample shows excess scattering at $T \sim 2$ K; see Sec.IV-F.4 .

d At low temperatures T46 (of width 10 microns) and L45 (of width 2 microns) show precursors of a dimensional crossover effect, $\ell_i \sim W$. This precludes an accurate determination of A_1.

The term in the inelastic scattering rate which is linearly dependent on temperature can be due to the two-dimensional dirty-limit electron-electron scattering. As noted in II-F.3, the expression for the electron-electron scattering rate relevant to the localization measurement is Eq.(2.25). This corresponds to small energy transfers. An estimate of the characteristic length ℓ_{int} for our typical thin films with $D \sim 40 cm^2/sec$ gives

$$\ell_{int} \approx \frac{1750 \text{ Å}}{T^{1/2}}$$

where T is in K. The conditions for two dimensionality [see Sec.II-F.3)] are easily satisfied by our films with

$$d < \ell_{int}$$

In Table IV-2 we show a comparison of the coefficient A_1 for various samples from experiment to that expected from Eq.(2.25). The agreement is also very good. For all the samples in Table IV-2 the experimental coefficients A_1 agree with the theoretical result within a factor of two. Again, this level of agreement is good.

Thus we find that the total inelastic scattering is due to electron-phonon scattering and electron-electron scattering with

$$\tau_i^{-1} = \tau_\varepsilon^{-1} + \tau_{ep}^{-1} \qquad (4.8)$$

The quantitative agreement of the inelastic scattering rates with theory confirms that the use of localization theory can lead to understandable inelastic scattering rates in metal films, at least in the case of aluminum.

IV-C.3 Spin-Orbit Scattering

Now we discuss the results for τ_{so} from our MR fits. In Fig.IV-9,

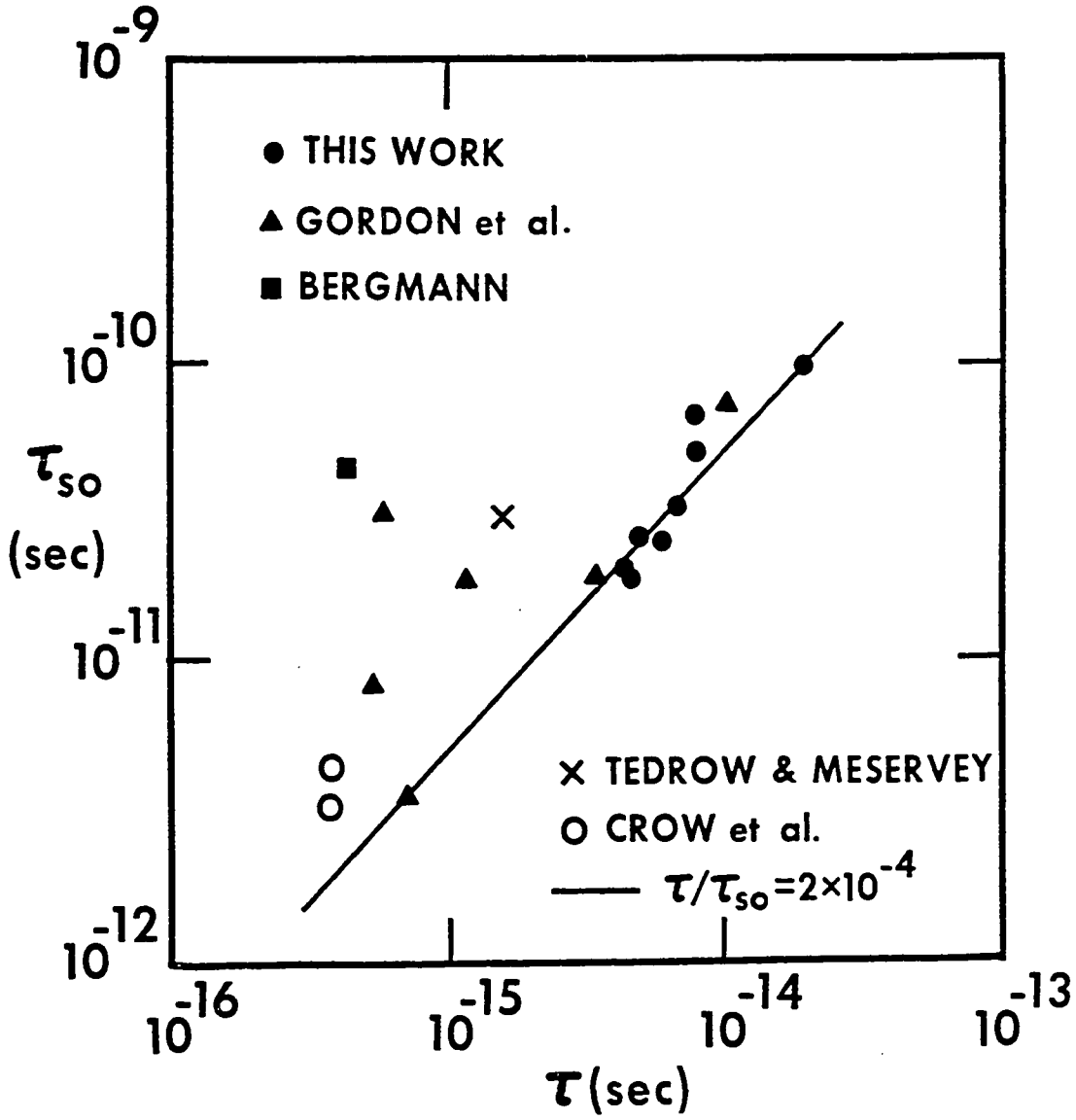

Fig.IV-9 Spin-orbit time in Al as a function of the elastic scattering time . The results from non-localization experiments (Refs.55, 91) and localization experiments(Refs. 82, 86, 97).

the inferred τ_{so} is plotted as a function of τ (note $v_F \tau = \ell$) for eight samples. The solid line corresponds to $\tau/\tau_{so} = 2 \times 10^{-4}$. We find this scaling of τ_{so} with τ for our data sufficient to argue that spin-orbit scattering arises from the same source as that which causes the elastic scattering. Since $\ell < d$, the elastic scattering is due primarily to bulk defects and not due to surface scattering. We control the resistivity (hence τ and ℓ) of the Al films by the rate of deposition of Al. We expect that oxygen incorporated in the film, either as an impurity or as an oxide, causes the elastic scattering. Using Z=8 for oxygen in Eq.(2.27) we obtain

$$\frac{\tau}{\tau_{so}} = 0.12 \times 10^{-4}$$

about <u>20 times smaller</u> than the experimental value. However, if Z=13 (for Al) is used we get 0.8×10^{-4} for the ratio τ/τ_{so}, closer to the experimentally the observed value.

Prior to these localization experiments an estimate of τ_{so} as a function of τ was very difficult to obtain. From the analysis of tunneling data into thin films of superconductors Tedrow and Meservey[55] obtained the spin-orbit scattering rates in those films. Those tunneling experiments required films of thickness ~ 50 Å for satisfactory analyses. Tedrow and Meservey concluded that the scattering of electrons from the boundaries was the mechanism causing spin-orbit scattering. In addition, from a compilation of data from various experiments, they found an approximate Z^4 dependence of the spin-orbit scattering rate, as proposed by Eq.(2.27). Crow et al.[91] studied the upper critical magnetic fields in thin Al films to obtain τ_{so}. We also show the results from these

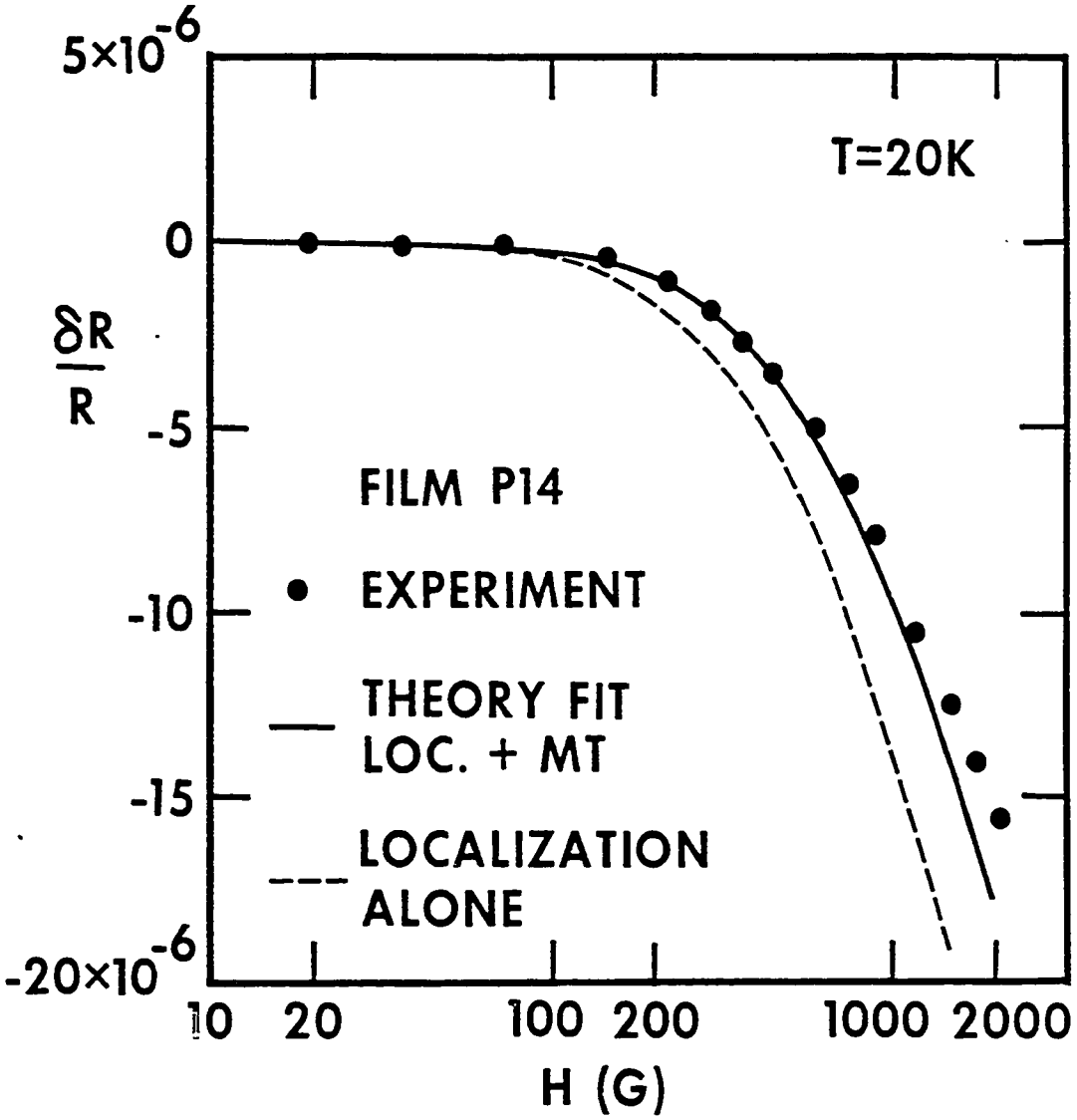

Fig.IV-10 Theoretical decomposition of the observed magnetoresistance into localization and MT contributions .

non-localization experiments in Fig.IV-9 for comparison. We find the agreement to $\tau_i/\tau_{so} = 2 \times 10^{-4}$ satisfactory in all cases. We should note that the quantitative validity of Eq.(2.27) for τ_{so} has not been proven unambiguously by experiments. We discuss the results on spin-orbit scattering rate in Al from the other localization experiments, by Gordon et al. and by Bergmann, in Chapter VI.

IV-C.4 Comments on the Relative Magnitudes of the Localization and MT Terms

It is not possible to perform an experiment to fully separate the localization and MT contributions for Al. However, we can address theoretically the question of their relative importance. In Fig.IV-10 we show the experimental magnetoresistance data for P14 at T= 20K. The theoretical fit is the solid line (which includes the localization and MT contributions) done as described in IV-C.1. The dashed line corresponds to the localization term alone with the same values of H_i and H_{so}. We see that even at T=20K ($T_c \sim 1.4$K) the contribution due to the MT term is not negligible, though it is small.

IV-D RESISTANCE AS A FUNCTION OF TEMPERATURE

Most of the early experiments on thin films measured resistance as a function of temperature in order to observe a resistance increase with a decrease in temperature due to localization. Since we have aluminum as our material, the resistance decrease due to superconducting fluctuations has to be taken into account (see II-A).

IV-D.1 Fitting Procedures

The experimental R(T) data for sample Q28 in the temperature range 2K to 16K are shown in Fig.IV-11. We have matched the theory to the

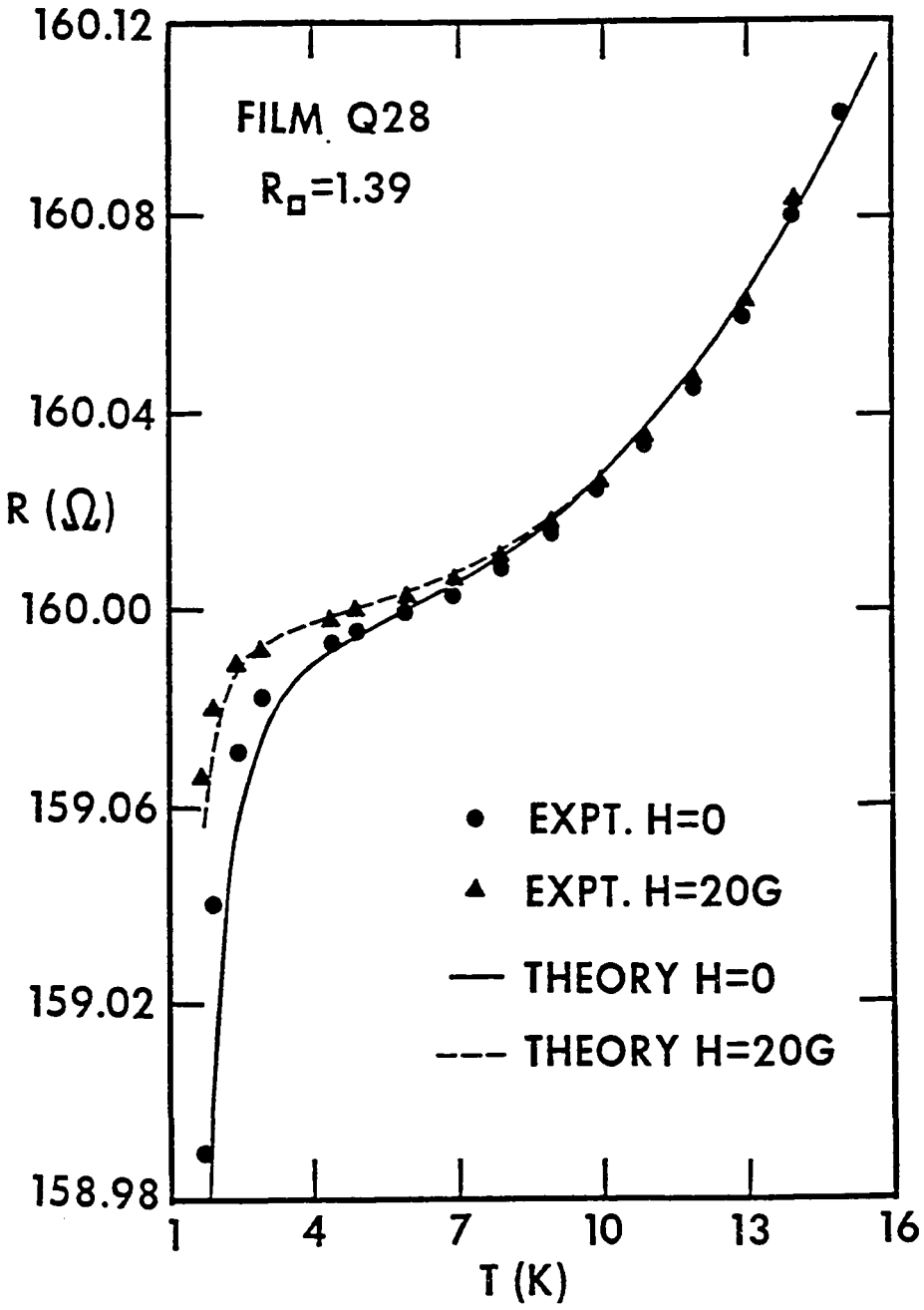

Fig.IV-11 Resistance vs temperature for 2D film Q28. The theory fit was matched to the experimental data at T= 6K. The only fitting parameter was $C_{ph} = 1.9 \times 10^{-7}$.

experimental data at 6K. The solid line is the theory fit which comprises the sum of equations (2.10),(2.11),and (2.16) [corresponding to localization and MT fluctuations]. The classical electron-phonon contribution is fitted by

$$\frac{\Delta R^{ph}}{R} = C_{ph} T^3 \qquad (4.9)$$

H_i, H_{so} and C_{ph} are the three parameters for the theory curve. However, H_i and H_{so} were already determined from fitting the magnetoresistance data and hence are not adjustable for this figure. Thus only C_{ph} is a free parameter here. The general shape of the curve is due to the fact that at high temperatures the electron-phonon scattering of Eq.(4.9) is dominant and at the lowest temperatures the Maki-Thompson term [Eq.(2.16)] is dominant.

Fig.IV-11 also shows the experimental data and the corresponding theory fit (dashed line) at H= 20 G. For such a small field, the classical magnetoresistance is negligible and the changes in the shape of the curve are mainly due to the change in the localization and MT terms due to the application of the field. A small shift (a few millikelvins) in T_c is experimentally measured (also included in the data analysis) but it is not the main reason for the changes in R(T). The parameters [H_i, H_{so}, $\beta(T/T_c)$ and C_{ph}] used for the fit with H = 20G are the same as those for H=0.

IV-D.2 Relative Magnitudes of Various Contributions

We indicated above that in the temperature range 2K < T < 16K the only significant contributions to R(T) are from localization, MT fluctuations and classical electron-phonon scattering. For the sake of

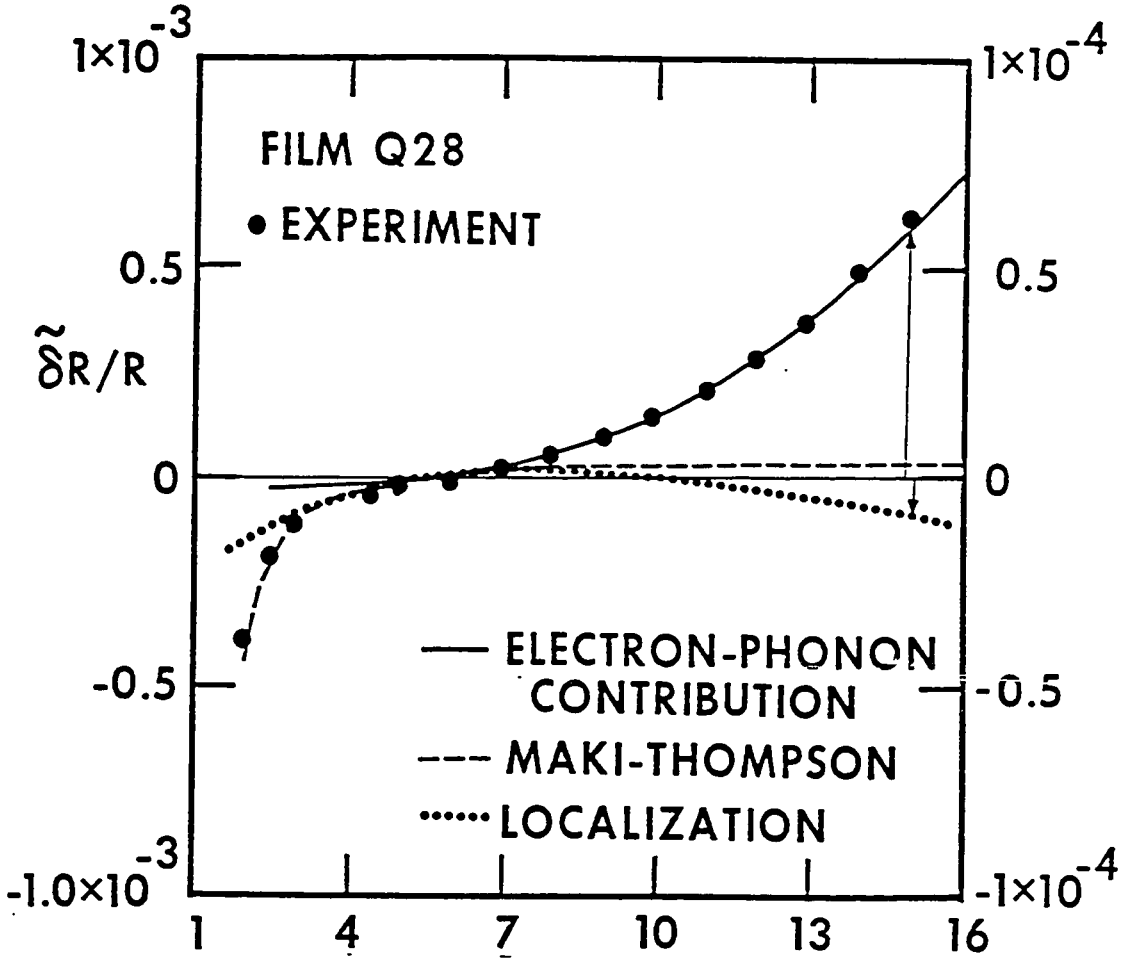

Fig.IV-12 The decomposition of $\tilde{\delta}R(T)$ for sample Q28 into individual contributions. For the localization contribution only (dotted line), see the enlarged vertical scale on the right. For T> 7K, the electron-phonon term is dominant and for T < 4K, the MT term is dominant. For 4K < T < 7K, all the terms are comparable and small. Reference temperature is 6K .

Table IV-3. Comparison of electron-phonon coefficients A_3 and C_{ph}.

Sample	A_3 (10^7 $s^{-1}K^{-3}$)	C_{ph} (10^{-7} K^{-3})	τ (10^{-14} s)	$\frac{A_3\tau}{C_{ph}}$
P12	1.2	2.0	0.82	0.5
Q28	1.8	1.9	0.81	0.8
P14	1.7	1.0	0.52	0.9
P15	1.5	0.8	0.48	0.9
Q20	2.1	1.0	0.46	1.0

completeness, we show in Fig.IV-12 the decomposition of the overall R(T) into the various individual terms. For $T > 7K$ the electron-phonon term is dominant and for $T < 4K$ the MT term is dominant. Only in a small range of temperature $4K < T < 7K$ the localization term is comparable to the MT contribution and the electron-phonon contribution.

Furthermore, we note that $H_{so} \ll H_i$ at high temperatures and $H_{so} \gg H_i$ at low temperatures. Consequently, the contribution due to localization [Eqs.(2.10) and (2.11)] is only about a tenth of the rise predicted in the absence of spin-orbit scattering as the temperature initially goes down from 20K. Then $\tilde{\delta}R$ due to localization starts going down with further decrease in temperature. Thus, the role of spin-orbit scattering is crucial in deciding the quantitative behavior due to localization . The agreement seen at the low temperatures confirms the theoretical expression for the MT contribution and the inferred inelastic rate from the magnetoresistance.

IV-D.3 The Value of C_{ph}

The value of C_{ph} inferred in Sec IV-D.1 should be related to A_3 inferred from magnetoresistance in Sec.IV-C.2 . Using a simple Drude model[12],

$$\frac{\rho_{ph}}{\rho_0} = \frac{\tau_{ep}^{-1}}{1/\tau} = \frac{A_3 T^3}{1/\tau} = \left(\frac{A_3 \ell}{v_F}\right) T^3 \qquad (4.10)$$

such that $C_{ph} = (A_3 \times \ell)/v_F$. This relationship assumes that all inelastic scattering events contribute to the resistance and there is no restriction on scattering angles. The participation of large angle electron scattering processes is due to the dominance of the umklapp electron-phonon processes over the normal electron-phonon processes in

Al[26,87,92] at all temperatures. We show the values $(A_3 \times \ell)/(v_F \times C_{ph})$ for various samples in Table IV-3. As expected, they are all close to unity. Thus we conclude that the resistivity due to electron-phonon scattering in our samples varies as T^3 in the temperature range 2K to 20K.

IV-E PARALLEL FIELD MAGNETORESISTANCE

We have done measurements on one sample P14 in both parallel and perpendicular field orientations. The goal was to verify the theoretical prediction for parallel fields and see if the parameters H_i and H_{so} are the same as those for perpendicular field. Sample P14 was codeposited with P15 but was measured about a year after P15. The basic film properties of P14 related very well to those of P15 (see Table IV-1).

The inferred values for τ_{so} and τ_i from perpendicular magnetoresistance also agreed well with those for P15 (see Table IV-2). First, perpendicular field measurements on P14 were done as described previously. P14 was then mounted on a stub designed for parallel fields, and was measured on a different day. We did <u>not</u> attempt to verify the deviation from parallel orientation in any systematic fashion and hence could not rule out the possibility of a small perpendicular component to the field. However, in order to avoid a more complicated analysis with one more parameter (tilt angle), we chose to do the analysis with just the parallel field theory,and looked for self-consistency. Since this study was not a major aspect of our work, we did not construct an adjustable parallel field sample holder.

IV-E.1 Parallel Superconducting Critical Field Measurements

As a preliminary verification of the basic film behavior, we studied

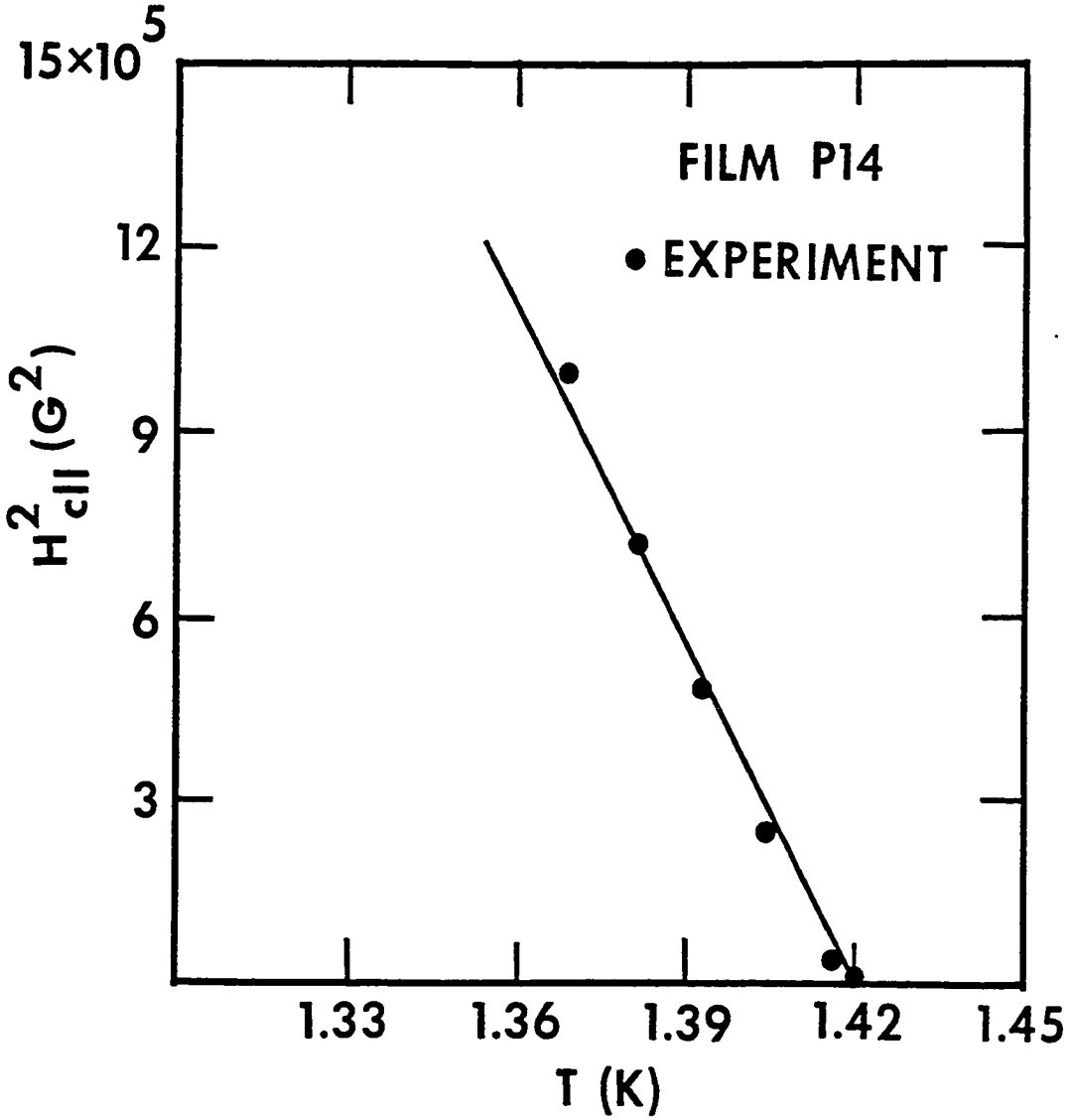

Fig.IV-13 Square of the parallel field applied as a function of the measured T_c values. The straight line is the fit to Eq.(4.11).

the temperature dependence of the parallel superconducting critical field. $H_{c2\parallel}$ is given by (see Appendix F)

$$H_{c2\parallel}^2 = 0.79 \frac{\Phi_0^2}{d^2} \frac{k_B}{\hbar D}(T_c - T) \qquad (4.11)$$

One can obtain the diffusion constant from a plot of of $H_{c2\parallel}^2$ as a function of T using the known value of the thickness of the film. In addition, the H=0 intercept of the curve gives an independent value for T_c.

Fig.IV-13 shows $H_{c2\parallel}^2$ as a function of T for sample P14. The observed behavior confirms the theory for parallel critical fields. We inferred a diffusion constant of 38 cm^2/sec from our fitting. This is to be compared with 29 cm^2/sec obtained with the perpendicular field measurement. We consider this a satisfactory agreement. (Note that an error of 10% in the value of film thickness would result in an error of 20% for the diffusion constant). The value of T_c = 1.421K inferred from the two fitting parameters in Fig.IV-13 agrees well with the directly measured value of T_c=1.416K. These results for the superconducting critical field measurements confirm that the sample does behave properly in a parallel field configuration.

IV-E.2 Fitting Procedures for the Parallel Magnetoresistance and Results

The qualitative behavior of the magnetoresistance for the parallel and perpendicular field measurements is similar. At low temperatures, positive magnetoresistance is observed both in perpendicular and parallel field orientations. Similarly, negative magnetoresistance is observed at high temperatures. This already confirms the relative magnitudes of H_i and H_{so}. However, there is an appreciable magnetoresistance at low

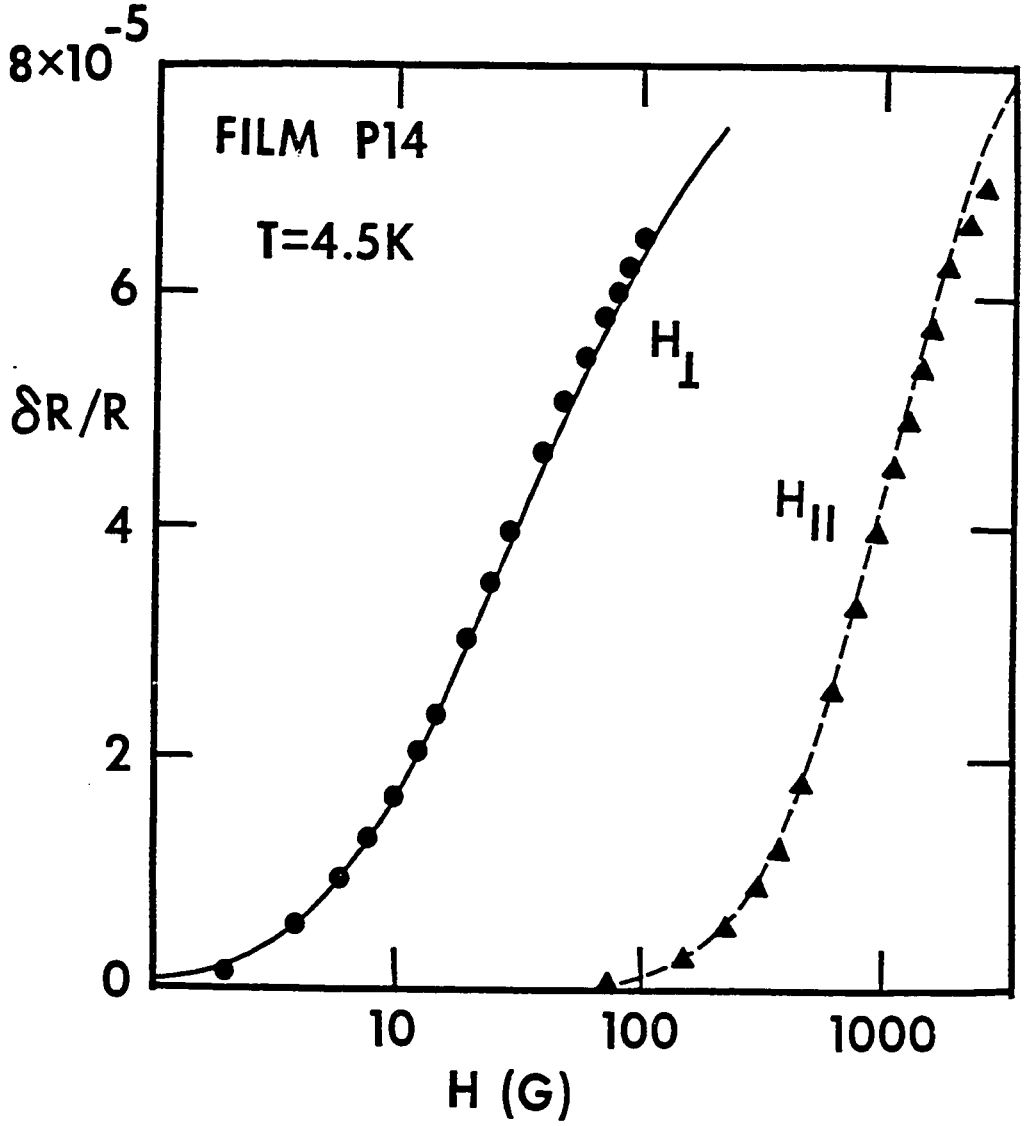

Fig.IV-14 Comparison of parallel and perpendicular magnetoresistance data for sample P14. The fit parameters are H_i=1.35G and H_{so} = 21G for the perpendicular field data (●). For the parallel field data the fit parameters are H_i = 1.8G and H_{so}=31.5G.

fields in the case of perpendicular orientation. In the parallel orientation one needs a field typically one order of magnitude larger for comparable size magnetoresistance.

As indicated in Chapter II the theory for parallel fields is a perturbation calculation and valid only for fields $H < 12\ H_d$ (see Sec.II-B.7). Since d = 250Å, this condition restricts applied fields to be less than $\sim$10 kG . This restriction is of no consequence in our analysis. However, at fields $\sim$1kG other contributions (such as classical magnetoresistance which is isotropic, since $\ell < d$) should not be ignored.

Fig.IV-14 shows the magnetoresistance data at 4.5K for sample P14 in parallel and perpendicular fields. The theory used in the fit includes the localization and MT terms as described in Chapter II. We use the same value for the parameter $\beta(T/T_c)$ for both the fits, taken from Ref.23. The fitting for the parallel orientation was done independently of that for the perpendicular orientation. The fits are excellent. The inferred H_i and H_{so} for these fits differ only by a factor of $\sim$1.5. We consider this agreement satisfactory. Similar fits are obtained for all temperatures below T$\sim$10K for the parallel field data.

At higher temperatures, we see a measurable magnetoresistance only in larger fields (H > 1kG). From our discussion of magnetoresistance at high fields (in Sec.IV-B) we should expect a contribution from classical magnetoresistance given by Eq.(4.5). The experimentally observed behavior is consistent with an inclusion of classical magnetoresistance in the analysis, in addition to the localization and MT contributions. Thus, in our experiments in parallel magnetic fields, we find good agreement with theory for the magnetoresistance. The parameters inferred are quite reasonable when compared to perpendicular field results.

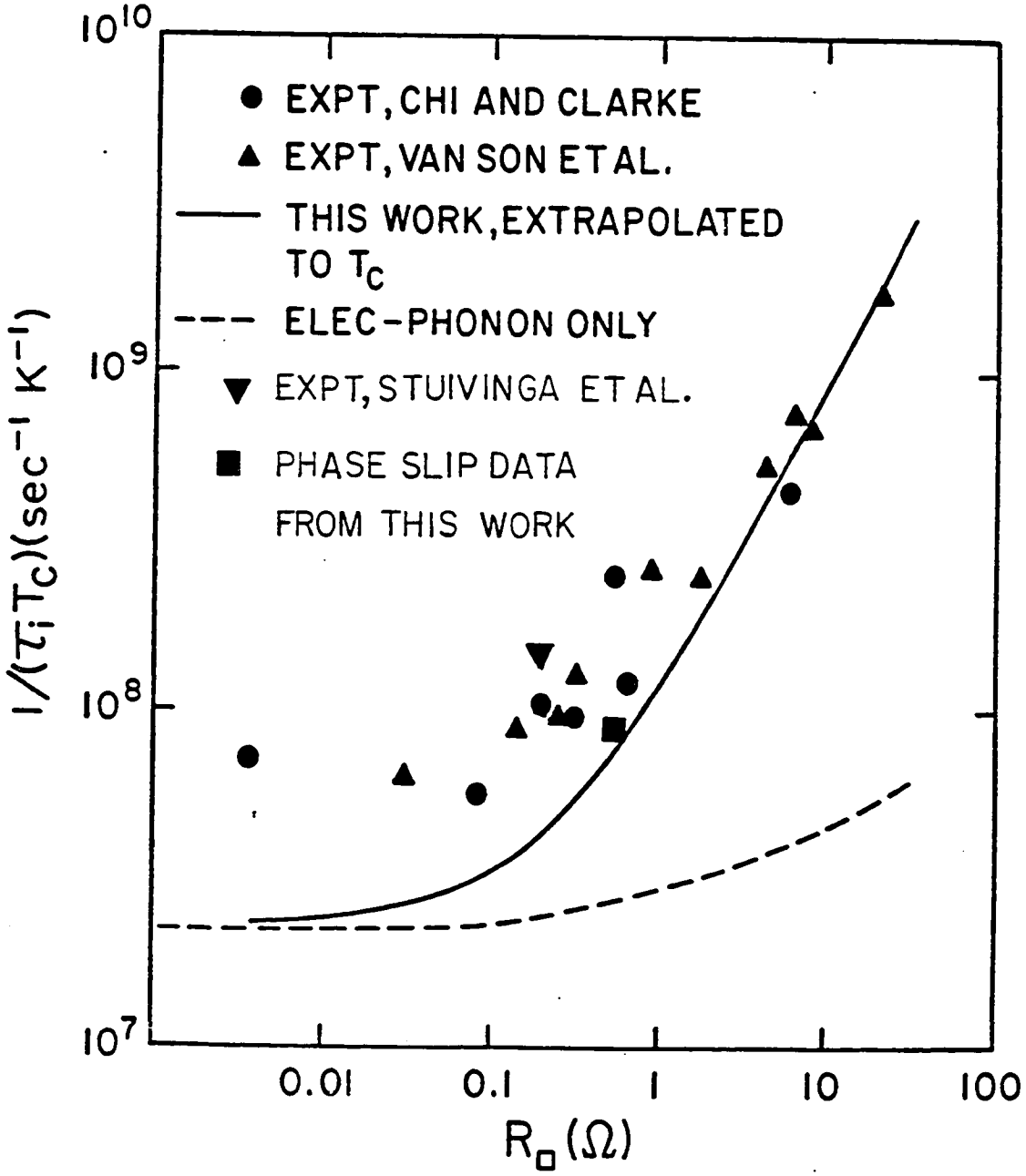

Fig.IV-15 Inelastic scattering rate divided by T_c as function of sheet resistance $R_\square$.

IV-F COMPARISON TO INELASTIC TIMES FROM SUPERCONDUCTING EXPERIMENTS

IV-F.1 Tunneling Experiments

Now we turn to some 'anomalous' behavior observed in superconducting tunneling experiments (see Sec.II-H.3) on Al films by Chi and Clarke[60]. These experiments directly infer $\tau_i(E_F)$ from the charge-imbalance relaxation. They do not require knowledge of $\rho_o \ell$ products or diffusion constants. The inelastic scattering rate deduced by Chi and Clarke was larger than the electron-phonon rate; it increased with $R_\square$. These authors did not note the dependence on $R_\square$, but it can be deduced from their tabular summary of the results. We show their experimental data for $(\tau_i T_c)^{-1}$ vs $R_\square$ in Fig.IV-15. The solid line is our prediction for their samples based on our experimentally determined average coefficients $A_1/R_\square$ and A_3. In the case of the high resistance films ($R_\square > 1$ ohm) the agreement between the inelastic scattering rate inferred from localization and the tunneling experiments is very good. The result indicates that the rise of τ_i^{-1} with $R_\square$ is due to dirty limit electron-electron scattering.

IV-F.2 Microwave Gap Enhacement Experiments

van Son et al.[93] measured the minimum microwave frequency for the superconducting critical current enhancement in 2 micron strips of aluminum just below to T_c. Their films were deposited under identical conditions and differed only in the thickness. The inferred inelastic scattering rates from their experiments are also shown in Fig.IV-15. The magnitude of τ_i deduced from these experiments did not require a knowledge of diffusion constants or $\rho_o \ell$ products. These authors independently concluded that the observed dependence of the inelastic rate on $R_\square$ was due to dirty-limit electron-electron scattering.

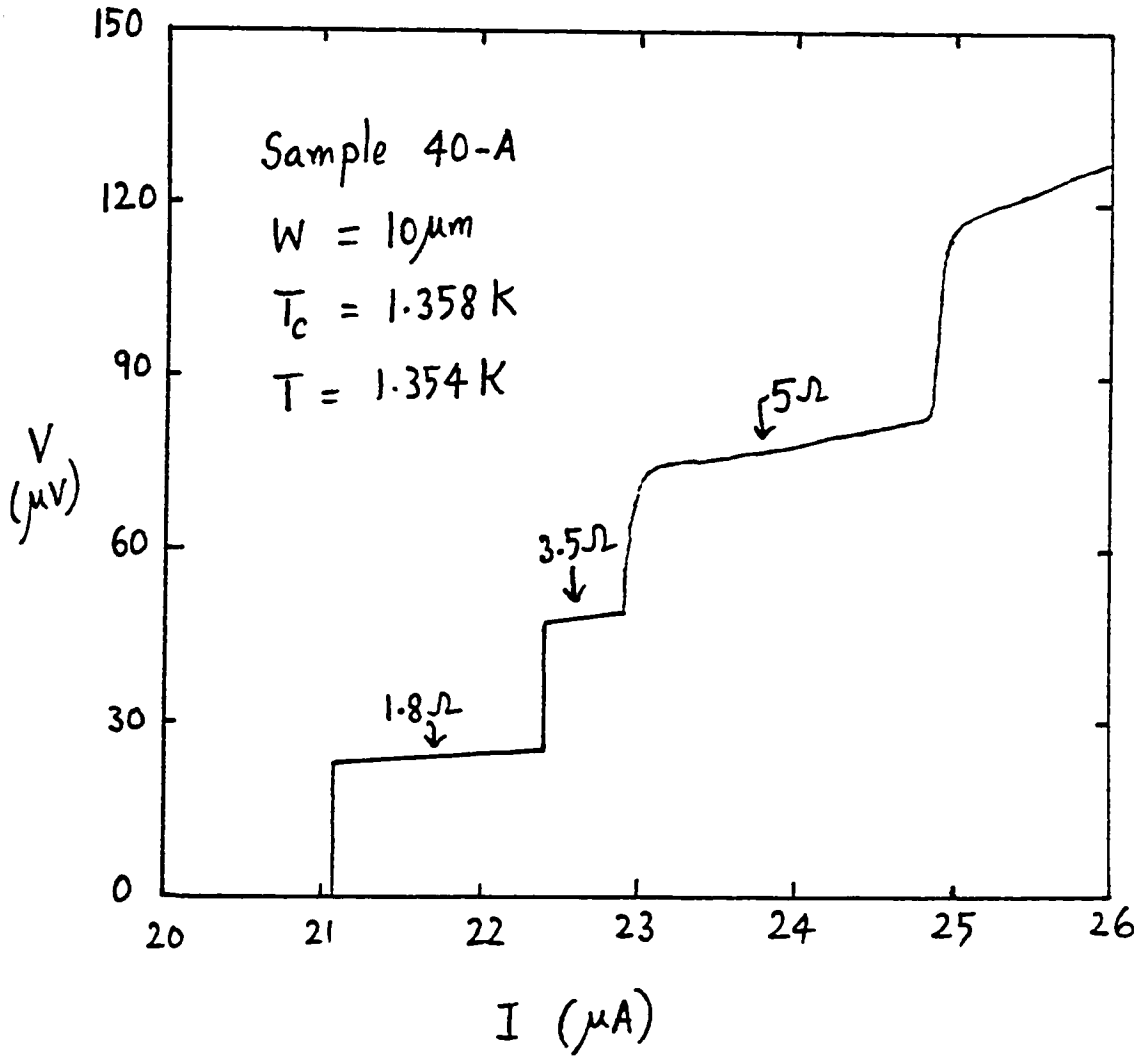

Fig.IV-16 Voltage-current plot for sample 40-A. The minimum unit for differential resistance R_d = 1.7 ohm.

Table IV-4 Sample details for the phase-slip experiments

Sample	Width (microns)	$R_{\square}$ (4.5K) (ohm)	d (Å)	T_c (K)	D[b] (cm^2/s)	$\tau_i(T_c)$ (nS)
40-A	10.0	0.57	700	1.358	32.5	8.8
1[a]	2.4	0.20	430	1.25	153.0	4.8

a Sample 1 of Stuivinga et al.(Ref.64)

b D was calculated assuming $\rho_o l = 3.0 \times 10^{-12}$ ohm-cm^2 (see text).

IV-F.3 Phase Slip Experiments

In the early stages of this work, we performed a few experiments to study phase-slip centers in narrow strips of Al (see Sec. II-H.3). These experiments were restricted to temperatures just below T_c and yielded an estimate of the inelastic scattering rate at $T \sim T_c$. We briefly discuss our results from a 10 micron wide strip, sample 40-A fabricated using optical lithography. 40-A had an $R_\square \sim 0.5$ ohm. More details of the film properties are shown in Table IV-4.

Since the width of the sample was 10 microns the experiments had to be done within a few millikelvins from T_c in order to satisfy the condition that the sample width be smaller than the the coherence length $\xi(T)$ and the penetration depth $\lambda(T)$. Fig.IV-16 shows the current-voltage characteristics of 40-A at $T = 0.997\ T_c$. The step structure seen is the one described in Sec.II-H.4. It is due to formation of phase slip centers along the length of the sample. The average minimum unit for the increase in differential resistance R_d is = 1.7 ohms. Using Eq.(2.30), this corresponds to a quasiparticle charge imbalance length $\lambda_{Q*} = 14.9$ microns and a charge imbalance relaxation time $\tau_{Q*} = 68$ nS. Eq.(2.29) can be readily used to obtain τ_i at $T \sim 1.35$ K as 8.8 nS.

R_d is expected to show a weak divergence as $T \to T_c$ due to the presence of the superconducting energy gap Δ in Eqs.(2.29) and (2.30). However, experimentally R_d was essentially independent of the temperature at which the phase slip measurements were made, in contradiction with the theory. A similar temperature independence of R_d was reported in some early phase slip experiments[61]. Subsequently, the divergent behavior of R_d as $T \to T_c$ was shown to be obscured by heating effects[61]. Thus

experiments on phase slip centers through the study of differential resistance of current-voltage characteristics are not entirely dependable for their quantitative results. We believe that the τ_i value derived from PSC measurements is of reasonable qualitative guidance. Therefore, we compare the value of τ_i^{-1} from our phase slip experiments to the results of our localization experiments in Fig.IV-15 for completeness.

Stuivinga et al.[64] studied spatial dependence of the electrochemical potential for quasiparticles (see Sec.II-H.4). They obtained for a film of $R_\square$ = 0.2 ohm at 1.25 K a value of τ_i = 4.8 nS*. (see Table IV-4 for the film properties). Their result is also shown in Fig.IV-15.

IV-F.4 Conclusions

The satisfactory agreement observed in Fig.IV-15 among τ_i from the four different kinds of superconductivity experiments (done by three different groups) is quite impressive. The role of inelastic electron-electron scattering in charge-imbalance relaxation was considered theoretically by Entin-Wohlman and Orbach[94]. They proved that in the case of both clean and dirty superconductors, the electron-electron scattering rate adds to the electron-phonon scattering rate in causing charge-imbalance relaxation. However, the inelastic scattering rate inferred from the phase relaxation of the Cooperon in localization experiments may be, in principle, different from that appearing in charge-imbalance relaxation experiments. In any case, based on Fig.IV-15, we can conclude that the magnitude of the electron-electron scattering measured in

---

* We have multiplied the value of τ_i given by the authors by three in quoting here since we believe that $\rho_o \ell$ = 3 x10^{-12} ohm-cm^2 is relevant (see Fig.IV-2) in this resistivity range instead of the 9 x10^{-12} ohm-cm^2 used by those authors.

localization is close to the inelastic rate which is relevant in superconductivity experiments.

Now we discuss Fig.IV-15 with respect to the behavior of clean films with $R_\square$ < 1 ohm. In the low resistance films of Chi and Clarke (as well as those of van Son et al.) both electron-phonon and dirty-limit electron-electron scattering are too small to account for the experimental rates. In fact, our sample Q8 with $R_\square$ = 0.17ohm also shows excess scattering. We speculate that this extra scattering is due to clean-limit electron-electron scattering. A recent theoretical calculation of this effect for strictly 2-D systems[48] yields $\tau_{ee}^{-1} = 1.7 \times 10^7 T^2$ within a factor of $\sim$3 of the extra scattering seen in Fig IV-15. Our data for sample Q8 are also consistent with such a term. Clean limit electron-electron scattering has also been found to play a role in MOSFETs[95]. More theoretical and experimental work is needed for this regime.

V. EXPERIMENTAL RESULTS: NARROW WIRES

The work reported in this chapter was done in close collaboration with S. Wind . The author is indebted to S. Wind for the fabrication of the submicron wires using x-ray lithography (see Sec. III-E.3) and for his generous assistance in the low temperature experiments and data analyses.

V-A SAMPLE PARAMETERS

V-A.1 Determination of $R_{\square}$ and T_c

The discussion in Sec.IV-A of the various important characteristics of thin films is relevant here also. Measurements of film thickness, Residual Resistivity Ratio and T_c were done as for the thin films. We have used a dc bias current of 0.5 microamp in tracing the superconducting transitions of the wires. The determination of $R_{\square}$ and the elastic mean free path for the narrow wires deserves some discussion.

We needed to observe the sample in a SEM to determine its width, length and uniformity. Since it is not known if the properties of the film are affected by the exposure to the electron beam in the SEM, we chose to do the SEM observation <u>after</u> the low temperature experiments. A careful study of the sample in a high resolution Zeiss optical microscope, prior to low temperature measurements, was sufficient to have a rough idea of the sample width. Electrical measurements, of course, verified the continuity of the sample. The length of the wires was $\sim$210 microns. The uniformity of the widths of the wires was $\sim$5% in all cases discussed below. We used <u>the $R_{\square}$ inferred from the measured sample</u>

TABLE V-1 Parameters for narrow wires. $R_{\square}$ is at 4.5K

Sample	$R_{\square}$ (ohms)	d (A)	T_c (K)	W (micron)	ℓ_{so} (micron)	$\ell_{i(4.5K)}$ (micron)
A	0.9	250	1.35	0.20	0.48	1.47
B	1.2	240	1.34	0.24	0.57	1.28
C	2.8	150	1.45	0.60	0.32	0.98
D	4.5	150	1.49	0.40	0.30	0.78

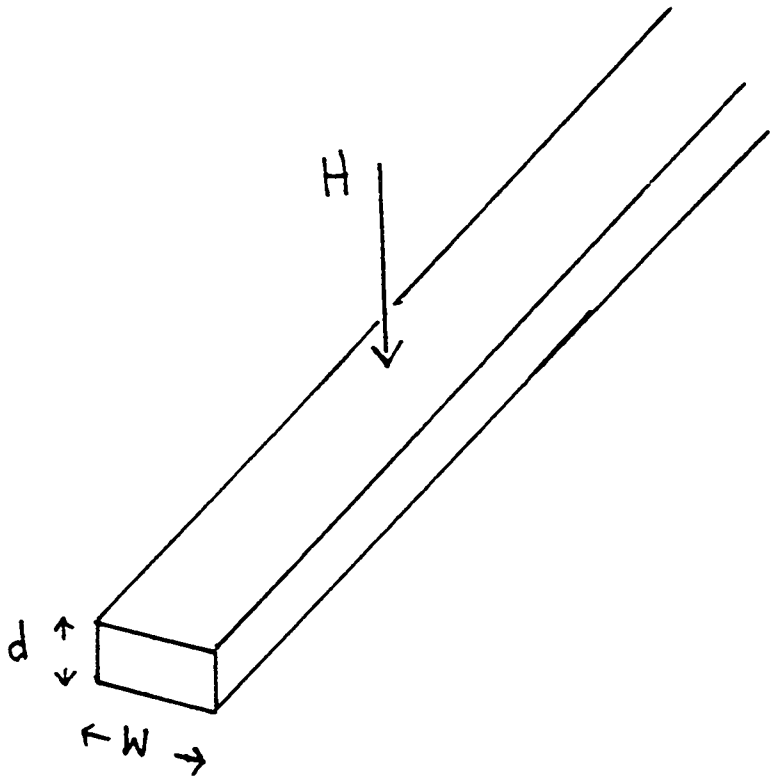

Fig.V-1 The field orientation for magnetoresistance measurements on narrow wires.

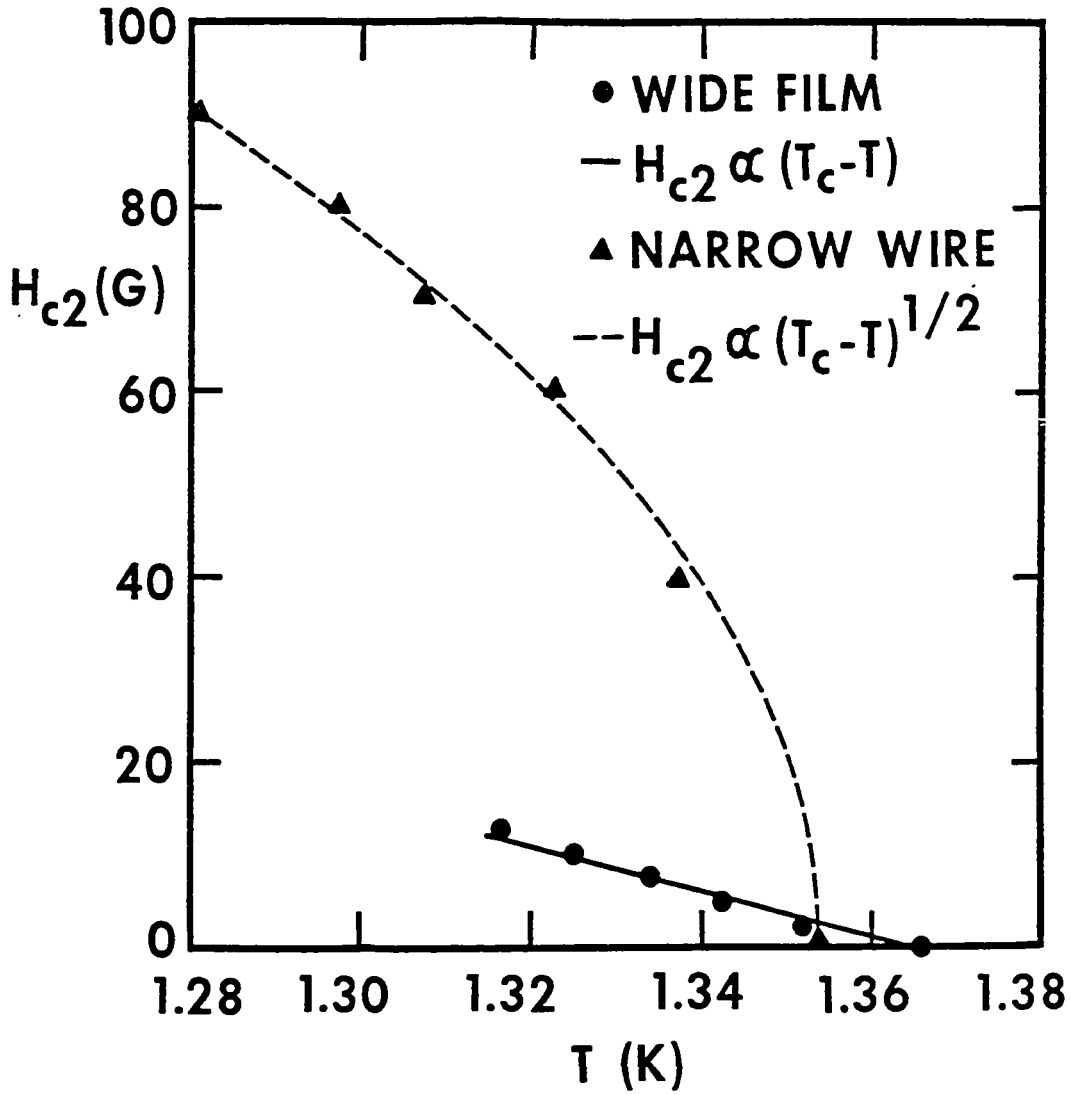

Fig.V-2 Comparison of the perpendicular critical field data for a narrow wire and the corresponding wide film. The transition temperatures of the samples differ by 15mK due to small difference in their material properties.

dimensions for the narrow wires in our data analyses. Table V-1 shows the film properties of the narrow wires studied.

V-A.2 Determination of the Diffusion Constant from Perpendicular Critical Field Measurements

We consider the narrow wires placed in a perpendicular magnetic field, as shown in Fig.V-1. In contrast to two-dimensional films which obey Eq.(4.1) in perpendicular fields, the narrow wires showed

$$H_{c2\perp} \propto (T_c - T)^{1/2} \tag{5.1}$$

as seen in Fig. V-2. We interpret this behavior as due to the fact that the superconducting coherence length $\xi(T)$ is larger than the sample width at $T \sim T_c$. The situation, then, is similar to that of a superconducting thin film in a parallel field. This would lead to the behavior indicated in Eq.(4.11). However, one should use the width W instead of the film thickness d in Eq.(4.11). Therefore, we can determine the diffusion constant in the case of the narrow wires from a fit to H_{c2} - T data. A test for the validity of this approach is the comparison of the value of T_c obtained from the fitting parameters in the $H_{c2\perp}$ -T plot to the directly measured value of T_c.

We found good fits to Eq.(4.11) (with W instead of d) in the cases of the four experimental samples studied. The T_c values inferred from the $H_{c2\perp}$ - T fits agreed with the directly measured T_c values to within a few millikelvins.

V-A.3 Comparison of the Material Properties of Wires and the Codeposited Films

In films of the same thickness and comparable resistivity, the

resistive transition was broader (and less smooth) in the case of a wire than that of a wide film. The broader transition in narrow wires could be an intrinsic effect due to the one-dimensional [W,d $<<\xi(T)$] nature of the fluctuations close to the transition. Zwicknagl and Wilkins[96] have shown how macroscopic inhomogeneities in superconducting samples also broaden the <u>width</u> of the superconducting transition. Inhomogeneities in the wires can also cause the 'bumpiness' of the transitions. This is likely since the bias current can be larger than the critical current of a specific region of the wire, making that part of the sample stay normal until a lower temperature is reached. Simple T_c variations may also lead to a bumpy transition.

The experimental value of $R_\square$, from the measured geometry of the wires, was smaller for the wires than for the codeposited wide film, by a factor of $\sim$1.2 in the best case and by a factor of $\sim$1.5 in the worst case. In addition, the residual resistance ratios for the wires are larger by $\sim$8% than those of the corresponding wide films indicating a real (but small) difference in the resistivity of the films. The transition temperatures of the wires were also lower than those of the corresponding wide films by $\sim$15 mK, which is also consistent with the difference in their resistivities.

The values of the diffusion constant from the $H_{c2\perp}$-T fits for the wires were larger than the values for the corresponding codeposited wide films by a factor of $\sim$1.2 in the best case to $\sim$2.2 in the worst case. It is worth noting that the order of the samples in the 'best to worst' sequence was the same for $R_\square$ as for the diffusion constant.

The small differences in the material properties of wires and films are attributed to physically different locations of the narrow wire and

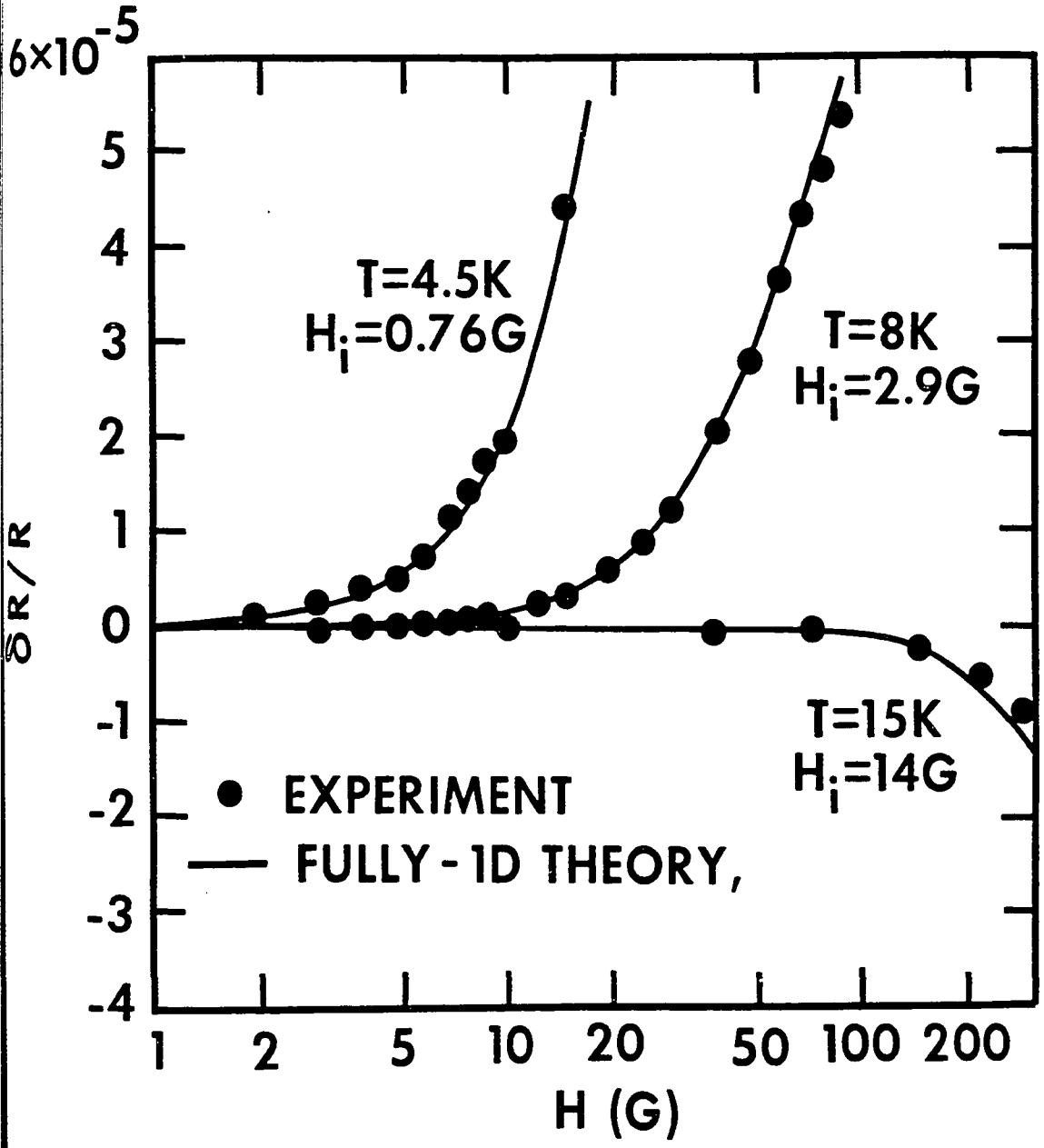

Fig.V-3 Normalized magnetoresistance for sample A. H_{so}= 7G for theory curves.

the wide film in the evaporation chamber. In addition, the narrow wires were fabricated on oxidized silicon wafers whereas the wide films were fabricated on glass substrates. In order to avoid possible complications due to the choice of the diffusion constant in the comparison of the scattering times, in the later sections we compare the diffusion lengths (which are directly inferred in the experiments) instead of the scattering times. Also, the small differences in $R_\Box$ will only appear as a higher order correction to the inelastic scattering lengths inferred . This is because at low temperatures, where electron-electron scattering is dominant, we expect [see Eq.(2.25)]

$$\ell_i \propto R_\Box^{-1/2}$$

V-B FULLY-ONE-DIMENSIONAL SAMPLES

V-B.1 Magnetoresistance in Perpendicular Fields

As seen in Sec II-B.4, to be in the fully-one-dimensional regime, we need samples such that $W < \ell_i$ and ℓ_2 . We discuss the behavior of Sample A of width 0.2 micron to illustrate this case. Fig.V-3 shows the normalized magnetoresistance data for Sample A. The theoretical expression which comprises localization and MT fluctuations [the sum of Eqs.(2.9), (2.13), and (2.18)] is shown by the solid lines. The analysis was similar to the two-dimensional case. Values of H_i and H_{so} were chosen for best fits. $\beta(T/T_c)$ was taken from Ref.23 as for 2D films (see Appendix G). We note that since the theoretical result [Eq.(2.13) and Eq.(2.18)] is a perturbation calculation for small fields (see Appendices A-C) we show the magnetoresistance data for only up to 300G. The limit-

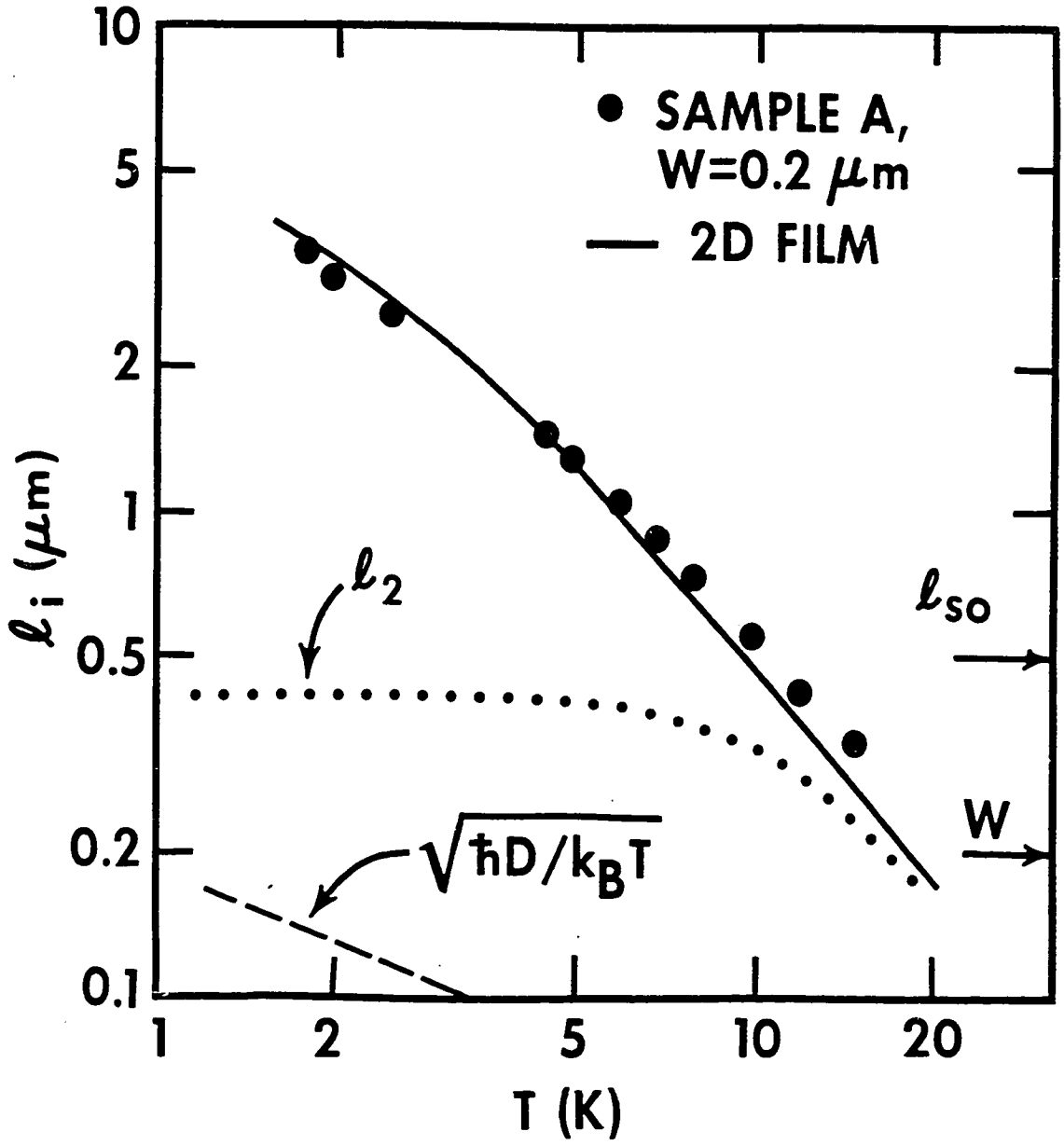

Fig.V-4 Inelastic diffusion length vs. temperature. The solid line is the experimentally determined ℓ_i for the co-deposited wide film. Upto 15K, $W < \ell_2$, ℓ_i as required for fully-one-dimensional behavior. ℓ_{so} is the spin-orbit scattering length [= $(D\,\tau_{so})^{1/2}$].

ing field H (beyond which the theory is not adequate) for sample A is ~300G.

From our fits we find that the magnetoresistance obeys the fully-one-dimensional form over the entire temperature range 1.8K to 15K. Fits to the two-dimensional theoretical form were not satisfactory. We discuss the interpretation of the fitting parameters in the next sections.

V-B.2 Spin-orbit Scattering Length in Wires

H_{so} obtained for a given sample was essentially independent of temperature as was found for 2D films. The spin-orbit diffusion lengths inferred for wire A and the codeposited wide film agreed within ~20%. The spin-orbit diffusion length inferred from the fit for sample A was 0.5 micron, consistent with the requirement $W < \ell_{so}$ for the fully-1D analysis. A similar result was obtained for the other fully-1D wire, Sample B.

V-C INELASTIC MECHANISMS IN WIRES

The inelastic scattering length $\ell_i(T)$ inferred from the fits is plotted in Fig.V-4 for wire A. For comparison we show the $\ell_i(T)$ for the codeposited wide (2D) film. The agreement between them is excellent. In addition, we note that the inferred inelastic scattering lengths are <u>larger</u> than the sample width. This further confirms our use of the fully-1D analysis.

The agreement of inelastic scattering rates in Fig.V-4 is the first reported agreement of inelastic rates for samples of different localization dimensionality. Similar agreement is seen for the other fully-1D wire, sample B. Before we try to understand this result, we should note that the mechanisms that contribute to the inelastic processes are elec-

tron-phonon scattering and electron-electron scattering (see Sec.IV-C.2). The discussion below compares the roles of these two mechanisms in wires and films.

Sec.II-F.2 describes the relevant considerations for electron-phonon scattering. The dimensional size scale for electron-phonon scattering is the characteristic phonon wavelength $\sim(726/T)\mathring{A}$ with T in K. At temperatures where electron-phonon scattering is dominant, both the films and the narrow wires are three-dimensional with respect to electron-phonon scattering.

At low temperatures, the electron-electron scattering rate begins to dominate. The details of the general considerations related to this mechanism are given in Sec. II-F.2 and II-F.3. The dimensionality for electron-electron scattering is decided by a different characteristic length from that of the electron-phonon scattering. The characteristic length for electron-electron scattering corresponding to an energy transfer of $\sim k_BT$ is $(\hbar D/k_BT)^{1/2}$. We initially thought Eq.(2.23a) to be the relevant theoretical result for electron-electron scattering, with a typical energy $\sim k_BT$. Hence we proposed[18,45,46] that the wires were also still 2D with respect to the electron-electron inelastic mechanism, since $W > (\hbar D/k_BT)^{1/2}$ in our experiments.

However, as was discussed in II-F.3, the relevant scattering mechanism for the phase relaxation is electron-electron scattering at small energies. The theoretical predications for this mechanism are Eq.(2.25) or (2.26) for the 2D and 1D cases respectively. The condition (2.26a) for the use of 1D scattering rate reduces to the following for sample A

$$W < (6/T^{1/2}) \text{ microns} \qquad (5.2)$$

with T in K. Since sample A is only 0.2 micron wide, it satisfies the

condition for one-dimensional electron-electron scattering very easily. For sample A, a comparison of the magnitudes of the τ_ε^{-1} at T=4K for the 2D and 1D cases [Eq.(2.25) and (2.26) respectively] reveals that the 1D rate is larger than the 2D rate by a factor of $\sim$5. This difference in the inelastic scattering rate is expected to result in a value of l_i that is $\sim$2 smaller than for the 2D film. Hence, we should have observed the one-dimensional electron-electron scattering mechanism. We apparently did not.

Due to the dominance of the electron-phonon scattering at high temperatures the temperature range we have in our experiments to observe the change in the dimensionality of the electron-electron scattering mechanism is limited (1.8K < T < 5K). We should note that Eq.(2.26) for 2D systems has been experimentally verified in 2D systems (see Sec.IV-C.2). But, Eq.(2.26) for 1D systems has not yet been verified, especially for its quantitative validity. Our results indicate that Eq.(2.26) could be overestimating the electron-electron scattering rate in 1D systems by a factor of $\sim$3 or more. In any case the agreement of the electron-phonon scattering rates at higher temperatures for the narrow wire and the film unambiguously confirm the one-dimensional behavior with respect to localization.

We discuss some observations on the experimental results in 1D silicon inversion layers in Chap VI.

V-D RESISTANCE AS A FUNCTION OF TEMPERATURE

Most previous experiments on narrow wires measured primarily the resistance change with temperature. For our samples, magnetoresistance data and the resulting τ_i values provide a more direct test of locali-

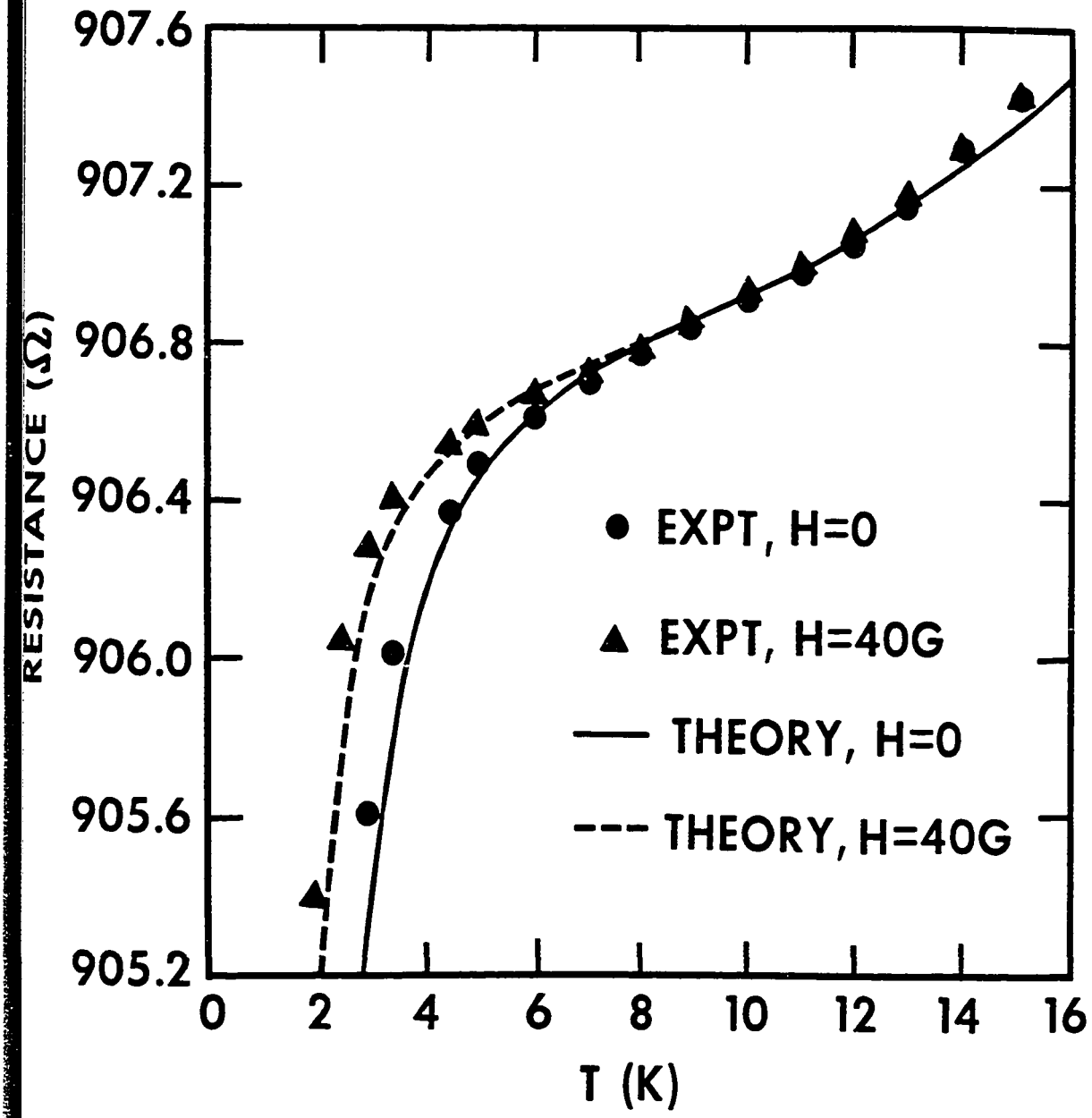

Fig.V-5 Resistance as a function of temperature for sample A. Theory curves were matched to the experimental data at 6K.

zation theory. Still, to verify the R(T) prediction we plot in Fig.V-5, R(T) for sample A.

Theoretical plots of R(T) are also given in Fig.V-5. We expect the localization and MT contributions to be one-dimensional [Eq.(2.10),(2.13) and (2.18)] upto 15K. The electron-phonon contribution to $\widetilde{\delta R}$ for the wires is well fitted by Eq.(4.9), similar to the case of thin films discussed in IV-D.1. As in the 2D case the electron-phonon contribution is independent of H.

The parameters for the theoretical curves, H_i and H_{so}, are taken from the 1D magnetoresistance studies. The values are not adjustable here. C_{ph} for the 2D and 1D cases agree within 5%. The quantitative agreement over the entire temperature range confirms the 1D theoretical prediction. The agreement of theory and experiment at low temperatures, where the MT term is dominant, confirms that l_i is the relevant length scale for the MT term.

V-E MIXED DIMENSIONAL SAMPLES

As noted in Sec.II-B, when the sample width is such that $l_2 < W < l_i$ we expect a mixed dimensional behavior. We have studied two samples (C and D) in this regime. We illustrate the behavior in terms of sample D.

V-E.1 Magnetoresistance

The magnetoresistance data for sample D, of width 0.4 micron, are shown in Fig.V-6. At high temperatures, 15K and 20K, the data can be satisfactorily fit to the 2D theory (see the discussions in IV-C.1) with reasonable, temperature-dependent values for H_i and a temperature-independent value of H_{so} = 18G. In contrast, for T< 12K, the experimental

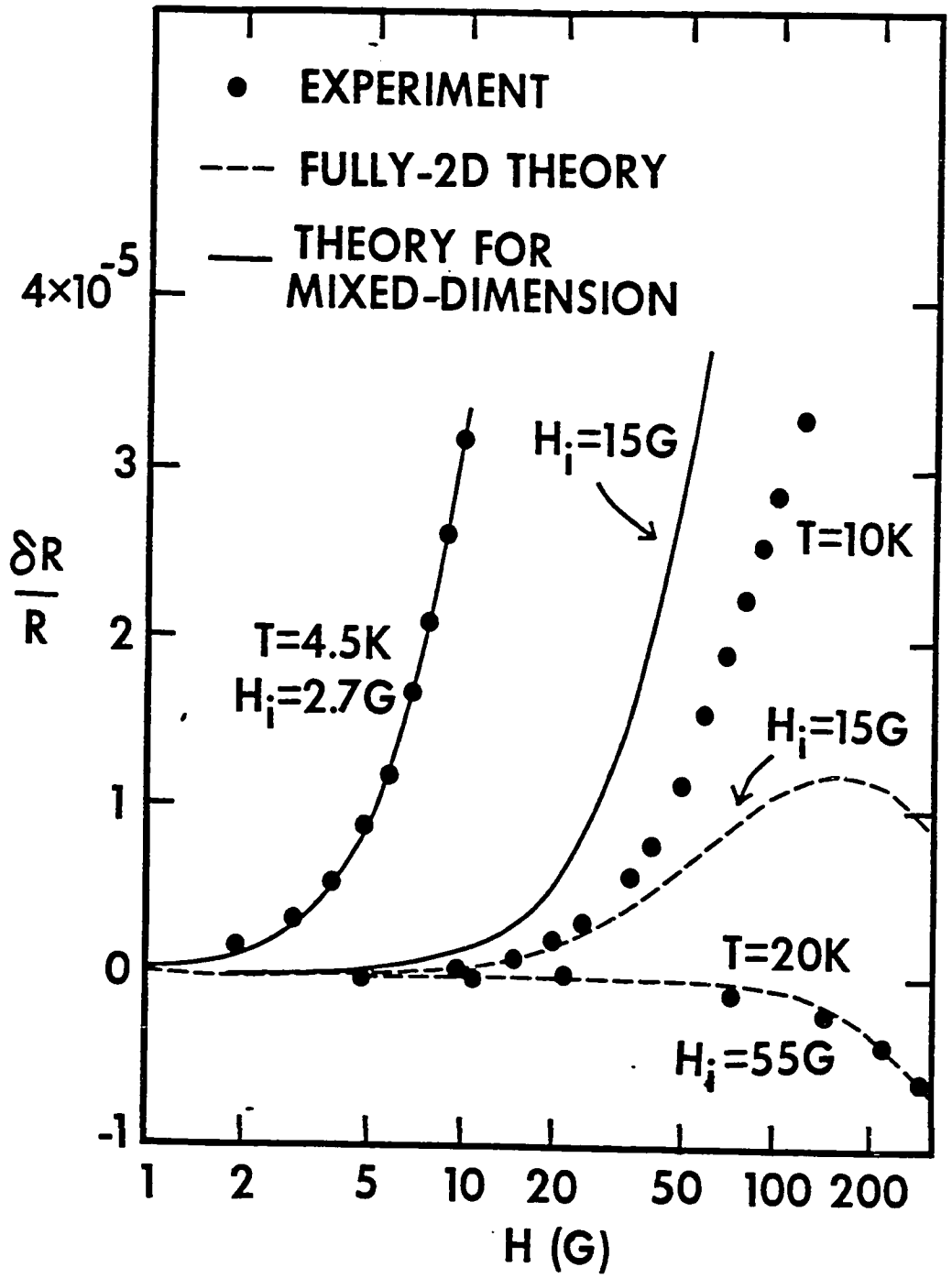

Fig.V-6 Magnetoresistance for sample D that showed mixed-dimensional behavior. At T=10K, neither the mixed-dimensional theory nor the fully-2D theory fit the data. H_{so} = 18G for all fits.

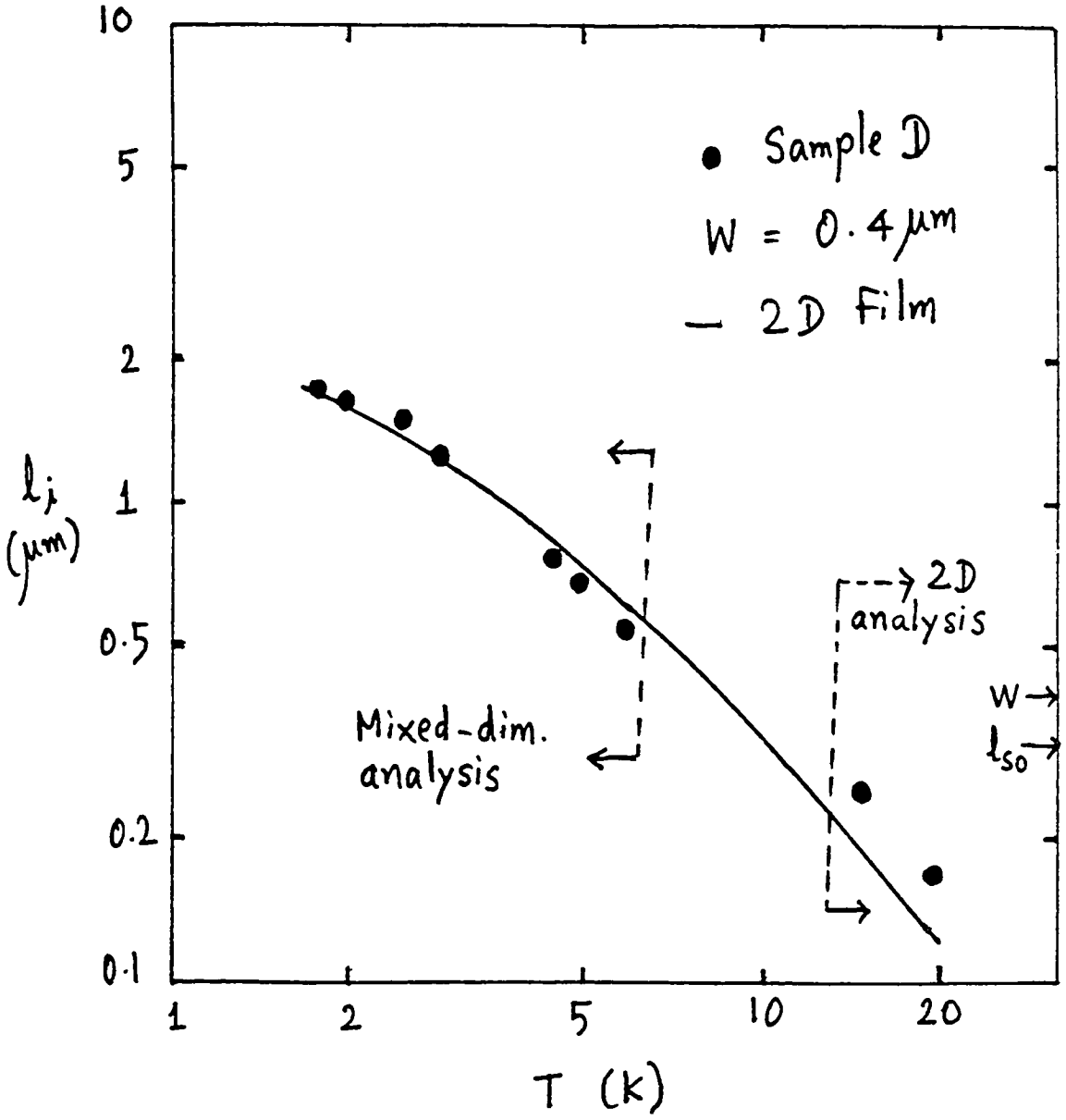

Fig.V-7 Inelastic diffusion length vs temperature for sample D. For T ≤6K, the localization behavior is mixed dimensional as $l_2 < W < l_i$. For T ≥ 15K , the behavior is that of a 2D film. In each temperature range appropriate theoretical analysis was used to extract values of l_i.

data cannot be fit satisfactorily to the 2D theory for any set of parameters H_i and H_{so}. When $T \sim 5K$ the behavior of the sample is well described (see Fig.V-6) by the magnetoresistance formula corresponding to the mixed-dimensional behavior [the sum of Eqs.(2.9),(2.14) and (2.18)], with the same H_{so} as at high temperatures. The fully-1D theory does not provide as good a fit. At the lowest temperatures ($T \sim 2K$), due to the dominance of MT fluctuations and the singlet part of the localization contribution, it is hard to tell the mixed-dimensional theory from the fully-1D theory in the fitting procedures. A non-superconducting material will be needed in order to make this distinction clear at the lowest temperatures.

For $H_{so} = 18G$, we obtain $l_{so} = (D \tau_{so})^{1/2} \sim 0.3$ microns. The inferred inelastic diffusion length for sample D is plotted as a function of temperature in Fig.V-7, along with those for the codeposited wide 2D film. The agreement of the $l_i(T)$ from the wire D with that of its codeposited film can be understood from our discussion in Sec.V-C. In addition for sample D, we note that at high temperatures $W > l_i$ and l_2 as appropriate for 2D behavior. At low temperatures $l_2 < W < l_i$ as expected for the mixed-dimensional behavior (See Fig.V-7). The behavior of Sample C is similar to that of Sample D regarding its mixed-dimensional behavior.

V-E.2 Location of the Dimensional Crossover

Experimentally we find that when $l_i > 1.3\ W$, the mixed-dimensional theory is applicable, and when $l_i < 0.5\ W$ the 2D theory is applicable. Thus, for the singlet and MT terms there is a crossover in dimensionality when $l_i \sim W$. This crossover of localization dimensionality is in accord with the original ideas of Thouless[3].

We had measured magnetoresistance of sample L45, a 2 micron wide wire fabricated by optical lithography, before we studied the submicron wires discussed in this chapter so far. The magnetoresistance data could be fitted to the 2D theory for $T > 6K$ consistent with the empirical condition $l_i < 0.5\ W$. At the lowest temperature at which magnetoresistance data were taken, $T \sim 2.5K$, neither the 2D theory nor the mixed-dimensional theory could describe the data satisfactorily, implying that $l_i(2.5K)$ was not long enough for the mixed-dimensional theory to be valid. This conclusion is consistent with our conclusions drawn from the narrower wires.

VI. COMPARISON TO OTHER WORK

VI-A TWO DIMENSIONAL STUDIES

Due to the vast number of studies in two dimensional systems, it is not possible to give a full account of the results in this chapter. We refer to a recent review of Bergmann[11] for a thorough summary of the conclusions from various experiments. The study of magnetoresistance at very low magnetic fields has proved crucial in separating the localization contribution from that due to electron-electron interaction effects. Such a separation is possible only when $H_i \ll H_{int}$. The experimental results from the studies of many two-dimensional systems (thin metal films and electron inversion layers in MOSFETs) are consistent with the existence of localization effects.

The inferred parameters from fits to experimental data (viz. inelastic scattering rate, spin orbit rate and magnetic scattering rate) provide the crucial test for the quantitative validity of the localization theory. Due to the large differences in properties of thin films made in various laboratories a consensus on the quantitative behavior of the scattering rates has not been possible[11] . Hence, the general question of the mechanisms responsible for phase destruction of the Cooperon does not seem to have a simple answer.

Among the various materials studied, aluminum films appear to display reasonably consistent behavior in the published literature . By and large this consistency is not obvious when one reads these literature reports due to the differences in the data analysis procedures. We discuss these experiments on aluminum in the next section.

VI-A.1 Other Studies on Aluminum Films

(i) Bruynseraede et al.[89] studied Al films of $R_\square$ ranging from $\sim$1.5 ohms to 60 ohms. The films were nominally 150Å thick. They used the localization theory in the zero spin-orbit scattering limit for the analysis. The inferred inelastic rates showed a linear dependence on T but were larger than the prediction of the electron-electron scattering result, Eq.(2.23a), by one order of magnitude. We subsequently reanalyzed their magnetoresistance data for sample A of Bruynseraede et al. (see Fig.IV-7 and Tables IV-1 and IV-2) and found their experimental data consistent with our data. Our own analysis of their data yielded inelastic times consistent with those in our films, and explained by electron-electron and electron-phonon scattering. Bruynseraede et al. now agree with our analysis and conclusions on their films[89].

(ii) The work of Gordon et al.[22,82] is an interesting complement to the work reported in this thesis. They initially studied granular, high resistivity films, with $\ell \sim 15$ Å. They fit the magnetoresistance data to the complete theoretical form and found the inelastic rate to be due to a combination of electron-electron scattering and electron-phonon scattering as was found in this work. In their original analyses they concluded that their electron-phonon mechanism showed $\tau_{ep}^{-1} = A_4 T^4$ for films with $\ell < 15$Å and $\tau_{ep}^{-1} = A_3 T^3$ for a film with $\ell = 46$ Å. They have recently studied cleaner films (comparable to ours) and also have reanalyzed their original data[86]. Gordon et al. have concluded that the form $\tau_{ep}^{-1} = A_3 T^3$ for electron-phonon scattering rate describes the experimental data well for all their samples. Their experiments spanned a wide range of $R_\square$ ($\sim$2 ohms to $\sim$200 ohms) and thickness (d$\sim$70Å to 200Å). The coefficient A_3 appeared to increase from our value of $\sim 1.5 \times 10^7$ to $\sim 3.5 \times 10^7$

with increasing resistivity. Their earlier extraction of an electron-phonon rate $\propto T^4$ was due to the relatively small contribution of electron-phonon scattering in the high resistance films with $R_\square > 50$ ohms.

For many films of Gordon et al. τ / τ_{so} was $\sim 1 \times 10^{-4}$ in reasonable agreement with our result of 2×10^{-4} for the ratio (see Sec. IV-C.3 and Fig.IV-9). There were a few samples of Gordon et al. which indicated a value for τ / τ_{so} as low as 0.2×10^{-4} indicating the possibility of a difference in the nature of spin-orbit scattering in those films. No systematic trend is indicated by their samples for the variation of the ratio τ / τ_{so}. However, based on their work, we conclude that all our conclusions on the inelastic scattering rate are valid for films whose resistivity spans two orders of magnitude.

Gordon et al.[22] also studied magnetoresistance very close to T_c (including the Aslamasov-Larkin term in the analysis for the magnetoresistance). Due to the increased probability for the pairing of two electrons to form a superconducting fluctuation, a divergent phase breaking rate was expected close to T_c from theory[22]. Through a proper subtraction of the inelastic scattering rate due to electron-phonon and electron-electron mechanisms, their experiments quantitatively confirmed the existence of an additional phase breaking mechanism due to electron pairing close to T_c.

(iii) Gershenson et.al.[23] reported measurements on two Al films with $R_\square = 20$ ohms and 112 ohms. The films were ~ 50 Å thick. They did the analysis of magnetoresistance data in the strong spin-orbit limit in the low temperature regime and in the zero spin-orbit scattering limit in the high temperature regime. Such an analysis is questionable in general; but at very low temperatures ($T \sim 3K$) the strong spin-orbit scattering

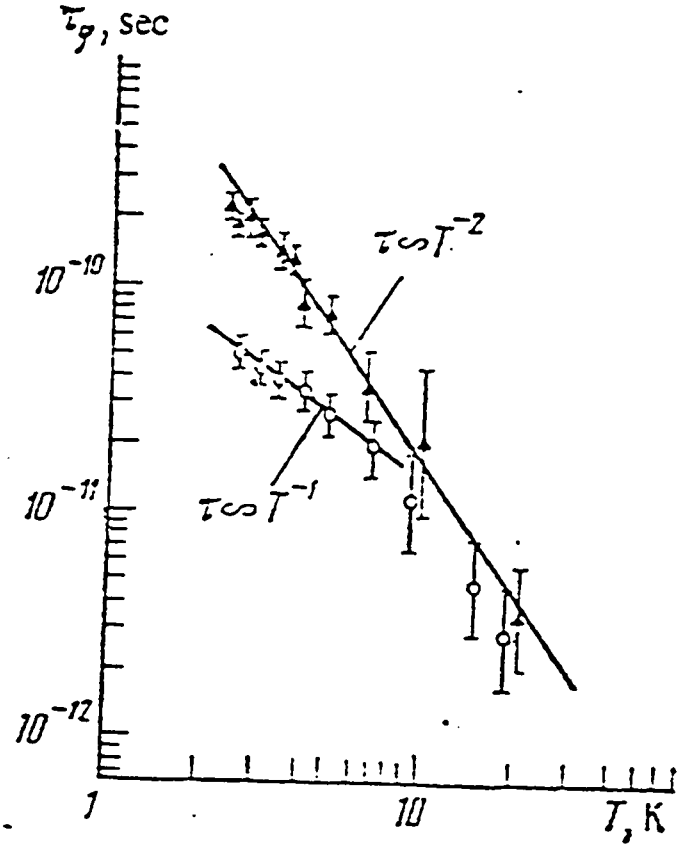

Fig.VI-1 Inelastic times vs temperature inferred by Gershenson et al.(Ref.23). The solid triangles correspond to the sample with $R_\square$ =20 ohms and open circles correspond to the high resistance sample with $R_\square$ = 112 ohms.

limit is satisfactory (see Sec.IV-C.1) for inferring reasonable τ_i. Thus, we can use the τ_i values of Gershenson et al at low temperatures without much error. But the high temperature fits are quite sensitive to the choice of τ_{so}, since typically even at 20K the τ_i is not much shorter than τ_{so}.

Fig.VI-1 shows the inferred inelastic rates derived by Gershenson et al. for their two samples. We have already noted that their method of analysis was not satisfactory. They found that the low resistance film showed $\tau_i^{-1} \propto T^2$ behavior in the entire temperature range. The high resistance film showed $\tau_i^{-1} \propto T$ at low temperatures and $\tau_i^{-1} \propto T^2$ at high temperatures.

First we examine the high resistance (112 ohm) sample. It is clear from Fig.VI-1 that for this sample the mechanism with $\tau_i^{-1} \propto T$ dominates at low temperatures. The authors claimed that the magnitude from Eq.(2.25) was larger than the experimentally observed rate by 'several times'. We disagree with this conclusion. An evaluation of Eq.(2.25) for their sample yields

$$\tau_\varepsilon \sim (2.6/T)\times 10^{-10} \text{ sec}$$

At T=3 K, we calculate $\tau_\varepsilon \sim 85$ pS compared to ~ 45 pS observed experimentally. This agreement is within a factor of ~ 2 (similar to ours). At high temperatures the finite spin-orbit scattering rate has to be included for a satisfactory analysis of magnetoresistance data. Inclusion of finite spin-orbit rate in the fitting procedure will decrease the value of τ_i required to fit the data. Hence, there is a good possibility that τ_i will decrease faster the T^{-2} at high temperatures if spin-orbit scattering is included in the analysis. It is not clear if such a thin film ($d \sim 35\text{Å}$) should behave similarly to our samples, discussed in

Chapter IV. In any case, one needs a more thorough analysis of the data to address this issue. Unfortunately, we have not reanalyzed the data of Gershenson et al. ourselves.

For the sample with $R_\square$ = 20 ohms [as expected from Eq.(2.25)] τ_ε^{-1} is smaller. However, based on the results discussed in Chapter IV, we expect a significant electron-phonon contribution to the inelastic rate. As determined by Gordon et al.[86], the coefficient A_3 for the electron-phonon scattering has a tendency to increase with decreasing elastic mean free path. An evaluation of τ_i^{-1} [Eq.(4.6) using Eq.(2.25) and τ_{ep}^{-1} = $2.0 \times 10^7 T^3$] at 3K yields 0.4 nS compared to 0.2 nS observed experimentally. Thus we see the apparent behavior of $\tau_i^{-1} \propto T^2$ can very easily be explained as due to a combination of electron-electron and electron-phonon scattering rates of the form of Eq.(4.6). With this, their data would be consistent with the results of other researchers. The only reason the data of Gershenson et al. appear to behave differently from ours is because their analysis of the magnetoresistance data at high temperatures is incorrect. This is because of their assumption that $\tau_{so}^{-1} \sim 0$.

(iv) Bergmann[97] studied a quench condensed Al film of $R_\square$ = 117 ohms and thickness 90Å. He fit the magnetoresistance data to the complete theory including spin-orbit scattering. He inferred a behavior for $\tau_i^{-1} \propto T^{2.13}$ in the temperature range 4.5K to 20K. Bergmann contended that quenched condensed films were intrinsically different from pure Al or granular Al. In spite of all the differences in the preparation of the samples, the basic film properties (T_c, ρ_c , D) and even the inferred spin-orbit scattering rate are close to those of the granular film sample C of Gordon et al[82,86]. An evaluation of τ_i following the inferred

coefficients from the work of Gordon et al. can likely explain Bergmann's data in quantitative terms. It is also likely that if Bergmann had obtained the experimental data over a wider temperature range, any deviation of the data for τ_i^{-1} from a single power law (T^n) would have been more obvious. τ_i at the lowest temperature studied, $T \sim 4.5K$ (see Fig.10 of Ref.97) deviates from the value one would extrapolate from the higher temperature data by assuming $\tau_i^{-1} \propto T^{2.13}$!. This indicates a slower temperature dependence than $\tau_i^{-1} \propto T^{2.13}$, which is consistent with our findings and those of Gordon[86]. The value for τ / τ_{so} for Bergmann's film was 0.13×10^{-4} (see Fig.IV-9).

VI-B THREE DIMENSIONAL STUDIES OF ALUMINUM

Mui et al.[107] reported magnetoresistance measurements on 1micron thick granular aluminum films with resistivities in the range ~300 micro-ohm-cm to 6000 microohmcm. The film morphology is that of Al grains ~30Å diameter isolated from adjacent grains by aluminum oxide. The analysis was done in terms of the three-dimensional theory, comprising terms from localization, MT fluctuations and the orbital contribution of the electron-electron interaction. The inferred inelastic rate appeared to change from $\tau_i^{-1} \propto T^2$ in the case of ~300 microohmcm sample to $\tau_i^{-1} \propto T$ for the ~6000 micro-ohm-cm sample. The magnitude of the inelastic scattering rate appeared to be comparable to the 2-D case.

It is not clear as to how to understand this behavior. These samples can be shown to be in the three dimensional limit for the electron-electron scattering with small energy transfers[49,15]. In such a case, electron-electron scattering with energy transfers of $\sim k_B T$ are expected to dominate[15,49], resulting in $\tau_{ee}^{-1} \propto T^{3/2}$ behavior. It is

also likely that electron-phonon scattering (in their lower resistivity films) is not negligible so that

$$\tau_i^{-1} = \tau_{ee}^{-1} + \tau_{ep}^{-1}$$

The nature of the electron-phonon scattering in such granular systems is unknown. The samples with resistivity ~1000 microohm-cm may indeed have have an inelastic mechanism corresponding to two-level tunneling states with a rate $\tau_{TLS}^{-1} \propto T$.

The ratio τ_i / τ_{so} inferred by Mui et al. was smaller by almost three orders of magnitude when compared to the ratio for our films. We suggest that this difference in behavior may be traceable to the existence of weak tunneling between grains that decides the resistivity for granular Al. The mechanism(s) behind spin-orbit scattering in granular Al must be different from that in 'pure' Al, where electron transport and apparently spin-orbit scattering are both determined by impurity scattering.

VI-C ONE DIMENSIONAL STUDIES

VI-C.1 Au-Pd Wires

The first experiments testing the predictions of Thouless were carried out by Giordano et al.[53]. They made narrow wires of $Au_{60}Pd_{40}$ with $(Area)^{1/2} \sim 300\text{Å}$ to 2000Å using a novel step-edge shadowing technique. The low temperature resistivity of the films used ranged from 100 microohm-cm to 400 microchm-cm. An increase in resistance with decreasing temperature was observed; the samples of smaller cross sectional area showed proportionally larger effects such that $\tilde{\delta}R/R \propto A^{-1}$, in agreement with the theoretical prediction for one-dimensional behavior. The interpretation of the R(T) data was in terms of Thouless' 1D localization

prediction[3] [Eq.(2.13) with H= 0 and $\tau_{so}^{-1} = 0$]. Fitting the data to this H=0 prediction yielded an inelastic scattering rate

$$\tau_i^{-1} = 9 \times 10^{12} \, (T/\rho_o)$$

with ρ_o the resistivity in microohm-cm. This inelastic rate far exceeds that due to the clean-limit electron-phonon scattering which, of course, does not depend on ρ_o. The dependence $\tau_i \propto \rho_o$ is also hard to understand also within any dirty-limit model of disorder related inelastic scattering. For disorder induced scattering , we would expect τ_i^{-1} to increase with ρ_o. No satisfactory theoretical explanation of the inelastic rate inferred by Giordano et al. has emerged to date. We note that these wires had $k_F l \gtrsim 1$ (due to very short mean free paths).

Since those experiments on Au-Pd wires were performed, the theoretical understanding of the effects of spin-orbit scattering and of the magnetoresistance have advanced significantly. Recent magnetoresistance measurements by McGinnes[98] on 2D Au-Pd films infer an inelastic rate of 2.5×10^{10} at 2K. The inelastic rate increased faster than T between 2K and 5K. These results are for a film of ρ_o = 112 microohm-cm and d =145Å. It was also found that $\tau_{so}^{-1} \sim 5 \times 10^{12} \gg \tau_i^{-1}$, so that for this Au-Pd alloy, $l_{so} \sim 80$Å.

These quantitative results of McGinnes for the scattering rates in a 2D Au-Pd film call into question the original analysis of the results for Au-Pd wires. Assuming that the 2D value of τ_{so} applies also for the wires, the narrowest wires of Giordano et al. could only be in the limit $l_{so} < l_i$ and $l_{so} \ll (\text{Area})^{1/2}$. The predictions of Thouless were for the weak spin-orbit scattering case and hence cannot be applied. In fact, considering the scattering parameters for the 2D films, if the only contribution to R(T) were from localization, the resistance for the

wires should actually decrease as T is reduced. This was definitely not the experimental result. If significant magnetic scattering was present, the localization effects would be decreased in magnitude and the temperature dependence of the localization contribution 'flattened'. In any case we do not know any plausible set of parameters τ_i, τ_{so}, and τ_s (magnetic) which could give the observed rise of resistance from localization effects.

White et al.[99] suggested that the resistance rise observed in the Au-Pd wires could be due to electron-electron interaction effects, and not necessarily due to localization effects. The discussion in the last paragraph can provide a plausible explanation for the absence of localization effects as due to spin-orbit and magnetic scattering. We find the identification of electron-electron interaction effects as the cause of the observed resistance rise to be plausible. The absence of appreciable magnetoresistance reported by Giordano et al. is consistent with such an interpretation.

The data of Giordano et al. shows[100] one curious dependence that could not be simply explained by electron-electron interaction effects[8]. It was the behavior of $\tilde{\delta}_{R/R}$ proportional to ρ_o, whereas the theoretical prediction of the interaction theory is $\tilde{\delta}_{R/R} \propto \rho_o^{1/2}$. It is possible that for these very dirty films, for which $k_F \ell \sim 1$, we need a modified theory for the resistance change. Such a theory might explain the experimental result for the resistivity dependence. Alternatively, it is possible that Giordano et al. were observing some other effect, and not localization or interaction effects. This remains for future study.

VI-C.2 W-Re Wires

Chaudhari et al.[101] studied narrow W-Re wires of width 700Å to

5000Å, fabricated by electron-beam lithography. The resistivity was ~400 microohm-cm and the films were 50 Å thick. The inelastic scattering rate was determined from the resistance rise [using Eq.(2.13) with H= 0 and $\tau_{so}^{-1} = 0$]. Measurements on superconducting phase-slip centers in 250Å wide wires were also performed, to obtain an independent measure of τ_i^{-1}. The inelastic rate from the localization experiment was in reasonable agreement with $\tau_i^{-1}(T_c)$ from the phase-slip experiments. However, a more recent experiment on 2D W-Re films[102] has concluded that the inelastic scattering length l_i was less than 200Å for T< 5K, leaving the 1D behavior of W-Re wires in question. That study also found that spin-orbit scattering to be strong in W-Re, so that the use of Thouless's theory[3] without spin-orbit scattering was not correct. White et al.[99] reanalysed the data for W-Re wires and found that the resistance rise was also consistent with the electron-electron interaction theory. One should note that the theory for including superconducting fluctuations in the analysis was not available when these experiments were done.

VI-C.3 Copper Wires

White et al.[99] studied <u>clean</u> copper wires ($\rho_0 \sim$ 3 microohm-cm) with cross-sectional dimensions as small as 200Å x 200 Å. From a careful analysis of the observed resistance rise at low temperatures, they concluded that electron-electron interactions could explain the observed R(T). This interpretation assumes that localization effects are small.

The apparent absence of localization effects in the clean copper wires of White et al. may have been due to magnetic scattering, which flattens the temperature dependence of $\tilde{\delta}_{R^{Loc}}$. In fact, the magnetoresistance studies of 2D Cu films by Abraham and Rosenbaum[103] did find a relatively short magnetic scattering time, $\tau_s \sim$ 65 pS, though it did

depend on film preparation techniques. Furthermore, the copper wires of White et al. were in the 1D limit for the electron-electron scattering, corresponding to Eq.(2.26). Since $\tau_\varepsilon^{-1} \propto (Wd)^{2/3}$, the 1D inelastic scattering rate would be large, so that the change in resistance $\tilde{\xi}_{R^{loc}}$ could be quite small. In addition, Abraham and Rosenbaum found a relatively short τ_{so} ($\sim$5 pS) indicating the importance of its inclusion in the analysis of Cu wires.

VI-C.4 Drawn Platinum Wires

Sacharoff et al.[104] prepared platinum wires of $\sim$1000Å diameter by a mechanical drawing process. They found an unusually large fractional change of resistance with temperature and also an anomalous positive magnetoresistance. These experimental data could not be explained by 1D localization theory or 1D electron-electron interaction theory as was noted by the authors. They found good agreement with the 3-D localization theory. A mechanism due to the unusually large disorder introduced by the drawing process was suggested as the reason for the large inelastic rate observed.

VI-C.5 Bismuth Whiskers

In a study by Overcash et al.[105], single crystal whiskers of bismuth less than 2000Å in diameter were made by stress accelerated growth. The elastic mean free path was estimated to be boundary limited. Resistance measurements from 20K down to 0.5K showed only a decrease in resistance with decreasing temperature. The authors concluded that there was no clear evidence for 1D localization. We conjecture that this apparently null result may be a case of weak localization, but where the singlet term in Eq.(2.13) is significant. The authors esimated the inelastic diffusion length to be $\sim$100microns, and given the large Z of Bi, τ_{so} is

likely much shorter. A detailed study of magnetoresistance on these samples at very small fields would be of significant interest.

VI-C.6 MOSFETs

Wheeler et al.[106] studied a narrow wire formed in silicon inversion layers of width $\sim$0.4 micron and compared its behavior to a simultaneously prepared wide 2-D inversion layer on the same substrate. The magnetoresistance studies showed clearly the presence of localization in these experiments. The analysis of data in the wide MOSFETs showed $\tau_i^{-1} \propto T$ in agreement with the then available Eq.(2.23a), but with an experimental magnitude for the rate $\sim$5 times smaller than that from Eq.(2.23a). A comparison to the more recent theoretical prediction Eq.(2.25) now gives excellent agreement between theory and experiment.

In the narrow inversion layer the inelastic electron scattering mechanism appeared to change as the localization behavior changed from 2D to 1D at low temperatures. The requirement for the 1D behavior as given by Eq.(2.26a) yields for a MOSFET with $R_\square$ = 200 ohms and D= 140 cm^2/sec,

$$W < (0.7/T^{1/2}) \text{ micron}$$

For a MOSFET width of 0.4 micron this would imply that 1D behavior of the mechanism should occur below 3K. This was consistent with the observed behavior. However, the magnitude of the experimentally inferred ℓ_i at 0.5K was $\sim$0.7 microns compared to the theoretical estimate [Eq.(2.26)] of $\ell_i \sim$ 1.2 micron. This is against the trend observed in our work discussed in V-C.3 where we found that the theory predicted a smaller value for ℓ_i than was found from the experimental data. We do not know the reason for the discrepancy. One possible source of discrepancy is that the theoretical equation [Eq.(3) of reference 106] used by Wheeler et al. had an additional factor of 2 in the denominator. This would

cancel with the assumed degeneracy of 2 for the [100] silicon inversion layer, making the inversion layer effectively non-degenerate in the analysis. We also note that in contrast to the results reported in this thesis (see Fig.V-4), Wheeler et al found that ℓ_i was 2x smaller in the narrow channel compared to the wide channel at even the highest temperature measured, T = 4 K. Based on the results from our work (Fig.V-4), both the narrow and wide channels would be expected to have the same inelastic scattering length. Thus, the quantitative situation with respect to localization effects is fairly well understood for wide and narrow MOSFETs, as it also is for metal films and wires. The understanding of the inelastic mechanisms in the narrow MOSFETs is apparently not as complete as for metal wires.

VII. SUMMARY AND CONCLUSIONS

The primary objective of this thesis has been to verify the existence of the quantum correction to resistivity due to weak localization of electrons in Al films. In this chapter we summarize the important developments in our understanding of electron transport in Al films. We discuss our results in two parts viz. thin films and narrow wires.

VII-A THIN FILMS

VII-A.1 General Comments

From studies in various two-dimensional systems there is little doubt today that the phenomenon of electron localization exists in disordered metallic systems. Our results in aluminum films add strong quantitative evidence to support this contention. The existence of superconducting fluctuations above the transition temperature of Al presents an interesting (and in a way useful) complication to the data analysis. The theory of Maki-Thompson fluctuations (recently rederived by Larkin for $T \gg T_c$) has made the analysis of experimental data possible in the case of superconductors. The identification[3] of inelastic scattering as the mechanism responsible for non-zero conductivity at $T \neq 0$ was crucial in the development of the concept of localization. The same mechanism, inelastic scattering, prevents the excess conductivity due to Maki-Thompson fluctuations from diverging at $T > T_c$. This realization[23,108] has been important in our understanding of superconductors.

The study of magnetoresistance has been very helpful for a clear separation of weak localization and MT fluctuations from the other quan-

tum effects. In particular, it avoids the uncertainty in the analysis of R(T) data for inferring the various electron scattering parameters (τ_i, τ_{so}, τ_s). These parameters are of enormous importance in electron transport in disordered metallic systems.

VII-A.2 Inelastic Mechanisms

A key contribution of this work is in the understanding of the inelastic mechanisms that destroy the phase coherence essential for localization. From a detailed study of magnetoresistance data we have identified the inelastic mechanisms as electron-phonon scattering and electron-electron scattering such that

$$\tau_i^{-1} = \tau_\varepsilon^{-1} + \tau_{ep}^{-1}$$

The electron-phonon scattering rate τ_{ep}^{-1} has been determined in our films to be

$$\tau_{ep}^{-1} \sim 1.5 \times 10^7 \, T^3$$

essentially independent of film resistivity in the range 1.5 microohm-cm to 8 microohm-cm. This result for τ_{ep}^{-1} agrees within a factor of two with the theory of Lawrence and Meador for electron-phonon scattering in Al. To be exact, the experimental rate is larger than that predicted by the theory by $\sim$1.6 .

We find that the experimentally inferred rate τ_ε^{-1} is given by

$$\tau_\varepsilon^{-1} \sim 8 \times 10^7 \, R_\square \, T \, .$$

This result agrees within a factor of two with the prediction of the theory of electron-electron scattering at small energy tranfers proposed by Altshuler et al. for 2D systems . Here also, the theory predicts a rate that is $\sim$2 times smaller than the experimental result.

In some metal films with resistivity of $\sim$100 microohm-cm (see for example the work by Bergmann[11] on Mg), $\tau_i^{-1} \propto T^2$ behavior has been

observed. This inelastic rate (proportional to T^2) is different from what we have seen in our much cleaner samples. Bergmann has noted, however, that the observed inelastic rate is too large to be explained by current theories of electron-phonon scattering[11,34].

VII-A.3 Comparison to Superconducting Experiments

The inelastic scattering rates inferred from our localization experiments on higher resistance ($R_\square > 1$ ohm) films are in satisfactory agreement with those from experiments done in the superconducting state, such as superconducting quasiparticle charge imbalance, microwave enhancement of the critical current, and superconducting energy gap relaxation.

Based on our current understanding of electron-electron scattering in localization and superconductivity experiments, the agreement between the localization and superconductivity experiments raises an important issue. Localization experiments measure the phase relaxation rate τ_ε^{-1} of the Cooperon. It is the electron-electron quasiparticle scattering rate τ_{ee}^{-1} which apparently enters the superconductivity experiments[57]. In principle, the Cooperon rate can differ from this quasiparticle rate. Hence the theoretical question arises as to whether the experimental agreement we find between the two rates is coincidental. We do not have an answer to the theoretical question. In any case, our experiments clearly indicate that the rates in the localization and superconducting experiments are not very different (see Fig.IV-15).

In cleaner films ($R_\square < 1$ ohm), the inferred inelastic scattering rate from the superconducting experiments (see Fig.IV-15) is larger than the electron-phonon scattering rate by a factor of $\sim$5. It is likely that

this excess scattering can be explained by clean-limit electron-electron scattering .

VII-A.4 Spin-Orbit Scattering

Localization experiments allow a direct extraction of τ_{so}, which is difficult in almost all other transport measurements. Our experiments show a clear indication of scaling of the spin-orbit scattering time with elastic scattering time, in agreement with the theory of Abrikosov and Gorkov (see Sec.II-G). We find

$$\tau / \tau_{so} \approx 2 \times 10^{-4}$$

in our samples. Since the film thickness is larger than the elastic mean free path it is reasonable to expect that the spin-orbit scattering is due to impurities in the bulk of the film and not due to boundary scattering. A simple estimation proposed by Abrikosov and Gorkov, with oxygen as the impurity, does not explain the data. However, if the elastic scattering is assumed to be due to vacancies in bulk Al, one can explain the τ / τ_{so} ratio using the theory of Abrikosov and Gorkov. Identification of the chemical impurity species responsible for spin-orbit scattering is still somewhat ambiguous, since oxygen incorporation had been thought to cause the resistivity increase for slowly-deposited films. We need a more controlled experiment in order to address this issue quantitatively and in detail.

VII-A.5 R(T) Behavior in Films

The experimental R(T) behavior in our films is dominated by electron-phonon scattering at high temperatures ($T \gtrsim 8K$) and by Maki-Thompson fluctuations at low temperatures ($T < 4K$). The localization contribution to the resistance is comparable to the contributions from MT fluctuations and electron-phonon scattering only in a small interval in temperature

4K < T < 8K. We find the theory for MT fluctuations in 2D systems explains the experimental data well. The electron-phonon scattering contribution to the resistance is proportional to T^3, indicating the importance of umklapp scattering at these low temperatures. The magnitude of the electron-phonon contribution to the resistance agrees very well with that expected from the inelastic scattering rate inferred from magnetoresistance data.

VII-A.6 Comparison of Parallel and Perpendicular Field Results

From our study, we conclude that the theoretical calculations satisfactorily explain the experimental data for magnetoresistance in the parallel field orientation. The large anisotropy expected from the localization theory was indeed observed. Excellent fits to experimental data were obtained with inferred scattering parameters that differed by only a factor of $\sim$1.5 for the two field orientations.

VII-A.7 Comments on Other Studies of Aluminum

We have shown in detail how the experiments on Al of considerably different film quality done in various laboratories of the world do agree with each other, and support our interpretation of the inelastic scattering rate. The mechanism(s) causing spin-orbit scattering in granular films does appear to differ from that in clean films.

VII-B NARROW WIRES

VII-B.1 Localization Dimensionality: Theory

According to the original 1D theory of Thouless (which is true only in the limit of negligible spin-orbit scattering), the localization dimensionality of a sample is decided by the inelastic scattering length l_i. Spin-orbit scattering plays an important role in real experimental

samples. To account for the effects of spin-orbit scattering, we have introduced another length scale ℓ_2 for localization experiments. Only when

$$W,d < \ell_i, \ell_2$$

can the sample be considered to be in the fully-one-dimensional limit for its localization behavior. When

$$d < \ell_i, \ell_2 \quad \text{and} \quad \ell_2 < W < \ell_i$$

the sample will show a mixed-dimensional (1D + 2D) behavior. We have extended the existing localization theory to include spin-orbit scattering, and given theoretical predictions for the change in resistance in the fully-one-dimensional and mixed-dimensional regimes. Our experiments confirm these theoretical predictions.

VII-B.2 One-Dimensional Maki-Thompson Superconducting Fluctuations: Theory

We have proposed (see Sec. II-D.4) that the dimensionality for MT fluctuations is decided by ℓ_i. The sample behavior becomes one-dimensional for a sample with $W,d < \ell_i$. Thus, in the case of samples that are either fully-one-dimensional or mixed-dimensional in their localization behavior, the MT contribution is <u>one-dimensional</u>.

VII-B.3 One-Dimensional Behavior: Experiment

Our experiments on two samples of width $\sim$0.2 micron have verified our predictions of the theory of one-dimensional localization that includes spin-orbit scattering and superconducting fluctuations. The samples showed one-dimensional behavior for magnetoresistance up to relatively high temperatures ($>$15 K).

The values of ℓ_i and ℓ_{so} inferred from the fully 1D analysis, were both larger than the sample width, confirming the use of the fully-1D

theory. In addition, the inelastic scattering length inferred from the wires agreed well with that from a codeposited wide film of similar material properties. The wide film data were analyzed independently using the 2D theory. This illustrates the fact that the inelastic scattering mechanism can be the same even if localization dimensionalities are different. In fact, for $T > 5K$, the dominant inelastic scattering mechanism for both wires and films is three-dimensional electron-phonon scattering.

At the lowest temperatures measured, the dominant inelastic scattering mechanism was electron-electron scattering. This was also found in wide films. According to the theory of Altshuler et al., our samples were one dimensional with respect to the electron-electron scattering mechanism. But the values of ℓ_i estimated using this theory are at least a factor of ~ 2 smaller than the experimentally inferred values in the temperature range 1.8 to 4.5K. Their theory appears to be overestimating τ_ε^{-1} by a factor of ~ 5

VII-B.4 Mixed-Dimensional Behavior

Two of the wires we studied of $W \sim 0.5$ micron showed mixed-dimensional behavior at low temperatures ($T < 7$ K). These samples fitted the 2D theory for magnetoresistance at $T \geq 15$ K.

At $T \sim 6$K it was clear from the fits to magnetoresistance data that the mixed-dimensional result describes the experimental data better than either the fully-1D or fully-2D theory. At low temperatures (< 5K) in our aluminum samples, it was hard to distinguish the fully-1D theory from the mixed-dimensional theory for the localization term due to the large magnetoresistance contribution from superconducting fluctuations. A non-

superconducting material with reasonably long inelastic lengths may be more suitable for this purpose.

The inferred inelastic scattering lengths from the mixed-dimensional samples agreed with those inferred from the codeposted wide films. Experimentally, when $\ell_i > 1.3\ W$, the mixed-dimensional theory is applicable, and when $\ell_i < 0.5\ W$ the 2D theory is applicable. Thus when $\ell_i \sim W$, there is a crossover in localization dimensionality in agreement with the original ideas of Thouless.

VII-B.5 One-Dimensional Maki-Thompson Fluctuations: Experiment

A significant consequence of the choice of Al as our sample was that we could verify the Maki-Thompson contribution for 1D superconducting fluctuations. The theoretical belief that ℓ_i decides the length scale for MT term is verified by our experimental results. This identification is quite unambiguous, since the one-dimensional fluctuations are significantly larger than the two-dimensional fluctuations. This result lends a new credibility to our understanding of both localization and superconductivity.

VII-B.6 Comments on Other Studies on Narrow Metal Wires

We have reanlyzed the previous experiments done on narrow metal wires of materials other than Al, and come to the following conclusions: (i) In the case of Au-Pd and W-Re alloy wires, large spin-orbit scattering and/or magnetic scattering rates could have produced localization effects that are much smaller than the original Thouless' prediction for H=0 and $\tau_{so}^{-1} = \tau_s^{-1} = 0$. The temperature dependence of the resistance was likely due to electron-electron interaction effects. (ii) In Cu wires the observed resistance rise was also due to interaction effects. The localization contribution could have been small due to magnetic

scattering and/or due to a large 1D electron-electron inelastic scattering rate. (iii) For the drawn Pt wires the observed magnetoresistance was not due to 1D localization effects. (iv) In the case of Bi whiskers, it is possible that the observed decrease in resistance was due to localization in the strong spin-orbit scattering limit. (v) In the case of the silicon inversion layers in MOSFETs, there was evidence for 1D localization but some quantitative discrepancies exist on the inferred scattering rates. Without systematic magnetoresistance data for (i), (ii), and (iv) further interpretation of these data is difficult.

In conclusion, we have demonstrated experimentally the existence of electron localization in Al films in the presence of superconducting fluctuations. Our experiments on 2D films have yielded understandable inelastic scattering rates. Furthermore, we have also shown that the localization behavior in Al observed in the experiments of other researchers is also consistent with our results. In the case of 1D systems, in contrast to the previous experiments, our experimental results show the first clear confirmation of the localization theory, when the theory is generalized to include spin-orbit scattering. The agreement of the inferred scattering parameters for the narrow wires and wide films further confirms the theoretical model of localization in 1D and 2D systems. We have shown clearly that a consistent interpretation of the experimental data in two-and one- dimensional systems for localization behavior is now possible.

APPENDIX A

Calculation of the Localization Contribution for Thin Films in Parallel Fields, and Limitations

Here we describe the similarities in the calculation of the Cooperon amplitude C(r,r') and that of the Ginzburg-Landau (GL) order parameter $\bar{\Psi}(r)$ in superconductivity. We briefly outline the existing theoretical calculations on the nucleation of superconductivity in a slab in a parallel field. We then use this theory to estimate the range of validity of the parallel field magnetoresistance formula due to localization in thin films.

A-1 Calculation for the Nucleation of Superconductivity in A Slab

An excellent discussion of this topic can be found in in Ref.109. We want to determine the maximum parallel magnetic field applicable to a superconducting slab, below which the superconducting order parameter $\bar{\Psi}(r)$ is not zero. Since the order parameter is small in this regime, linearization of the G-L equation is justified; the linearized equation is

$$\frac{\hbar^2}{2m}\left[-i\nabla - \frac{2e}{\hbar c}\bar{A}\right]^2 \Psi + \alpha \Psi = 0$$

with the boundary condition

$$\left[-i\nabla - \frac{2e}{\hbar c}\bar{A}\right]_n \Psi = 0$$

for the component normal to the surface of the superconductor.

To facilitate a direct comparison to the eigenvalue equation for the Cooperon operator (see below) we rewrite the above equation as

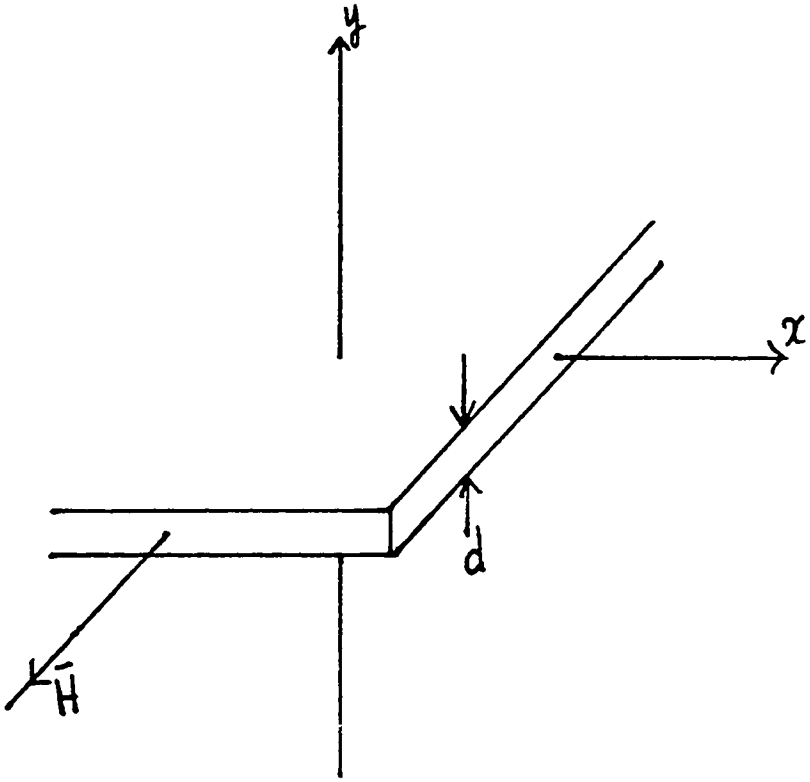

Fig.A-1 Sample orientation in a magnetic field for parallel field calculations.

$$\frac{\hbar}{2m}\left[-i\nabla - \frac{2e\bar{A}}{\hbar c}\right]^2\bar{\Psi} = -\frac{\alpha}{\hbar}\bar{\Psi} = \varepsilon\bar{\Psi} \qquad (A.1)$$

Now we consider a slab of thickness d parallel to the xz plane. The film extends from +d/2 to -d/2 on the y-axis. We apply a magnetic field H parallel to the z-axis as shown in Fig.(A-1). We choose a gauge $A = yH\hat{x}$. For small fields the eigenvalues of Eq.(A.1) can be written as[109]

$$\varepsilon = \frac{\hbar}{2m}\left[q_x^2 + q_z^2 + \left(\frac{2n\pi}{d}\right)^2 + \left(\frac{2eH}{\hbar c}\right)^2\frac{d^2}{12}\right] \qquad (A.2)$$

where n is an integer that can take positive and negative values. Since the largest nucleation field corresponds to the smallest value of ε one takes

$$q_x = q_z = n = 0$$

In this low field regime, the order parameter has its maximum amplitude located at the center of the slab[109]. As the field increases to a value given by

$$H \approx 1.6\left(\frac{\hbar c}{2e}\right)\left(\frac{2}{d}\right)^2 \approx 12.5\, H_d \qquad (A.3)$$

(where $H_d = \hbar c/4ed^2$)vortices appear in the sample and surface nucleation of superconductivity begins. Thus for $H > 12.5\, H_d$ the eigenvalues are no longer given by Eq.(A.2) [see Fig.(4.6) and Fig.(4.9) in Ref.109]. Strictly speaking, for a field of $H = 12.5\, H_d$ the eigenvalue given by the

low-field expression, Eq.(A.2), is smaller than a numerical solution of the eigenvalue equation by ~10%.

A-2 Calculation of the Cooperon Amplitude

Now we consider the calculation of the Cooperon amplitude for a thin film in a parallel field. Fig.(A-1) also describes this situation. The relevant eigenvalue equation is

$$D\left[-i\nabla - \frac{2e}{\hbar c}\vec{A}\right]^2 \varphi = \varepsilon\varphi \qquad (A.4)$$

with the boundary condition

$$\left[-i\nabla - \frac{2e}{\hbar c}\vec{A}\right]_n \varphi = 0$$

Thus a substitution of $\hbar/2m$ by D in Eq.(A.1) yields Eq.(A.4) with the same boundary condition. Hence the eigenvalues for <u>small fields</u> are also given by

$$\varepsilon_{n,q_x,q_z} = D\left[q_x^2 + q_z^2 + \left(\frac{2n\pi}{d}\right)^2 + \left(\frac{2eH}{\hbar c}\right)^2 \frac{d^2}{12}\right] \qquad (A.5)$$

Now in order to evaluate change in the conductivity per unit area due to localization, we compute

$$\Delta\sigma_{2D}^{Loc} = -\frac{2e^2 D}{\pi\hbar}\frac{1}{(2\pi)^2}\sum\iint \frac{dq_x\, dq_z}{\varepsilon_{n,q_x,q_z} + \tau_i^{-1}}$$

We have to sum over the discrete quantum number n and integrate over the continuous quantum numbers q_x and q_z. Altshuler and Aronov[17] perform

this calculation. Their derivation does not clearly state all the steps in the calculation of the conductivity. We give here a complete account of the derivation.

We assume that the dominant contribution comes from the n=0 term (since $\frac{2\pi}{d} > l_i$, corresponding to a quasi-two-dimensional behavior). The two-dimensional integral over q_x and q_y can be performed in radial coordinates with the choice of the upper limit for the radial coordinate $q_{max} = 1/l$ where l is the elastic mean free path. We then calculate the conductivity per unit area (which is also the conductance per unit area) due to localization as

$$\Delta\sigma_{2D}^{Loc} = \frac{-e^2}{2\pi^2\hbar} \ln\left(\frac{q_{max}^2}{\gamma^2}\right) \qquad (A.6)$$

Here

$$\gamma^2 = \frac{1}{l_i^2} + \left(\frac{2eH}{\hbar c}\right)^2 \frac{d^2}{12}$$

and we have taken $q_{max}^2 + \gamma^2 = q_{max}^2$ in arriving at Eq.(A.6) since $\gamma \ll q_{max}$ in typical experimental situations. Thus we can write the fractional change of resistance due to localization for a film in a parallel field as

$$\frac{\Delta R}{R} = \frac{-\Delta\sigma_{2D}^{Loc}}{\sigma_{2D}} = \frac{e^2 R_\square}{2\pi^2\hbar}\left[\ln\left(\frac{H_\phi}{H}\right) - \ln\left(\frac{H_i}{H} + \frac{H}{48\, H_s}\right)\right] \qquad (A.7)$$

in terms of characteristic fields defined in Eq.(2.11a). We note that

this calculation has so far assumed the spin-orbit scattering to be negligible. The result quoted in Eq.(2.12) includes an extension for finite spin-orbit scattering[110] [see also Sec.(II-B.2)].

A-3 Comments on the Validity of the Low Field Approximation

Since Eq.(A.2) is valid under the condition given by Eq.(A.3), Eq.(A.5) is also applicable with the same restriction on the strength of the magnetic field. Therefore, we propose that Eq.(A.7) is valid only when

$$H < 12.5\ H_d$$

It will be interesting to see how much farther the analogy between the superconducting order parameter and the Cooperon amplitude can be pursued.

APPENDIX B

Extension of the 1D Theory to Include Spin-Orbit Scattering

In this appendix, we describe the extension of the theory of localization for quasi-one-dimensional systems to include spin-orbit scattering.

B- 1 Results of Altshuler and Aronov[17]

We consider a wire of width W and thickness d such that W,d << ℓ_i. The wire has its length along x-axis and width W along the z-axis in a field H = H $\hat{y}$ [see Fig.(V-1)]. The calculation of the eigenvalues of the Cooperon operator is similar to the one discussed in Appendix A for thin films in parallel field. The eigenvalues for small applied fields are given by

$$\varepsilon_{m,n,q_x} = D\left[q_x^2 + \left(\frac{2\pi m}{d}\right)^2 + \left(\frac{2\pi n}{W}\right)^2 + \left(\frac{2eH}{\hbar c}\right)^2 \frac{W^2}{12} \right]$$

Here m and n are integers. The quantization of the eigenvalues of the operator in the y- and z-directions is due to the finite film thickness and film width respectively. The small field is now qualified by the condition

$$H < 12.5\, H_W \qquad (B.1)$$

where $H_W = \hbar c/4eW^2$ since the penetration of the magnetic field is now restricted to a width W (instead of the thickness d, as was discussed in Appendix A). In this context we calculate the contribution to the conductivity per <u>unit length</u> due to localization as

$$\Delta\sigma_{1D}^{Loc} = -\frac{2e^2D}{\pi\hbar}\left(\frac{1}{2\pi}\right)\sum_{m,n}\int_{-q_{max}}^{q_{max}} \frac{dq_x}{\varepsilon_{m,n,q_x} + \tau_i^{-1}}$$

The summation is over the discrete quantum numbers m and n and the continuous values of q_x. Since $(2\pi/d) \gg \ell_i$ and $(2\pi/W) \gg \ell_i$ we can ignore all other terms of the discrete series except n = 0 and m =0. However, the integration over q_x has to be performed. We note that q_x can take both positive and negative values. The largest magnitude for q_x corresponds to the shortest length scale over which the Cooperon interference is possible. This length scale from our discussion in Sec.II-B.1 is the elastic mean free path ℓ . Therefore the q_x integral has to be from $-1/\ell$ to $+1/\ell$. Since most of the contribution to the integral comes from values of q_x close to zero and $\ell \ll \ell_i$, the limits for the q_x integral can be conveniently taken to be infinity. The integral can be performed very easily yielding the following expression for conductivity per unit length (which is also the <u>conductance</u> per unit length) in quasi-one dimensional systems:

$$\Delta\sigma_{1D}^{Loc} = \frac{-\ell_i}{\pi\hbar/e^2}\left[1 + \frac{1}{12}\left(\frac{2eH\ell_i W}{\hbar c}\right)^2\right]^{-1/2} \qquad (B.2)$$

The fractional change in resistance can be readily derived as follows: If ΔG is the change in conductance for a wire of length L due to localization , then

$$\frac{\Delta G}{G_0} = \frac{\Delta\sigma_{1D}^{Loc}}{L} \times \frac{1}{G_0}$$

where G_o (= $1/R_o$) is the total conductance of the wire. Then the fractional change of resistance due to localization is

$$\frac{\Delta R}{R} = \frac{-\Delta G}{G_o} = \frac{\rho_o}{Wd}\,\frac{l_i}{\pi\hbar/e^2}\left[1+\frac{1}{12}\left(\frac{2eHl_iW}{\hbar c}\right)^2\right]^{-1/2} \qquad (B.3)$$

In terms of sheet resistance $R_\square$ and characteristic fields H_i and H_W, Eq.(B.3) can be recast as

$$\frac{\Delta R}{R} = \frac{R_\square}{\pi\hbar/e^2}\left[\frac{H_W}{H_i}\right]^{1/2}\left[1+\frac{H^2}{48\,H_i\,H_W}\right]^{-1/2} \equiv f_1(H,H_i) \qquad (B.4)$$

B-2 Comparison to Thouless' zero field result

From Eq.(B.3) one obtains for H= 0

$$\frac{\Delta R}{R} = \frac{\rho_o}{Wd}\,\frac{l_i}{\pi\hbar/e^2} = \frac{l_i}{L_o}$$

where L_o corresponds to a wire of resistance $\pi\hbar/e^2 \sim 12.4$ kohms. This apparently is different from Thouless' formula[3] of

$$\frac{\Delta R}{R} = \frac{\rho_o}{Wd}\,\frac{l_i}{\sqrt{2}\,\pi\hbar/e^2}$$

by $\sqrt{2}$. This discrepancy can be traced back to Thouless' choice of Einstein's equation as

$$\sigma = \frac{1}{2}\,N(E_F)\,e^2\,D$$

instead of our definition

$$\sigma = \eta(E_F)\, e^2\, D$$

$\eta(E_F)$ is the density of states per unit volume at the Fermi energy and D is the diffusion constant. When thus accounted for, the two results agree exactly.

B-3 Inclusion of Spin-Orbit scattering

We observed in Sec.II-B.2 that the effect of spin-orbit scattering on the Cooperon was to split it into triplet and singlet parts

$$C_n = \frac{3}{2}\,\frac{1}{\varepsilon_n + \tau_2^{-1}} - \frac{1}{2}\,\frac{1}{\varepsilon_n + \tau_i^{-1}} \qquad (2.8)$$

The triplet part (the first term) has $l_2 = (D\tau_2)^{1/2}$ as the characteristic length and the singlet part (the second term) has l_i as the characteristic length

Case(i) Fully one-dimensional behavior:

If the sample width W is small compared to both l_i and l_2 we have a fully one-dimensional system. Due to the linear addition of the the singlet and triplet term, using equations (2.8) and (B.4) we can immediately write down the fractional resistance change as

$$\frac{\Delta R}{R} = \frac{3}{2}\, f_1(H, H_2) - \frac{1}{2}\, f_1(H, H_i) \qquad (2.13)$$

$f_1(H,H_i)$ is defined by Eq.(B.4).

Case(ii) Mixed dimensional systems

If $l_2 \ll W \ll l_i$ then an evaluation of conductivity will involve

a two-dimensional integral for the triplet term and one dimensional integral for the singlet term. We note that the singlet term adds linearly to the triplet term. Thus, knowing the results for a fully 2D system [Eq.(2.11)] and a fully 1D system [Eq.(2.13)] we can deduce for such a mixed dimensional system

$$\frac{\Delta R}{R} = \frac{3}{2} f_2(H, H_2) - \frac{1}{2} f_1(H, H_i) \tag{2.14}$$

where

$$f_2(H, H_2) \equiv \frac{R_\square}{2\pi^2 \hbar/e^2} \left[-\psi\left(\frac{1}{2} + \frac{H_2}{H}\right) + \ln\left(\frac{H_0}{H}\right) \right]$$

The form for $f_2(H, H_2)$ is correct[11] for $H_0 \gg H$, H_i, H_2. We note that both Eq.(2.13) and (2.14) have to be used with the same field restriction given by Eq.(B.1) because of the use of perturbation theory in the calculation of the 1D result.

APPENDIX C

Maki-Thompson Fluctuations for 1D Systems

Here we evaluate the Maki-Thompson fluctuations for a narrow wire with W,d << l_i in an external field H perpendicular to the plane of the film . The configuration is identical to the one shown in Fig.(V-1). The eigenvalues of the operator $D\hat{q}^2$ for this situation were given in Appendix B. They are

$$\varepsilon_{m,n,q_x} = D\left[q_x^2 + \left(\frac{2\pi m}{d}\right)^2 + \left(\frac{2\pi n}{W}\right)^2 + \left(\frac{2eH}{\hbar c}\right)^2 \frac{W^2}{12} \right] \tag{C.1}$$

n and m are integers that can take both positive and negative values. The contribution to conductivity per unit length due to MT fluctuations is

$$\Delta\sigma_{1D}^{MT}(T,H) = \frac{2De^2}{\pi\hbar} \times \frac{1}{2\pi} \beta(T/T_c) \sum_{m,n} \int_{-q_{max}}^{q_{max}} \frac{dq_x}{\varepsilon_{m,n,q_x} + \tau_i^{-1}} \tag{2.15}$$

Since W and d << l_i we can assume that all other contributions except n = m = 0 are negligible in the evaluation of (2.15). Under this approximation the conductivity per unit length due to MT fluctuations for wire becomes

$$\Delta\sigma_{1D}^{MT}(T,H) = \frac{e^2}{\pi^2\hbar} \beta(T/T_c) \int_{-q_{max}}^{q_{max}} \frac{dq_x}{\left[q_x^2 + \left(\frac{2eH}{\hbar c}\right)^2 \frac{W^2}{12} + l_i^{-2} \right]} \tag{C.2}$$

We have used $\ell_i = (D\tau_i)^{1/2}$ in Eq.(C.2). The main difference in the calculation of MT fluctuations from that of localization (see Appendix B) is in the choice of the upper cut-off value for the q_x integration. In the case of MT fluctuations (see Sec.II-D) we are describing the motion of two electrons of approximately zero total momentum that were created as a result of the decay of a pair fluctuation. The maximum length over which the coherence continues to exist is the inelastic scattering length (see Sec.II-D). ℓ_i^{-1} has already been included explicitly as the minimum value for q in Eq.(C.2). The minimum length over which the correlation exists between the electrons in a superconductor is given by the coherence length $\xi(T)$ that grows as $T \to T_c$. From the theory of dirty-limit superconductors we can write

$$\xi^2(T) = \frac{\pi \hbar D}{8 k_B T} \frac{1}{\ln(T/T_c)} \qquad (C.3)$$

Therefore q_{max} for the integral in Eq.(C.2) has to be chosen as

$$q_{max} = \xi^{-1}(T)$$

Similar to the case of 1D localization (discussed in Appendix B), the integral of Eq.(C.2) has to be done from $-q_{max}$ to $+q_{max}$. Since most of the contribution comes from $q \sim 0$ and if we assume $T \gg T_c$,

$$\xi(T) \ll \ell_i$$

q_{max} can be taken to be infinity without much error. Thus we get the final equation for conductivity per unit length as

$$\Delta\sigma_{1D}^{MT} = \beta(T/T_c)\,\frac{l_i}{\pi\hbar/e^2}\left[1+\frac{1}{12}\left(\frac{2eHWl_i}{\hbar c}\right)^2\right]^{-1/2} \quad (C.4)$$

We note that this is the same result as that for 1D localization [Eq.(B.1)] except for the appearance of the prefactor $\beta(T/T_c)$ and change of sign. Even though the actual cut-off values are different for the integrals for localization and MT fluctuations, in the evaluation of the integrals

$$\tan^{-1}(l_i/l) \sim \tan^{-1}[(l_i/\xi) \sim \tan^{-1}(\infty) = \pi/2$$

Hence the upper cut-off on q does not appear explicitly in the final result in either case.

The 2D calculations do not have this nicety. This is because they result in logarithmic functions $\ln(l_i/l)$ and $\ln(l_i/\xi)$ for the localization and MT fluctuation contributions respectively. These two functions can differ by a significant factor. In addition, the temperature dependence enters the theoretical result directly because of the choice of $1/\xi(T)$ as q_{max}. The evaluation of fractional change in resistance can be derived from Eq.(C.4) similar to the derivation of Eq.(B.3) from Eq.(B.2). One obtains,

$$\frac{\Delta R}{R}^{MT} = \frac{-R_D}{\pi\hbar/e^2}\,\beta(T/T_c)\left[\left(\frac{H_W}{H_i}\right)^{1/2}\left(1+\frac{H^2}{48\,H_i H_W}\right)^{-1/2}\right]$$

in terms of characteristic fields $H_i = \frac{\hbar c}{4eD\tau_i}$ and $H_W = \frac{\hbar c}{4eW^2}$

APPENDIX D

Classical Magnetoresistance in Al

In this appendix, we derive the classical magnetoresistance in Al. In a free electron Drude model, magnetoresistance is zero[12]. Hence, we consider the magnetoresistance based on a two band model. Each of the bands is assumed to be Drude like. The relevant theoretical expressions for a metal with an electron band and a hole band are derived in Ref.28. The equation for normalized magnetoresistance is given by

$$\frac{\delta R}{R} = \frac{\sigma_e \sigma_h (\beta_e - \beta_h)^2 H^2}{(\sigma_e + \sigma_h)^2 + H^2(\beta_e \sigma_e + \beta_h \sigma_h)} \qquad (D.1)$$

The subscript 'e' corresponds to the electron band in the third Brillouin zone of Al and 'h' to the hole band in the second Brillouin zone. The first zone is completely full. In Eq.(D.1)

$$\beta_e = \frac{e\tau_e}{m_e} \quad \text{and} \quad \sigma_e = \frac{n_e e^2 \tau_e}{m_e}$$

β_h and σ_h are defined similarly. We note that only if $\beta_h = \beta_e$, the magnetoresistance will be zero.

To estimate the size of the magnetoresistance, we use the band structure parameters for Al quoted by Ashcroft[111]. We take

$$\frac{m_e}{m_h} = 0.1 \quad ; \quad \frac{\tau_e}{\tau_h} = 0.6$$

The densities of electrons and holes have to be estimated from the fraction of the Brillouin zone occupied by them in the third and second zone respectively. Based on Ashcroft's suggestion (that densities of third zone states amount to only a few percent of an electron per atom) we

take n_e = 0.05 electron per atom. High field Hall effect experiments confirm the fact[12] the $n_h - n_e = 1$. Hence n_h = 1.05 electron per atom. The numerical substitutions yield

$$\frac{\beta_e}{\beta_h} = 6 \quad ; \quad \frac{\sigma_e}{\sigma_h} = 0.3$$

and a magnetoresistance

$$\frac{\delta R}{R} \approx \frac{7.5\,(\beta_h H)^2}{1.7 + 7.8\,(\beta_h H)^2} \qquad (D.2)$$

We note that $\hbar k_F = m_o v_F = m_h v_h$ and $\ell_h = v_F \tau_h$ yielding

$$\beta_h H = \left(\frac{e}{\hbar c}\right)\left(\frac{\ell_h}{k_F}\right) H \approx 0.1\, H \ell_h \qquad (D.3)$$

We evaluate ℓ_h based on the band structure parameters we have used so far. We note that free electron Drude conductivity can be written as the sum of the conductivities of the electron and the hole bands so that

$$\sigma_c = \sigma_e + \sigma_h$$

In the free electron model the density is taken to be 3 electrons per atom for Al. Also, the elastic scattering time τ entering the free electron Drude formula Eq.(2.2) is given by $\ell = v_F \tau$. After some algebraic manipulations we arrive at

$$\tau_h \approx 2.3\,\tau$$

Since we have assumed[111] $m_h = m_o$ and

$$\ell_h = 2.3\,\ell \qquad (D.4)$$

Combining Eqs.(D.4), (D.3) and (D.2) and noting that $(H\ell) \ll 1$ in our field regime we obtain,

$$\frac{\delta R}{R} \approx 0.23 (H\ell)^2 \qquad (D.5)$$

This prediction is qualitatively confirmed by our experiments (see Sec.IV-B). However Eq.(D.5) predicts a magnitude of ~ 4 <u>smaller</u> than our experimental result. Considering the approximations made to arrive at this result, the agreement is quite acceptable.

Notably, Eq.(D.2) predicts a saturation of magnetoresistance for $(H\ell) \gg 1$ resulting in

$$\frac{\delta R}{R} \approx 1$$

This behavior has been observed[88].

APPENDIX E

Process Parameters for Photolithography

E-1 Cleaning of coverglass substrates

Corning #1-1/2 coverglass slides (18mm x 18mm x 0.17mm) were used as substrates for most of this work. The cleaning procedure was:

(a) Ultrasonic agitation in an acetone bath for 3 min.

(b) Spray-bottle rinse in acetone.

(c) Ultrasonic agitation in isopropanol for 3 min.

(d) Spray-bottle rinse in isopropanol

(e) Blow dry with high purity nitrogen gas.

E-2 Preparation of the Photoresist (PR) Layer

Shipley[112] AZ-1350B photoresist was used for high resolution work. It was spun on at 6000 RPM for a 3000Å layer, and at 10000 RPM for a 2500Å layer. Shipley AZ-1350J photoresist was used for lower resolution work. A spin speed of 3000 RPM for AZ-1350J yields a 2 micron thick layer. The substrate was prepared for optical lithography as follows:

(a) The substrate was centered on the chuck of a high-speed spinner. The vacuum hold down was then turned on.

(b) A small amount of PR was taken in a clinical syringe and fitted with a Millipore[113] filtering unit. The filtering unit consisted of a prefilter (type AP 2502200) and an absolute polytetrafluoroethylene filter (type FALP 02500) of 1 micron pore size. A few drops of filtered PR were quickly dropped onto the spinning substate.

(d) The spinning time was typically 40 sec.

(e) The substrate was checked for uniformity. Typically the central

portion of the slide looked uniform over a circular area of ~ 1cm diameter and at the corners of the coverglass slide the PR layer was thicker.

(f) The substrate was then baked on a hot plate for 15 min. at 85°C.

E-3 Exposure of PR Pattern

(a) Contact exposures were made using an unfiltered 100-watt high pressure mercury-vapor arc lamp. Typical exposure time was 30 sec.

(b) Projection exposures were made using a Carl Zeiss Photomicroscope equipped with type II-C epi-illuminator incorporating a 15-Watt tungsten lamp. Centerable objectives of the 'Aufl Pol' series of achromats were used for exposures. A red filter with a low pass cut-off of 6200Å (Corning type CS2-60) was used during focussing and alignment. A blue filter with a single transmittance peak at 4000Å (Corning type CS5-58) was used during exposure. A voltage regulating (Sola) transformer was used in the AC power line of the microscope lamp.

E-4 Development of Exposed PR

We used Shipley AZ-developer, diluted 1:1 with distilled deionized water.

(a) The recommended temperature of the the developer solution was 21 $\pm$ 1 °C. We did not find much effect on the quality of the developed PR patterns even if the temperature was not very carefully controlled to even 21 $\pm$ 3°C for structures larger than 2 micron.

(b) The substrate was dipped into the developer continually mixed by a magnetic stirrer. Typical developing time for a 6000Å thick 1350B layer was 30 sec.

(c) The substrate was rinsed in running distilled deionized water for at least 1 minute.

(d) The sample was then blown dry in high purity nitrogen gas.

The entire processing described in this appendix was done in a clean room to avoid dust. The submicron wide wires were fabricated on oxidized silicon wafers and the details of the processing and x-ray lithography can be found in Ref.75.

APPENDIX F

Inferring Diffusion Constants from Superconducting Critical Fields

Here we discuss the theoretical expressions used to infer the diffusion constant D in thin films from the measurement of superconducting critical fields close to T_c. Since we are interested in applying magnetic fields parallel and perpendicular to the plane of the thin film we discuss these two cases below.

(i) Perpendicular fields:

When the magnetic field is oriented perpendicular to the film the critical field is given by[56]

$$H_{c2\perp} = \frac{\Phi_o}{2\pi \xi^2(T)} \qquad (F.1)$$

Φ_o (= hc/2e) is the flux quantum. Close to T_c the coherence length is approximated by

$$\xi(T) = \frac{\xi(0)}{(1 - T/T_c)^{1/2}}$$

where

$$\xi^2(0) = \frac{\pi \hbar D}{8 k_B T_c}$$

Substituting for $\xi(T)$ in Eq.(F.1) we obtain

$$dH_{c2\perp}/dT = \frac{4 k_B c}{\pi e D} \qquad (F.2)$$

The above derivation assumes that $D = (1/3)v_F \ell$ corresponding to three dimensional diffusion in the film.

(ii) Parallel fields:

For magnetic fields parallel to the plane of the film the critical field is given by[56]

$$H_{c2\parallel} = \sqrt{12}\ \frac{\bar{\Phi}_o}{2\pi d\, \xi(T)} \qquad (F.3)$$

where d is the thickness of the film. Using the definition of $\xi(T)$ Eq.(F.3) can be recast as

$$H_{c2\parallel} = \left(\frac{49}{2\pi^3}\right) \frac{\bar{\Phi}_o^2}{d^2} \frac{k_B}{\hbar D} (T_c - T) \qquad . \qquad (F.4)$$

We note that

$$\frac{H_{c2\parallel}}{H_{c2\perp}} = \sqrt{12}\ \frac{\xi(T)}{d}$$

and hence for large ratios of $\xi(T)/d$ the $H_{c2\parallel}$ can be much larger than $H_{c2\perp}$

APPENDIX G

The Evaluation of $\beta(T/T_c)$

The parameter $\beta(T/T_c)$ used in the theoretical expressions was <u>not a free parameter</u> in our fitting procedures. $\beta(T/T_c)$ was calculated from a polynomial fit to the theoretical values tabulated by Larkin[23]. We used the form generated by us of

$$\beta(T/T_c) = -1.066 + 2.024\ X + 0.028\ X^2 \qquad \text{for } X > 1.0$$

and

$$\beta(T/T_c) = -1.085 \times 10^{-3} - 2.779 \times 10^{-3}\ X + 1.733\ X^2 - 0.950\ X^3 + 0.270\ X^4 \qquad \text{for } X \leq 1.0$$

where

$$X = [\ln(T/T_c)]^{-1}$$

The theoretical values of Larkin and the fits done using the coefficients given above are shown in Fig.G-1. The theoretical numbers of Larkin are reproduced by these polynomials to within 1% .

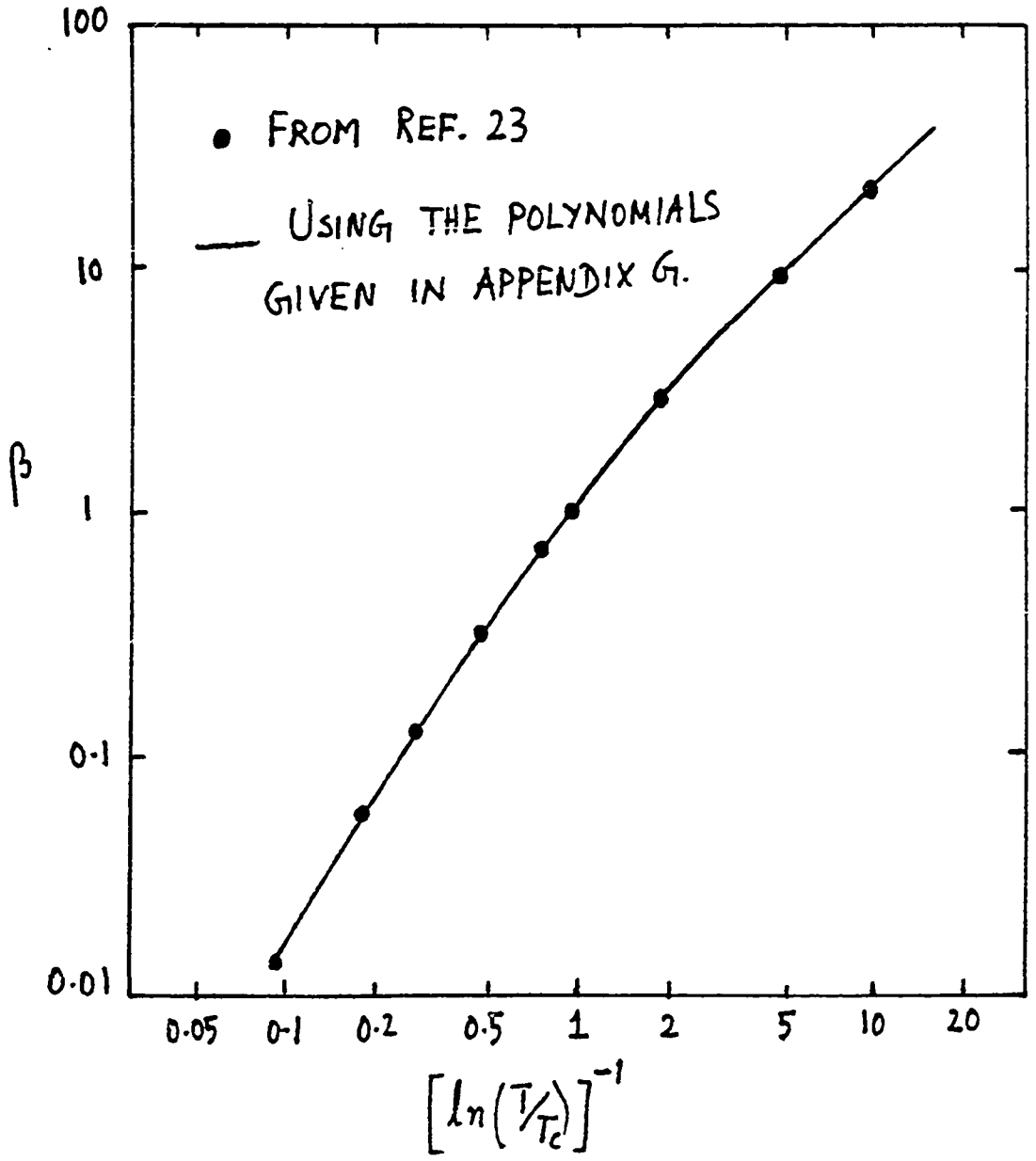

Fig.G-1 The electron-electron interaction parameter $\beta(T/T_c)$ as a function of $[\ln(T/T_c)]^{-1}$.

REFERENCES

1. P. W. Anderson, Phys. Rev. 109, 1492 (1958).

2. N. F. Mott, Metal Insulator Transitions (Taylor and Francis, London 1974).

3. D. J. Thouless, Phys. Rev. Lett. 39, 1167 (1977); Solid State Comm. 34, 683 (1980).

4. E. Abrahams, P. W. Anderson, D. C. Licciardello and T. V. Ramakrishnan, Phys. Rev. Lett. 42, 673 (1979).

5. S. Hikami, A. I. Larkin, and Y. Nagaoka, Prog. Theor. Phys. 63, 707 (1980); S. Maekawa and H. Fukuyama, J. Phys. Soc. Jpn. 50, 2516 (1981).

6. B. L. Alt'shuler, A. G. Aronov, A. I. Larkin and D. E. Khmel'nitski, Zh. Eksp. Teor. Fiz. 81, 768 (1981) [Sov.Phys.JETP 54, 411 (1981) : B. L. Alt'shuler, D. E. Khmel'nitskii, A. I. Larkin, and P. A. Lee, Phys.Rev. B22, 5142 (1980)]

7. H. Fukuyama, Chapter in Percolation, Localization and Superconductivity, A. M. Goldman and S. Wolf, Ed.(Plenum, New York, 1984), pg. 161

8. B. L. Alt'shuler, A. G. Aronov, P. A. Lee, Phys. Rev. Lett. 44,1288 (1980)

9. P. W. Anderson, J. Phys. Chem. Solids, 11, 26 (1959); J.Appel and A. W. Overhauser, Phys Rev.B 29, 99 (1984)

10. G. Bergmann, Phys. Rev.B 3, 3797 (1971)

11. G. Bergmann, Phys. Rep. 107, 1 (1984)

12. N. W. Ashcroft and N. D. Mermin, Solid State Physics (Holt, Rinehart and Winston, New York, 1976).

13. J. S. Langer and T. Neal, Phys. Rev. Lett. 16, 984 (1966)

14. O. Madelung, Introduction to Solid State Theory (Springer Verlag, New York,1978)

15. B. L. Alt'shuler, A. G. Aronov, D. E. Khmel'nitski and A. I. Larkin, in Quantum Theory of Solids, I. M. Lifshitz, Ed.(Mir Publishers, Moscow, 1982)

16. H. A. Bethe and E. E. Salpeter, Quantum mechanics of One and Two-Electron Atoms (Plenum-Rosetta, New York, 1977), pg. 185.

17. B. L. Alt'shuler and A. G. Aronov, Pis'ma Zh. Eksp. Teor. Fiz. 33, 515 (1981) [JETP Lett. 33, 499 (1981)]

18. P. Santhanam, S. Wind, and D. E. Prober in Proceedings of the Seventeenth International Conference on Low Temperature Physics, Karlsruhe, FRG, 15-22 August 1984, (North Holland, 1984), Part I, pg.495

19. L. G. Aslamazov and A. I. Larkin, Fizika Tverdogo Tela 10, 1104 (1968) [Soviet Physics-Solid State 10, 875 (1968)]

20. W. J. Skocpol and M. Tinkham, Rep. Prog. Phys. 38, 1049 (1975)

21. K. Maki, Prog. Theor. Phys. 39, 897 (1968); R. S. Thompson, Phys. Rev. B1, 327 (1970)

22. J. M. Gordon, C. J. Lobb, and M. Tinkham, Phys. Rev. B29, 5232 (1984)

23. A. I. Larkin, Pis'ma Zh. Eksp. Teor. Fiz. 31, 239 (1980) [JETP Lett. 31, 219 (1980)

24. J. M. B. Lopes dos Santos and E. Abrahams, Phys. Rev. B31, 172 (1985)

25. M. E. Gershenson, V. N. Gubankov, and Yu. E. Zhuravlev, Solid State Commun. 45, 87 (1983); see caption of Fig.1 for their data-fitting procedure; Sov.Phys. JETP, 58, 167 (1983)

26. N. Wiser, Contemp. Phys. 25, 211 (1984).

27. C. M. Hurd, Electrons in Metals (Wiley, New York, 1975) pg. 268.

28. J. M. Ziman, Principles of The Theory of Solids (Cambridge University Press, 1972).

29. P. A. Lee and T. V. Ramakrishnan, Phys. Rev. B26, 4009 (1982)

30. A. Schmid, Z.Physik. 259, 421 (1973).

31. W. E. Lawrence and A. B. Meador, Phys.Rev. B18, 1154 (1978); see Table II and Eq.(25)

32. T. Wagehaupt and R. E. Doezema, Phys. Rev. B18, 742 (1978)

33. V. A. Gasparov and M. H. Harutunian, Sol. State. Comm. 19, 189 (1976)

34. A. Schmid, Chapter in The Proceedings of the International Conference on Localization, Interaction and Transport Phenomena in Impure Metals, August 1984, Braunschweig, FRG,(To be published in Springer Series on Solid State Science, Springer Verlag, 1985)

35. H. Takayama, Z.Physik. 263, 329 (1973).

36. Yu. Kagan and A. P. Zhernov, Zh. Eksp. Teor. Fiz. 50, 1107 (1966) [Sov. Phys. JETP 23, 737 (1966)]

37. G. Bergmann, Z. Phys. B 48, 5 (1982)

38. J. M. Ziman, Electrons and Phonons (Clarendon Press, Oxford,1960) pg.213.; A. B. Pippard, Philos. Mag. 46, 1104 (1955).

39. S. Kaplan, J. Low. Temp. Phys. 37, 343 (1979).

40. W. E. Lawrence and J. W. Wilkins, Phys. Rev B 7, 2317 (1973)

41. A. Schmid, Z. Physik. 271, 251 (1974)

42. B. L. Altshuler and A. G. Aronov, Sol. State Comm,46, 429 (1983)

43. E. Abrahams, P. W. Anderson, P. A. Lee and T. V. Ramakrishnan, Phys. Rev. B24, 6783 (1981)

44. P. Santhanam and D. E. Prober, Phys. Rev. B29, 3733 (1984)

45. P. Santhanam, S. Wind, and D. E. Prober, Phys. Rev. Lett. 53, 1179 (1984)

46. D. E. Prober, S. Wind, and P. Santhanam , Chapter in The Proceedings of the International Conference on Localization, Interaction and Transport Phenomena in Impure Metals, August 1984, Braunschweig, FRG, (To be published in Springer Series on Solid State Science , Springer Verlag, 1985)

47. J. M. B. Lopes dos Santos, Phys. Rev. B28, 1189 (1983)

48. H. Fukuyama and E. Abrahams, Phys. Rev. B27, 5976 (1983).

49. B. L. Altshuler, A. G. Aronov, and D. E. Khmel'nitskii, J.Phys.C 15, 7367 (1982).

50. W. E. Eiler, J. Low. Temp. Phys. 56, 481 (1984)

51. H. Fukuyama, Chapter in The Proceedings of the International Conference on Localization, Interaction and Transport Phenomena in Impure Metals, August 1984, Braunschweig, FRG. (To be published in Springer Series on Solid State Science , Springer Verlag, 1985)

52. J. L. Black, B. L. Gyorffy, and J. Jackle, Philos. Mag. B40, 331 (1979).

53. N. Giordano, W. Gilson, and D. E. Prober, Phys. Rev. Lett., 34, 725 (1979); N. Giordano, Phys. Rev. B 22, 5635 (1980); J. T. Masden and N. Giordano, Physica (Utrecht) 107B, 3 (1981)

54. A. Abrikosov and L. P. Gor'kov, Zh. Eksp. Teor. Fiz. 42, 1088 (1962) [Sov. Phys. JETP 15, 752 (1962)]

55. R. Meservey and P. M. Tedrow, Phys. Lett. 58A, 131 (1976); Phys. Rev. Lett. 41, 805 (1978)

56. M. Tinkham, Introduction to Superconductivity (McGraw-Hill, New York, 1975)

57. C. J. Pednick and H. Smith, J. Phys.C (Solid State) 13, 6313 (1980)

58. A. Schmid and G. Schön, J. Low Temp. Phys. 20, 207 (1975)

59. J. Clark, Phys. Rev. Lett. 28, 1363 (1972); T. R. Lemberger and J. Clarke, Phys. Rev. B23, 1088 (1981)

60. C. C. Chi and J. Clarke, Phys. Rev B19, 4495 (1979)

61. W. J. Skocpol in Nonequilibrium Superconductivity, Phonons, and Kapitza Boundaries, K. E. Gray, Ed. (Plenum, New York, 1981)

62. J. M. Aponte and M. Tinkham, J. Low. Temp. Phys. 51, 189 (1983)

63. G. J. Dolan and L. D. Jackel, Phys. Rev. Lett. 39, 1628 (1977)

64. M. Stuivinga, J. E. Mooij and T. M. Klapwijk, Physica 108B, 1023 (1981)

65. R. D. Mathis Company, Long Beach, Calif. 90806.

66. Alfa Products, Danvers, Mass. 01923

66a. MKS Instruments, Inc., Burlington, Mass. 01803.

67. D. Face, Ph.D. Thesis, Yale University (in preparation)

68. M. D. Feuer, Ph.D. Thesis, Yale University, 1980 (available from University Microfilms, Ann Arbor, MI 48106.)

69. M. D. Feuer and D. E. Prober, IEEE Trans. on Elec.Dev. 28, 1375 (1981)

70. D. E. Prober, Chapter in Percolation, Localization and Superconductivity, A. M. Goldman and S. Wolf, Ed. (Plenum, New York, 1984), pg.231

71. R. Wisnieff (Private communication)

72. D. E. Prober, M. D. Feuer and N. Giordano, Appl. Phys. Lett. 37, 94 (1980)

73. KTI Chemicals Inc., Sunnyvale, Calif. 94086

74. du Pont Company, Wilmington, Del. 19898

75. S. Wind (Private communication and unpublished)

76. D. C. Flanders and H. I. Smith, J. Vac. Sci. Technol. 15, 995 (1978); D. C. Flanders, Ph.D. Thesis, Massachusetts Institute of Technology, 1978, (unpublished)

77a. Model 147, Keithley Instruments, Inc., Cleveland, Ohio. 44139

77b. Princeton Applied Research Corporation, Princeton, N.J. 08540

78. Linear Research Inc., San Diego, Calif. 92110

79. B. J. Dalrymple, Ph.D.Thesis, Yale University,1983 (available from University Microfilms, Ann Arbor, MI 48106); B. J. Dalrymple and D. E. Prober, Rev. Sci. Instrum. 55, 958 (1984)

80. Cryocal, Inc., St. Paul, MN 55114.

81. E. Fawcett in Fermi Surface, W. Harrison and M. B. Webb, Ed. (Wiley, New York, 1960); When the free electron Fermi velocity is divided by thermal mass enhancement of 1.4 one gets v_F= 1.4 x10^8 cm/sec.

82. J. M. Gordon, C. J. Lobb, and M. Tinkham, Phys. Rev. B28, 4046 (1983)

83. G. A. Thomas and R. D. Parks, Phys. Rev. Lett., 27, 1276 (1971)

84. J. J. Hauser J. Low. Temp. Phys. 7, 335 (1972)

85. R. W. Cohen and B. Abeles, Phys. Rev. 168, 444 (1968)

86. J. M. Gordon, Ph.D. Thesis, Harvard University, 1984 (unpublished)

87. J. Bass, Adv. Phys. 21, 431 (1972)

88. F. R. Fickett, Cryogenics 11, 349 (1971)

89. Y. Bruynseraede, M. Gijs, C. van Haesendonck, and G. Deutscher, Phys. Rev. Lett. 50, 277 (1983); these authors have recently reanalyzed their original data according to the approach in this thesis. Their values of inelastic scattering time now agree with ours.

90. W. L. McLean and T. Tsuzuki, Phys. Rev. B29, 503 (1984)

91. J. E. Crow, M. Strongin, and A. K. Bhatnagar, Phys Rev. B9, 135 (1974).

92. W. E. Lawrence and J. W. Wilkins, Phys. Rev. B6, 4466 (1972)

93. P. C. van Son, J. Romijn, T. M. Klapwijk, and J. E. Mooij, Phys. Rev. B29, 1503 (1984)

94. O. Entin-Wohlman and R. Orbach, Phy. Rev. B24, 1177 (1981)

95. K. K. Choi, Phys. Rev. B28, 5774 (1983); R. A. Davies and M. Pepper, J. Phys. C: Solid State. 16, L353 (1983)

96. G. E. Zwaknagl and J. W. Wilkins, Phys. Rev. Lett. 53, 1276 (1984)

97. G. Bergmann, Phys. Rev. B29, 6114 (1984).

98. W. McGinnes, Ph.D. Thesis, University of California at Los Angeles, 1983 (unpublished)

99. A. E. White, M. Tinkham, W. J. Skocpol, and D. C. Flanders, Phys. Rev. Lett. 48, 1752 (1982)

100. N. Giordano, in Proceedings of the International Conference on Physics in One Dimension, J. Bernasconi and T. Schneider,Ed. (Springer Verlag, 1980)

101. P. Chaudhari and H. -U. Habermeier, Phys. Rev. Lett. 44, 40 (1980); Solid State Comm. 34, 687 (1980); P. Chaudhari, A. N. Broers, C. C. Chi, R. Laibowitz, E. Spiller, and J. Viggiano, Phys. Rev. Lett. 45, 930 (1980).

102. H. Raffy, R. Laibowitz, P. Chaudhari, and S. Maekawa, Phys. Rev. B28, 6607 (1983).

103. D. Abraham and R. Rosenbaum, Phys. Rev. B27, 1409 (1983); Phys. Rev. B27, 1413 (1983)

104. A. C. Sacharoff, R. M. Westervelt, and J. Bevk, Phys. Rev. B29, 1647 (1984).

105. D. R. Overcash, B. A. Ratnam, M. J. Skove, and E. P. Stillwell, Phys. Rev. Lett. 44, 1348 (1980).

106. R. G. Wheeler, K. K. Choi, A. Goel, R. Wisnieff, and D. E. Prober, Phys.Rev. Lett. 49, 1674 (1982).

107. K. C. Mui, P. Lindenfeld, and W. L. McLean, Phys. Rev. B30, 2951 (1984).

108. H. Ebisawa, S. Maekawa and H. Fukuyama, Sol. State. Comm. 45, 75 (1983)

109. D. Saint-James, G. Sarma and E. J.Thomas, Type II Superconductivity, (Pergamon, New York,1969)

110. M. E. Gershenson , B. N. Gubenkov and Yu. E. Zhuavlev, Sov. Phys. JETP 56, 1362 (1982)

111. N. W. Ashcroft, Phys. Kondens. Mat. 9, 45 (1969)

112. Shipley Corporation, Inc., Newton, Mass. 02162

113. Millipore Corporation, Bedford, Mass. 01730